1994

Microstructure-strength relationships of a deformation processed titanium-yttrium composite

Alan Mark Russell
Iowa State University

Order Number 9503590

Microstructure-strength relationships of a deformation-processed titanium-yttrium composite

Russell, Alan Mark, Ph.D.

Iowa State University, 1994

U·M·I
300 N. Zeeb Rd.
Ann Arbor, MI 48106

Microstructure-strength relationships of a deformation processed titanium-yttrium composite

by

Alan Mark Russell

A Dissertation Submitted to the
Graduate Faculty in Partial Fulfillment of the
Requirements for the Degree of
DOCTOR OF PHILOSOPHY

Department: Materials Science and Engineering
Major: Metallurgy

Approved:

Signature was redacted for privacy.

In Charge of Major Work

Signature was redacted for privacy.

For the Major Department

Signature was redacted for privacy.

For the Graduate College

Iowa State University
Ames, Iowa

1994

TABLE OF CONTENTS

INTRODUCTION TO DEFORMATION PROCESSED COMPOSITES

"That same day Pharoah gave this order to the slave drivers and foremen in charge of the people: 'You are no longer to supply the people with straw for making bricks; let them go and gather their own straw ' "[1]. As illustrated by Moses' experience with bricks strengthened by straw, simple composite materials have played a role in the human experience for millenia. In the Modern Era, a host of more sophisticated composite materials has been developed to provide special combinations of materials properties that would be difficult to achieve with one material alone. Among the most recent of these are composites comprised of mixtures of immiscible, ductile metals that are mechanically worked to severe deformations to reduce the phase sizes of the dissimilar metals. These composites, frequently called "in-situ composites" since they are formed within the starting materials by deformation processing, provide combinations of mechanical, electrical, and other physical properties superior to those of conventional alloys. Numerous in-situ composites have been studied, including pearlitic steel [2], Ag-Cu[3], Ag-Ni[4], and Ag-Fe. [5] However, the in situ composites receiving the most research attention during the past two decades are the Cu-X composites, where X = a body-centered cubic (bcc) metal immiscible in Cu such as Cr, Fe, Mo, Nb, Ta, V, or W [6-8].

The Cu-X in situ composites, comprised of face-centered cubic (fcc) Cu with 5% to 20% by volume element X, are severely deformed to produce a nanometer-scale microstructure of X filaments in the Cu matrix. The Cu-20% by volume Nb system (Cu-20Nb) has received particularly thorough study. Cu-20Nb has ultimate tensile strengths exceeding 2000 MPa after deformation to a true strain of $\eta = 12$ (where $\eta = \ln$ [initial cross section area / final cross section area]) [9].

The Cu-X alloys are remarkably ductile, which allows cast or powder processed starting billets to be deformed to $\eta = 13.4$ before breaking [10]. Such deformations represent

more than an 800-fold reduction in diameter and produce a concomitant reduction in the thickness and spacing of the X phase. Thus, an as-cast billet of Cu-20Nb, displaying Nb dendrites of average thickness 5 μm and average spacing 25 μm, can be deformation processed at room temperature into a wire with Nb filaments averaging 7 nm thick and 12 nm apart [11]. Such in-situ processed composite alloys have strengths substantially higher than those of any other Cu alloy, and deformation processing offers a relatively inexpensive method to produce bulk quantities of nano-scale composites. Debate continues on the mechanism(s) which account for the very high strengths of the Cu-X alloys [12-16], but discussion centers around the role of the nanofilamentary X structure in impeding propagation and motion of dislocations in both the Cu and X phases. The crystallographic alignment of the fcc Cu matrix with the bcc element X filaments is thought to play an important role in shaping the nanofilaments during deformation as well as in strengthening the resulting composite.

In the well-studied Cu-X composites, the matrix is fcc, and the second phase is bcc. Even in the other systems investigated (e.g. Ag-Cu, Ag-Fe, pearlite, etc.), the matrix is cubic. Insight into the role of crystallographic orientation in strengthening the Cu-X composites is somewhat limited because no non-cubic in situ composites exist to permit comparisons . If a binary mixture of non-cubic, immiscible metals could be found that displays filament formation upon deformation similar to that of the Cu-X in situ composites, it could provide valuable new information on the role crystallographic orientation plays in the phase morphology and strength of in-situ composites.

In an attempt to produce such a non-cubic in-situ composite alloy, two candidate metals were sought possessing good ductility, a binary phase diagram with mutual immiscibility and without intermetallic compounds, and roughly similar mechanical properties and melting temperatures. One combination of metals meeting these criteria is a Ti-Y alloy. Both of these metals are hexagonal close packed (hcp), and their elastic

constants, c/a ratios, and densities are nearly identical. It was hoped that investigation of the deformation processing behavior of such an hcp-hcp alloy might provide a second, non-cubic perspective into the fundamental mechanism(s) operating in in-situ composite alloys. In addition, if deformation processing proved to be a successful strengthening method in this system, a potentially useful low density, high strength alloy might result.

DEFORMATION PROCESSED COMPOSITES

Conductivity and Strength of Deformation Processed Composites

Deformation processed copper-refractory metal alloys have been under study for nearly twenty years. Their two most characteristic properties are excellent electrical conductivity and high strength. Both properties are attributable to their microstructure: a continuous copper matrix typically comprising about 80 volume per cent to 95 volume per cent of the composite, reinforced with body-centered cubic transition metal filaments only a few dozen to a few hundred atoms wide with aspect ratios between about 10^4 and 10^7 [3] (the ratio of filament length to filament thickness). These composites, hereinafter referred to as Cu-X (where X = Cr, Fe, Mo, Nb, Ta, V,or W), are usually prepared by casting or powder methods and deformation processed by various combinations of rolling, extrusion, swaging, and drawing. They possess electrical conductivities in the approximate range of 50% to 80% of the International Annealed Copper Standard [10], that is to say, the per cent of the conductivity of pure Cu. This is superior to the conductivity of other high strength copper alloys (e.g. Cu-2%Be, 32% IACS) that achieve their strength by precipitation hardening a second phase from solid solution. The reasons for the superior conductivity of Cu-X composites are readily apparent. The copper matrix , which comprises most of the composite volume, is nearly free of conductivity degrading solid solution atoms or precipitates (Most of the X elements in Cu-X have low solubility in copper at elevated temperatures and near zero solubility at room temperature.) In addition the second phase is aligned parallel to the rod or wire axis of the Cu-X specimen, leaving long, unobstructed pathways for electron flow parallel to the specimen's center line.

The mechanisms whereby the Cu-X structure contributes to the mechanical strength of the Cu-X composites is less well understood and has been the subject of extensive analysis and debate [12-16]. The relation between ultimate tensile strength and the amount of deformation processing received by the specimen is shown in Figure 1.

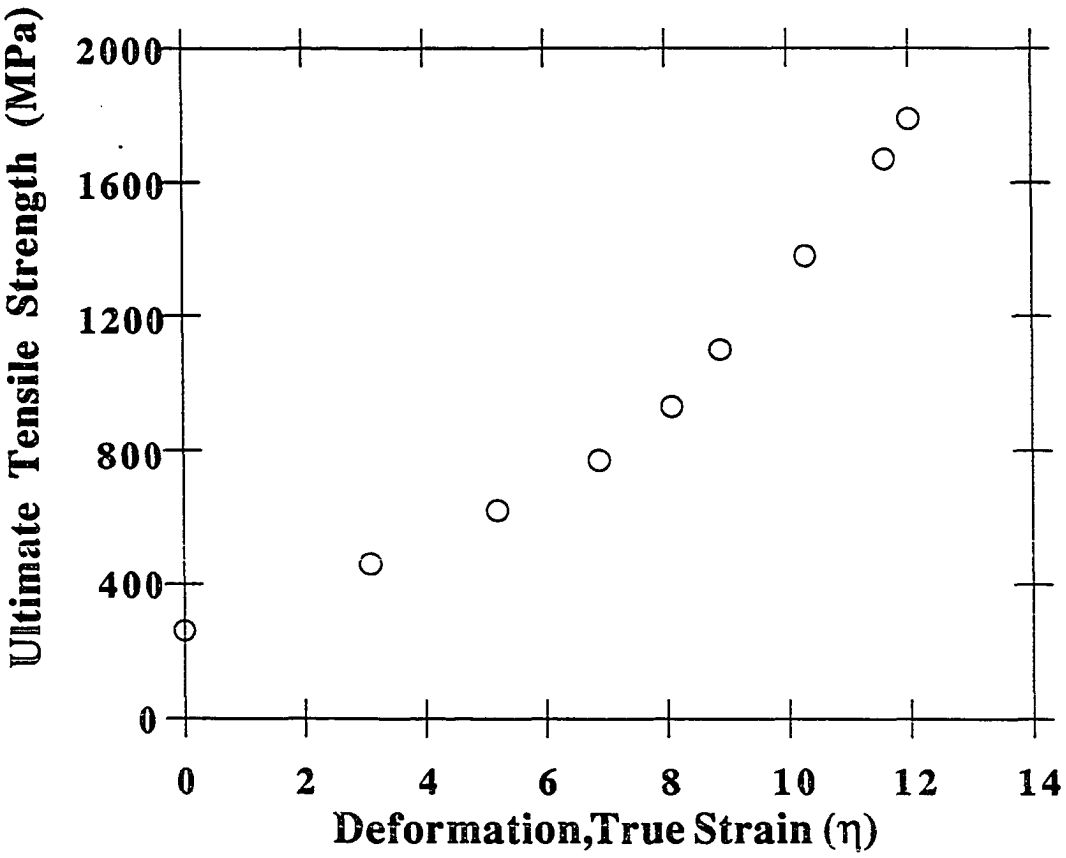

Figure 1. Ultimate tensile strength versus deformation true strain by wire drawing for a Cu-20 volume % Nb deformation processed composite rod [9]

One fact has been incontrovertibly demonstrated; the strengths of wire drawn Cu-X composites are substantially higher than one would predict from a simple rule-of-mixtures calculation [6,17]:

$$\sigma_{c,uts} = \sigma_{f,uts} V_f + \sigma_{m,uts} V_m$$

where $\sigma_{c,uts}$ is the ultimate tensile strength of the deformation processed composite, $\sigma_{f,uts}$ and $\sigma_{m,uts}$ are the ultimate tensile strengths of the fiber and matrix materials respectively, each deformed to the same true strain as the composite, and V_f and V_m are the volume fractions of the filament and matrix components of the composite. The rule of mixtures assumes that each phase acts independently of the other as a simple "load-sharing column" and ignores the effect of the phase boundaries on dislocation formation and motion. The rule of mixtures predicts strengths poorly for Cu-X composites. The rule of mixtures model predicts an ultimate tensile strength no higher than 550 MPa for the 18.2 volume % Nb in Cu composites studied by Bevk, Harbison, and Bell [6], yet the actual ultimate tensile strengths observed for these specimens ranged from 650 MPa (deformation processed to $\eta = 5.5$ (where η = true strain = ln [initial cross sectional area / final cross sectional area])) to 2200 MPa (deformation processed to $\eta = 11.5$). Rolled Cu-X composites also show higher strengths than predicted by the rule of mixtures [17], but their deviations from the rule are less pronounced. Since the Cu matrix and the X filaments in Cu-X are not single crystals, the grain boundaries within each phase presumably increase the strength of each phase by serving as barriers to dislocation motion. Including this effect in calculations of a rule of mixtures strengthening effect in a Cu-20 volume % Nb composite [17] increased the rule of mixtures strength prediction by only 100 MPa, far less than the observed difference.

Since many composite materials with large filament sizes possess strengths lower than the rule of mixtures prediction [6], Cu-X composite strengths greatly in excess of the rule of mixtures prediction suggest that some interaction between the matrix and filaments occurs to enhance the composite's strength. Several models have been proposed to

characterize this deviation from the rule of mixtures. Among the simpler models is the Hall-Petch relation:

$$\sigma_y = \sigma_0 + Kd^{-0.5}$$

where σ_y is the yield strength of a material with average grain diameter d and σ_0 and K are constants empirically developed for a given material [18].

Although originally developed to characterize the strengthening that accompanies grain size refinement in single phase material, the Hall-Petch expression could be applied to two phase composites by reasoning that phase boundaries in a composite material are comparable to grain boundaries in a homogeneous material in blocking dislocation motion. Several years before the first Cu-X composites were produced. Embury and Fisher applied the Hall-Petch relation to their data on the strength of drawn pearlitic steel [2] . Their steel specimens showed ultimate tensile strengths of 4800 MPa after deformation processing to η = 7.2. Embury and Fisher reasoned that the spacing of barriers to dislocations within and between phases will be reduced in direct proportion to the reduction in the overall diameter of the specimen wire as it is drawn:

$$1/r_e = (1/r_0)(D_0/D_e)$$

where the barrier spacing before strain is r_0, the barrier spacing after strain is r_e, the specimen diameter before strain is D_0, and the specimen diameter after strain is D_e. Since the true strain (ε) from drawing is:

$$\varepsilon = \ln(D_0/D_e)^2$$

then the barrier spacing as a function of strain will be:

$$1/r_e = 1/r_0 \{\exp(\varepsilon/2)\}$$

And this expression can be combined with the Hall-Petch relation to produce:

$$\sigma_y = \sigma_0 + K(cr_e)^{-0.5}$$

where r_e is equivalent to the grain diameter in the original Hall-Petch relation and c is a geometrical factor of the lattice relating the mean slip distance to the barrier spacing. In

pearlite, the ferrite slip planes are at angles of 20° to 70° to the lamellae, so a value of 2 was assumed for c. (A slip plane tilted at these angles to a shortest connecting line between barriers will be roughly twice as long as that shortest connector.) With algebraic simplifications, a final expression can be developed:

$$\sigma_y = \sigma_o + K(2)^{-0.5}(r_o)^{-0.5}(\exp \varepsilon/4)$$

which is in excellent agreement with the data of Embury and Fisher for pearlitic steel. It must be borne in mind that the assumptions made in this model may not be valid in all composite systems. The dislocation barriers include cell walls within grains; this analysis assumes these cell walls to have stable populations as η increases, implying no net change in total barrier numbers caused by the formation of new cells during deformation and removal of existing cell walls by recovery.

Morris and Morris [19] followed a somewhat similar approach in building a model by expanding the original treatment of Orowan [20] who considered dislocation bowing between unshearable particles to lead to material strength τ_{Orowan}:

$$\tau_{Orowan} = \tau_m + \mu b / \lambda$$

where τ_m is the matrix flow stress given by the Peierls stress, solute strengthening and other factors, μ is the shear modulus, b is the magnitude of the Burger's vector, and λ is the center-to-center spacing between the unshearable particles. This expression can be made more accurate by accounting for the varying line tension of screw versus edge dislocations and the non-zero diameter of the particles randomly dispersed on the slip plane:

$$\tau_{Orowan} = \tau_m + \frac{1}{1.18}\left[\frac{2\mu b}{4\pi(\lambda - \phi)}\right]\ln(\phi / 2b)$$

where ϕ is the particle diameter and the dislocation core radius is assumed to be 2b.

Substituting appropriate parameters for Cu in this equation and assuming that both screw and edge dislocations will be involved yields:

$$\sigma = \sigma_m + \left[\frac{5.8}{\lambda - \phi}\right] \ln(\phi / 2b)$$

Morris and Morris then assumed that the Hall-Petch grain boundary strengthening term was independent of the unshearable particle term and added the two directly to obtain:

$$\sigma = \sigma_m + \left[\frac{5.8}{\lambda - \phi}\right] \ln(\phi / 2b) + kD^{-0.5}$$

where D is the average grain diameter and k is a constant measuring the ease with which a dislocation can slip across a high angle grain boundary (typically 0.16 MPa $m^{0.5}$ for most copper alloys).

The strengthening of Cu-X deformation processed composites was initially thought to follow the Hall-Petch relationship. In a study that compared Cu-20Nb and Cu-20Ta composites [9], Spitzig and Krotz found that both composites had a Hall-Petch slope of -0.47 on a log-log plot of ultimate tensile strength versus average phase spacing. Ideally, this slope would be -0.5, the exponent of d (r_e in the Embury and Fisher analysis) in the Hall-Petch relation. The slope of -0.47 was seen for all four specimens studied: Cu-20Nb with initial dendrite spacings of 3.8 and 6.2 μm and Cu-20Ta with initial dendrite spacings of 3.5 and 7.1 μm. For specimens with larger initial dendrite spacings, more deformation is needed to achieve a given phase spacing, and this additional mechanical working of those specimens made them slightly stronger at the same average phase spacing. The effect of this additional mechanical work manifests itself as a larger K coefficient in the Hall-Petch equation. An effect was also seen from the higher elastic modulus of Ta (186 GPa) as compared with Nb

(103 GPa); the Cu-20Ta displayed a larger coeffcient K in the Hall-Petch relation, reflecting the superior ability of the stiffer Ta filaments to block dislocation motion. These findings would predict that the highest ultimate tensile strength for a given average phase spacing should result from a Cu-20Ta composite cast with a relatively large dendrite spacing. However, practical realities prevented direct demonstration of that prediction; the Cu-20Ta composites began to break apart during wire drawing at an η value of 8.9, whereas the Cu-20Nb composites withstood drawing to $\eta = 11.9$.

More significantly, the use of scanning electron microscopy (SEM) to measure interphase spacings in these composites was later found [21] to introduce an appreciable error in the average interphase spacings measured on Cu-20Nb composites deformation processed to η values higher than 3 to 4. More accurate data acquired using transmission electron microscopy (TEM) showed a dependence between ultimate tensile strength and phase size of $t_{Cu}^{-0.5}$ for low strains , but this dependence shifted to $t_{Cu}^{-0.38}$ at higher strains, a value inconsistent with the original Hall-Petch relation. This transition was thought to correlate with the transition from roughly cylindrical Nb dendrite arms in the original cast material to the kinked ribbon-like shape of the Nb filaments seen at η values greater than 4 where the Cu and Nb have both become highly textured and the Nb is forced to deform on only two <111> directions (see discussion on texturing in Cu-X composites in the following section).

Verhoeven, Chumbley, Laabs, and Spitzig proposed a modification of the rule of mixtures similar to a model proposed by Sevillano [22] for strengthening in pearlite that takes into account the dislocation propagation in both the Cu and Nb phases in a 80 vol. % Cu and 20 vol. % Nb composite:

$$\sigma_c = 0.8\left[\sigma_o + \frac{MAGb}{2\pi t}\ln\frac{t}{b}\right]_{Cu} + 0.2\left[\sigma_o + \frac{MAGb}{2\pi t}\ln\frac{t}{b}\right]_{Nb}$$

where σ_O(Cu) and σ_O(Nb) = ultimate tensile stress of similarly deformation processed Cu and Nb respectively, M is the Taylor factor (M = 3 in fcc metals, M = 2 in bcc metals), A = 1.21 (weighted average of edge and screw dislocations), G is the shear modulus, b is the Burger's vector magnitude, and t is the thickness between barriers. This expression provided a good match to their wire-drawn Cu-20Nb data obtained with TEM measurements of phase spacings.

More recently still, Biselli and Morris [23] employed ball mill attrition to produce a Cu-10Fe composite with an unusually fine starting particle size; the Fe particles were 500 to 700 nm before the start of deformation processing. After deformation to a true strain of 7.5, these specimens had an average Fe filament thickness of only 4 nm (only about 16 Fe atoms thick). Even though such phase thicknesses are even smaller than have been obtained for Cu-Nb composites, the data of Biselli and Morris do not show the characteristic exponential dependence of ultimate tensile strength upon deformation processing true strain. Their data appear essentially linear on a plot of σ versus η. Although their specimens are not directly comparable to Cu-20Nb specimens (Fe has appreciable solid solubility in Cu and formed precipitate particles of average size 3nm in their Cu matrix), Biselli and Morris proposed a modification of the equation proposed by Verhoeven, Chumbley, Laabs, and Spitzig to describe the yield stress (as opposed to ultimate tensile stress) as:

$$\sigma_{comp} = \frac{f_{Cu}\left[\sigma_0(Cu) + \sigma_{ribbons} + \sigma_{part.}\right] + f_{Fe}0.2\%E_{Fe}}{1 - \frac{f_{Fe}E_{Fe}}{E_{comp.}}}$$

where $\sigma_{comp.}$= the yield stress of the composite, $\sigma_0(Cu)$= the yield stress of Cu, $\sigma_0(Fe)$= the yield stress of Fe, $f_{Fe}$and f_{Cu} are the volume fractions, $\sigma_{ribbons}$ is the yield stress of the Fe ribbons (which are assumed to have a higher yield stress than that of the composite as a

whole), $\sigma_{part.}$ is the yield stress of the precipitate particles in the Cu matrix, and E_{Cu} and E_{Fe} are elastic moduli. With this adaptation of the model, Biselli and Morris have achieved a better fit to their data for Cu-10Fe by accounting for the fact that the Fe ribbons are presumably below their elastic limit at all values of η investigated and by also accounting for the presence in the Cu matrix of the precipitate particles. These circumstances do not pertain to the case of Nb in Cu, so the model of Biselli and Morris is more nearly a corollary than a competitor to the model of Verhoeven, Chumbley, Laabs, and Spitzig.

Funkenbusch, Lee, and Courtney [24] have analyzed the strengthening of deformation processed composites from a different perspective. They postulate that the deformation processed composites' behavior is attributable to a lack of saturation in their work hardening rates and that work hardening rates are seen to increase with increasing strain up to true strains of at least $\eta = 10$. This is quite different from the behavior of single-phase metals and metals strengthened by non-deforming dispersoids, where work hardening saturation is observed at much lower η values. When two ductile phases are deforming simultaneously, an unavoidable strain incompatibility occurs due to the differing crystal structures, lattice parameters, and slip systems of the two phases. This strain incompatibility is accomodated by generation of so-called "geometrically necessary" dislocations that allow the dissimilar deformations in the two phases to occur without generating large numbers of void spaces at phase interfaces.

A key concept in the analysis of Funkenbusch, Lee, and Courtney is that "while a fine interphase spacing is indirectly associated with increased strength, it is not, in this view, the cause of it." [24] Their model is based upon a modified rule of mixtures approach

$$\sigma_c = V_A\sigma_A + V_B\sigma_B$$

where σ is a flow stress term and V is the volume fraction of the phase. However, σ_A and σ_B are not the strengths of the single-phase metals subjected to the same true strain levels as

the composite. Instead they are assumed to be larger due to the increased number of dislocations present in each phase from the geometrically necessary dislocations arising from the strain incompatibility of the two phases. Both σ_A and σ_B can be expressed as:

$$\sigma = \sigma_0 + \alpha M G b \sqrt{\rho}$$

where σ_0 is the flow stress of that phase with a very low dislocation density, α is a constant with a value near one, M is an orientation Taylor factor, G is the shear modulus, b is the magnitude of the Burger's vector, and ρ is the dislocation density actually present in the phase in the composite environment.

Funkenbusch, Lee, and Courtney assume the actual dislocation density varies with strain as (the expression for phase A is shown below; a similar expression for phase B obtains with the A subscript replaced by B):

$$\frac{d\rho_A}{d\varepsilon} = \left[C_{1A}\sqrt{\rho_A} - C_{2A}\rho_A + \frac{P_A K}{V_A D} \right]$$

where C_{1A} is a dislocation multiplication constant, C_{2A} is a dislocation annihilation constant, P is a dislocation partition constant ($P_A + P_B = 1$), K is a compatibility constant accounting for the degree of strain incompatibility between the A and B phases (K would be zero in a single phase polycrystal.), and the interphase spacing D is a function of deformation strain ε as: $D = D_0 \exp[-\varepsilon / 2]$

The $\frac{P_A K}{V_A D}$ term in this expression would be zero in the absence of phase boundaries (i.e. in a single-phase metal) and work hardening saturation would occur at moderate strain levels (η) as the dislocation multiplication and annihilation terms reach a steady state balance. Funkenbusch, Lee, and Courtney demonstrated the application of this model to three deformation processed composite systems: Ag-Fe, Cu-Nb, and Cu-Nb. There are eight constants in their model (σ_0, C_1, and C_2 for each phase as well as K and P_A)which are

different for each binary composite system. The σ_o, C_1, and C_2 terms can be determined from the flow stress versus deformation strain relationship for single phase materials A and B. Single-phase flow strengths are assumed to vary with dislocation density as $\sigma = \sigma_0 + \alpha M G b \sqrt{\rho}$ and the dislocation density as a function of strain, as described above, can be found from the expression for the rate of change of dislocation density with strain when K is zero. K and P_A can be determined from one strength value for a given two-phase alloy composite (although several values are available, and use of more than one value improves the accuracy of the resulting values of K and P_A). The agreement of this model was deemed satisfactory for the Ag-Fe and Cu-Nb cases. In the Cu-Fe case, the model prediction fit poorly to the data, and this failure was attributed to the presence of dispersion hardening precipitates in the Cu matrix caused by the appreciable solid solubility of Fe in Cu.

The Funkenbusch, Lee, and Courtney model is predicated on the assumption that high η composites will have high dislocation densities, at least up to the model's validity limit of $\eta = 10$. Some of the earlier studies on deformation processed composites seemed to confirm the presence of very high dislocation densities. Bevk and co-workers [6] reported dislocation densities as high as 10^{13} cm^{-2} in their deformation processed Cu-Nb, although they also commented that some of their thinnest filaments (10 to 20nm thick) displayed significant areas devoid of dislocations. Frommeyer and Wassermann [3] reported dislocation densities of 10^{12} to 10^{14} cm^{-2} in their Ag-Cu composites deformation processed to $\eta = 4.6$; however, they, too, observed a decline in dislocation densities at high η values (up to 9.2) corresponding to average filament thicknesses of 10nm. They commented that the narrow confines of a 10nm thick filament may be be too small to permit Frank-Read sources to generate dislocations. Their internal friction measurements of the same samples showed an internal friction maximum and elastic and shear modulus minima at a mean fiber diameter of 55nm ($\eta = 4.6$). Measurements of internal friction as η increased from 4.6 to 9.2 showed a

steady decline (corresponding to the declining dislocation densities), while the elastic modulus rose from 80 GPa to 120 GPa, and the shear modulus rose from 20 GPa to 55 GPa.

More recently, TEM and electrical resistivity observations [8,13,14,17,26] have been made at Ames Laboratory showing that deformation processed composite dislocation densities are actually nearer 10^{10} to 10^{11} cm^{-2}. The methods used to measure dislocation densities by TEM (including the convergent beam electron diffraction technique used to measure TEM foil thicknesses) have become more reliable in recent years with the availability of higher accelerating voltages in TEM and the advent of computer programs to assist in data assessment. For this reason, these more recent measurements are presumably more accurate. These Ames Laboratory studies of dislocation density also noted numerous instances of dislocation-free zones within the thinnest filaments.

Both the correct values of dislocation densities as well as their importance in deformation processing strengthening mechanisms have been the topic of extensive debate [16], and no consensus has been reached on the issue. Courtney, et alia, maintain that the very high dislocation densities (10^{13} or higher cm^{-2}) imputed to their model are erroneously derived, and that observed dislocation densities are consistent with their model over the range of strains for which it was developed ($1 < \eta < 10$). Courtney, et alia, also cite the tendency of dislocations to annihilate at interphase boundaries when phase spacings become very small (e.g. a few tens of nm) and concede the possibility that such small interphase spacings may become an appreciable contributor to the composite's overall strength at η values greater than 10.

Another factor proposed to explain the strength of a fine-scale composite material is the high "energy price" of nucleating dislocations in extremely thin phases. Placing a dislocation into a crystal lattice introduces a long-range strain field around the dislocation that is believed to asymptotically approach zero at distances of hundreds of lattice parameters from the dislocation. If, however, the dislocation is to be placed in a narrow phase field with

interphase boundaries only a few dozen lattice parameters away or even closer, the energy cost of nucleating such a dislocation can be calculated to be substantially higher than in large crystals far from interphase barriers that interrupt the dislocation's strain field. Koehler [27] calculated a strength due to this stress barrier effect of:

$$\sigma = \frac{GR}{8\pi}$$

where σ is the composite strength, G is the shear modulus, and $R = (\mu_2 - \mu_1)/(\mu_2 + \mu_1)$ with μ_1 and μ_2 being the shear moduli of the two phases. Koehler considers a lamellar phase structure where both phases deform. He calculated that the strength σ will be observed when a composite has a critical degree of microstructural refinement wherein the softer phase has a thickness t:

$$t = \frac{32\pi b}{R}$$

where b is the magnitude of the Burger's vector in the softer phase. Koehler's relation predicts that at this critical thickness, Frank-Read source dislocation generation would be effectively stopped, and the material would be at its theoretical strength of approximately $\mu/30$ (where μ is the shear modulus). Therefore, making the layers finer still could impart no additional strengthening. Although the Koehler model was calculated for ultra-thin lamellar layers produced by sputtering rather than for filamentary microstructures, the basic premise should remain qualitatively valid for nanofilamentary composites. Indeed Koehler's theory is found to fit poorly to nano-scale filamentary material [21,28] where it predicts a critical thickness for the phases of about 200nm, yet no maximum in strength is observed in Cu-Nb composites at thicknesses an order of magnitude smaller than this. One must bear in mind

that in an extreme case where filament thicknesses were about one nanometer (3 or 4 atoms thick), the composite phase size would be only slightly greater than the diameter of a single atom, and the composite would be close to becoming just a supersaturated solid solution, which would be expected to have a far lower strength.

In summary, the mechanisms at work in producing the anomalously high strengths of deformation processed composites are still incompletely understood. The basic principle of science calls for conducting an experiment in which one factor is changed while all others are held constant. In the case of deformation processed composites, as in so many other problems in materials science, such experiments are nearly impossible to design. Increasing η not only increases the strength of the composite, but it also changes the interphase spacing, dislocation density, filament morphology, and crystallographic texture in the specimen. Correlating cause with effect becomes an exceedingly challenging enterprise in such systems. It is little wonder that even twenty years of work in several laboratories has been insufficient to clearly define all the interrelationships of the many variables at play in deformation processed composites.

Crystallographic Texture in Cu-X Composites

All real crystals have some anisotropic properties. The elastic modulus of copper, for example, is 193 GPa in the <111> direction, but only 69 GPa in the <100> direction [29]. Properties such as Poisson's ratio, yield strength, and ultimate tensile strength are also anisotropic, even in cubic metals. Since these key mechanical properties vary substantially from one direction to another within a crystal, it is not surprising that plastic deformation of polycrystalline metals tends to impart a preferred orientation to the many grains which comprise the deformed piece. The crystallographic planes and directions of easiest slip are typically seen to tilt during plastic flow to positions which permit the lowest energy

deformation. As a result, the statistical distribution of these grains' orientations is no longer random, but becomes "clustered" around directions which promote easier deformation. This preferred orientation is usually referred to as "texture".

Deformation processed composites are heavily textured. Both x-ray diffraction and electron diffraction in a TEM have been employed to measure the preferred orientations of the matrix and second phases. In Cu-10Fe deformation processed composites, Biselli and Morris [24] employed both measuring techniques and learned that the Fe filaments assume a strong <110> fiber texture, that is, the <110> direction of individual Fe grains tends to lie parallel to the specimen's cylindrical center line, as shown in Figure 2. Such <110> fiber texture is typical of single-phase bcc metals subjected to axisymmetric deformation (extrusion, swaging, wire drawing). At low η values, Bisselli and Morris reported the Cu matrix showed a mixed texture of <001> and <111> with the preponderance of grains in the <001> orientation. This is somewhat similar to the fiber texture observed in pure Cu rods after axisymmetric deformation; in pure Cu both textures occur but the <001> is seen in about 25-35% of the grains with the balance in the <111> orientation [29]. As deformation progressed to higher η values, they observed an increase in the <111> fraction. It has been observed that the proportional split between <001> and <111> in fcc alloys is a sensitive function of stacking fault energy [30], which would be affected by impurity content in the Cu lattice. Biselli and Morris reported an appreciable amount of Fe in solution in their Cu matrix, which may account for the difference in the ratios of the two orientations.

Several studies at the Ames Laboratory have employed both TEM electron diffraction as well as x-ray diffraction to measure the texture of various deformation processed Cu-X alloys. Verhoeven and co-workers [8] used TEM electron diffraction in deformation processed Cu-15Ta and Cu-2Ag-15Nb to observe a <110> fiber texture in the bcc filaments and both <111> and <001> fiber textures in the Cu matrix. Trybus, Spitzig, and Chumbley [17] employed TEM electron diffraction on deformation processed Cu-20Nb wire and found

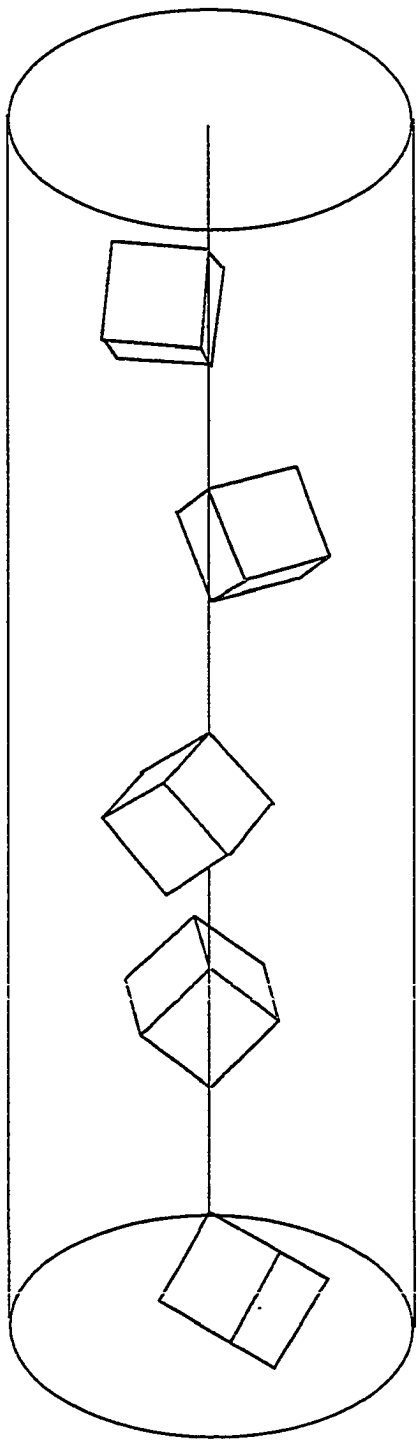

Figure 2. Illustration of the <110> fiber texture in a bcc rod. Each cube depicted represents a bcc unit cell with its <110> direction aligned along the rod axis

a <110> fiber texture in the Nb and a <111> fiber texture in the Cu matrix. Pelton, et alia, [26] used TEM electron diffraction to study deformation processed Cu-20Nb and found a <110> fiber texture in the Nb and a mixed <111> and <001> fiber texture in the Cu matrix. Silimperi and Russell [31] used x-ray diffraction to observe a predominantly <111> fiber texture with a weaker component of <001> fiber texture in the Cu matrix of a Cu-15Cr composite deformation processed to η values between 1.39 and 4.92.

These data for Cu-X deformation processed composites are quite consistent. The fcc Cu matrix acquires a <111> fiber texture, often accompanied by a <001> fiber texture, and the bcc second phase filaments assume a <110> fiber texture. Figure 2 shows a schematic representation of several bcc unit cells aligned with a <110> rod texture. Note that the unit cells have rotational freedom to position themselves in any angular position around the rod axis while still preserving their <110> texture. A review of the slip systems available in these metals can provide some insight into why these textures form.

Since dislocation strain energy is proportional to the square of the Burger's vector magnitude, slip in the direction offering the shortest possible Burger's vector is favored. For the same reason of minimizing the energy of dislocation motion, slip tends to occur on planes with the widest possible separation from adjacent planes of the same kind. Since the most widely spaced planes in a lattice are also the closest packed, low index planes are favored. Thus, it is generally observed that slip occurs on the closest-packed plane in the direction of closest packing.

In the fcc unit cell, axially symmetric flow can readily occur with either the <111> or <001> fiber texture because these orientations have three and four slip directions respectively to accomodate plastic flow. This is demonstrated by the deformation processed Ag-Cu composites [3] studied by Frommeyer and Wassermann which show approximately circular phase cross sections in the transverse plane for both the Ag and Cu phases (both of which are fcc).

In the bcc unit cell, the situation is more complicated. The closest packing direction is the <111> cube body diagonal, but there is no plane with maximum packing efficiency. The most closely packed family of planes in the bcc lattice is the {110}, but other planes such as the {112} and {123} are nearly as widely spaced and have also been observed to act as slip planes. In general, bcc metals are observed to slip in the <111> direction with often complex combinations of cross slip occuring on various low index slip planes.

When a polycrystalline bcc metal specimen is deformed axisymmetrically, the <110> direction would be expected to align itself with the specimen's cylindrical center line, because this orientation will maximize the critical resolved shear stress (Schmid factor) for the <111> slip direction on the low index planes. Indeed, this alignment is observed in single-phase bcc metals, as well as in the bcc filaments of deformation processed Cu-X composites. It is also accompanied by a characteristic "curled" shape of the grains in a bcc metal so textured (see Figure 3).

Hosford [32] offered an explanation for this peculiar curling of grains in drawn wires of bcc metals. As shown in Figure 4, when the bcc crystal is oriented with <110> parallel to the specimen's center line, two of the four <111> directions (the $[1\bar{1}1]$ and the $[\bar{1}\bar{1}1]$) are positioned perpendicular to the center line and thus cannot slip. All slip is limited to the remaining two <111> directions (the [111] and the $[\bar{1}11]$) which lie opposite one another across the specimen center line. These two slip directions are geometrically incapable of responding to deformation by producing a symmetric flow of the crystal wherein an initially equiaxed grain gradually becomes cigar-shaped and then finally a long, approximately cylindrical filament as deformation progresses. Instead, it responds to the deformation by expanding in the [011] direction to elongate into a filament, but in so doing it must contract in the [100] direction. Neither contraction nor expansion occurs in the $[0\bar{1}1]$ direction, so the shape change of the bcc crystal is reduced to plane strain with all plastic flow confined to the $(0\bar{1}1)$ plane.

Figure 3. Conical scan dynamic dark field TEM micrograph of Cu-20Nb deformation processed to $\eta = 7$. Note the characteristic "curling" of the Nb filaments necessary to accomodate their plane strain deformation mode

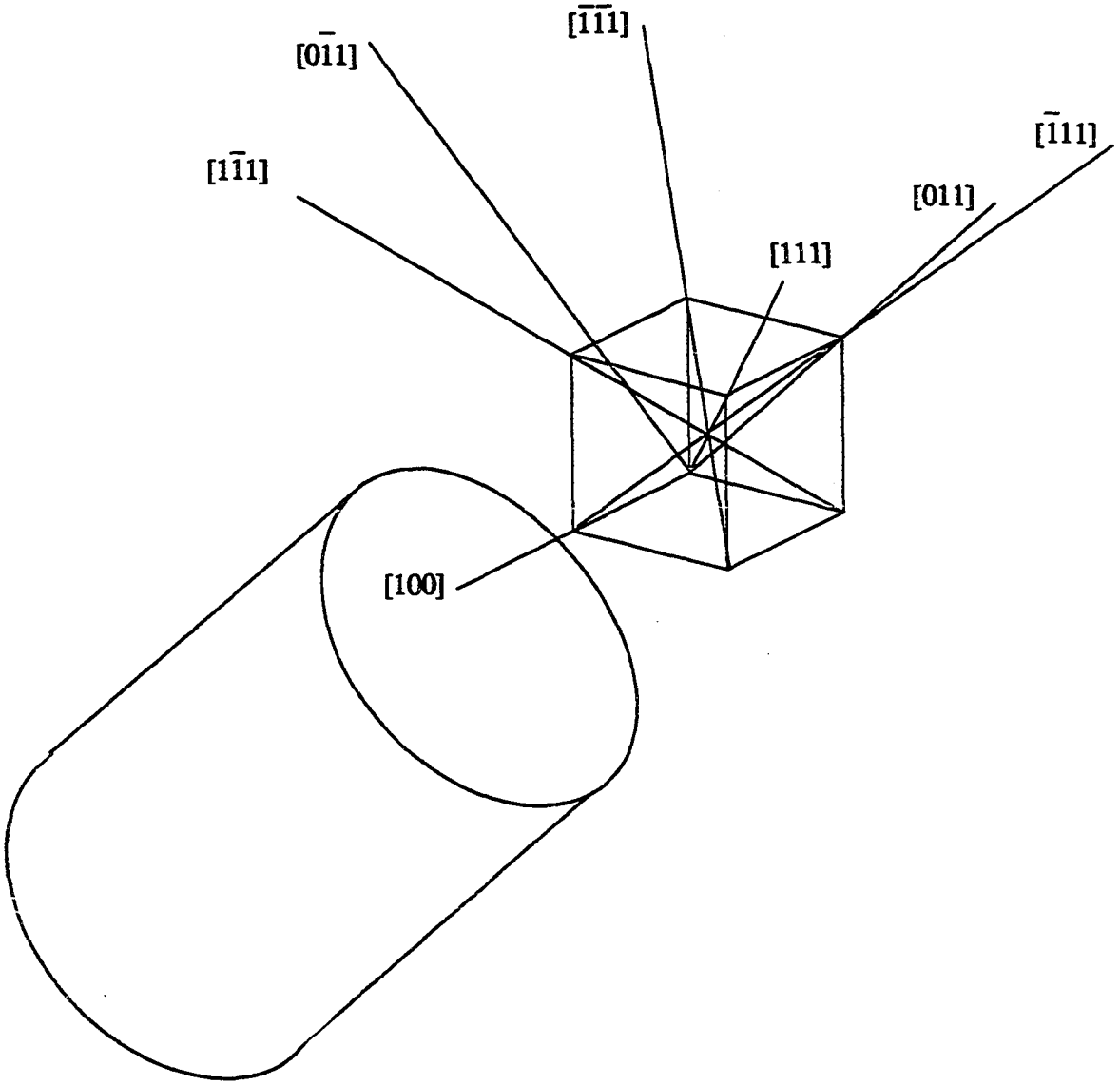

Figure 4. In a bcc crystal with a <110> fiber texture, two of the four <111> directions (the [$1\bar{1}1$] and the [$\bar{1}\bar{1}1$]) are positioned perpendicular to the center line and thus cannot slip. All slip is limited to the remaining two <111> directions (the [111] and the [$\bar{1}11$]) which lie opposite one another across the specimen center line

Hosford calculated that for any of the low index slip planes known to be active in bcc metals, the stress to produce axially symmetric flow is 1.5 times greater than the stress required for plane strain flow in the $(0\bar{1}1)$ plane. In drawn single-phase bcc metal, the grains bend around one another to allow each to undergo this energetically favored plane strain deformation. Hosford speculated that the extra slip required for this grain bending would be considerably less than the difference between plane strain and axisymmetric strain.

In the Cu-X deformation processed composites, much the same behavior is observed for the bcc phase. The bcc crystals assume the <110> fiber texture, and plane strain is still the lowest energy deformation mode, but the bcc phase is surrounded mostly by axisymmetrically deforming fcc-Cu. Consequently, the flattening of the bcc filaments from their plane strain is constrained by the axisymmetrically deforming fcc Cu crystals and results in the curling and folding effect evident in Figure 3. Thus, for an equivalent amount of deformation, Cu-X deformation processed composites have a much thinner effective filament thickness and a much larger interfacial area than do fcc-fcc deformation processed composites like Ag-Cu or Ag-Ni. The deformation processed Ag-Cu wire of Frommeyer and Wassermann [3] is comprised of 100% fcc fibers which deform axisymmetrically, and these specimens achieved much lower maximum UTS values (1250 to 1400 MPa) even at filament thicknesses of only 12 to 25nm. Bevk, et alia [6] suggested that the presence of a plane straining phase is one of the reasons for the superior strength of the Cu-X composites.

The plane strain mechanism active in the bcc phase of the Cu-X composites is expected to be involved in both phases of a deformation processed Ti-Y (hcp-hcp) composite, as described in the "Results and Discussion" section. If one or both phases in Ti-Y composite deform in plane strain, unusually high ultimate tensile strengths in a high-η Ti-Y composite would tend to confirm the assumption that the phase shape resulting from the plane strain mechanism is a key contributor to the high strength of Cu-X composites.

EXPERIMENTAL PROCEDURE IN PREPARING AND DEFORMATION PROCESSING A Ti-Y COMPOSITE AND A Ti CONTROL SPECIMEN

Producing a non-cubic, two-phase deformation processed composite would provide a new perspective from which to assess the effects of both phase spacing and texture on the properties of the composite. In an attempt to produce such a non-cubic in-situ composite alloy, two candidate metals were sought possessing good ductility, a binary phase diagram with mutual immiscibility and without intermetallic compounds, and roughly similar mechanical properties and melting temperatures. One combination of metals meeting these criteria is a Ti-Y alloy. Both of these metals are hexagonal close packed (hcp), and their elastic constants, c/a ratios, and densities are nearly identical. Figure 5 shows the Ti-Y phase diagram [33].

A Ti-Y composition of 80% by volume (80 vol%) Ti and 20 vol% Y (hereinafter called Ti-20Y) was selected for this experiment to match the volume ratios of 80 vol% Cu and 20 vol% X (where X=Cr, Fe, Mo, Nb, Ta, V, or W) frequently used in the well-studied Cu-X systems. The alternative possibility of an alloy comprised of 80 vol% Y and 20 vol% Ti was not chosen since Y is substantially more expensive than Ti, and the physical and mechanical properties of Y [34-35] are less well known than those of Ti.

The initial Ti-20Y alloy was formed by co-melting Ti sponge purchased from TIMET in Henderson, NV with Y from the inventory of the Materials Processing Center (MPC) of the Ames Laboratory in Ames, IA. The pure Ti control specimen was also produced using this same Ti sponge from TIMET. The Ti sponge analytical report provided by TIMET indicated the impurities listed in Table 1. This Ti sponge is substantially lower in impurity content than commercial grade Ti, which would typically have over 1000 ppm O for the low interstitial grade Ti or 2000 to 4000 ppm O for ordinary Ti sponge. The concentration of other impurities is similarly low in the Ti sponge used for this ecperiment.

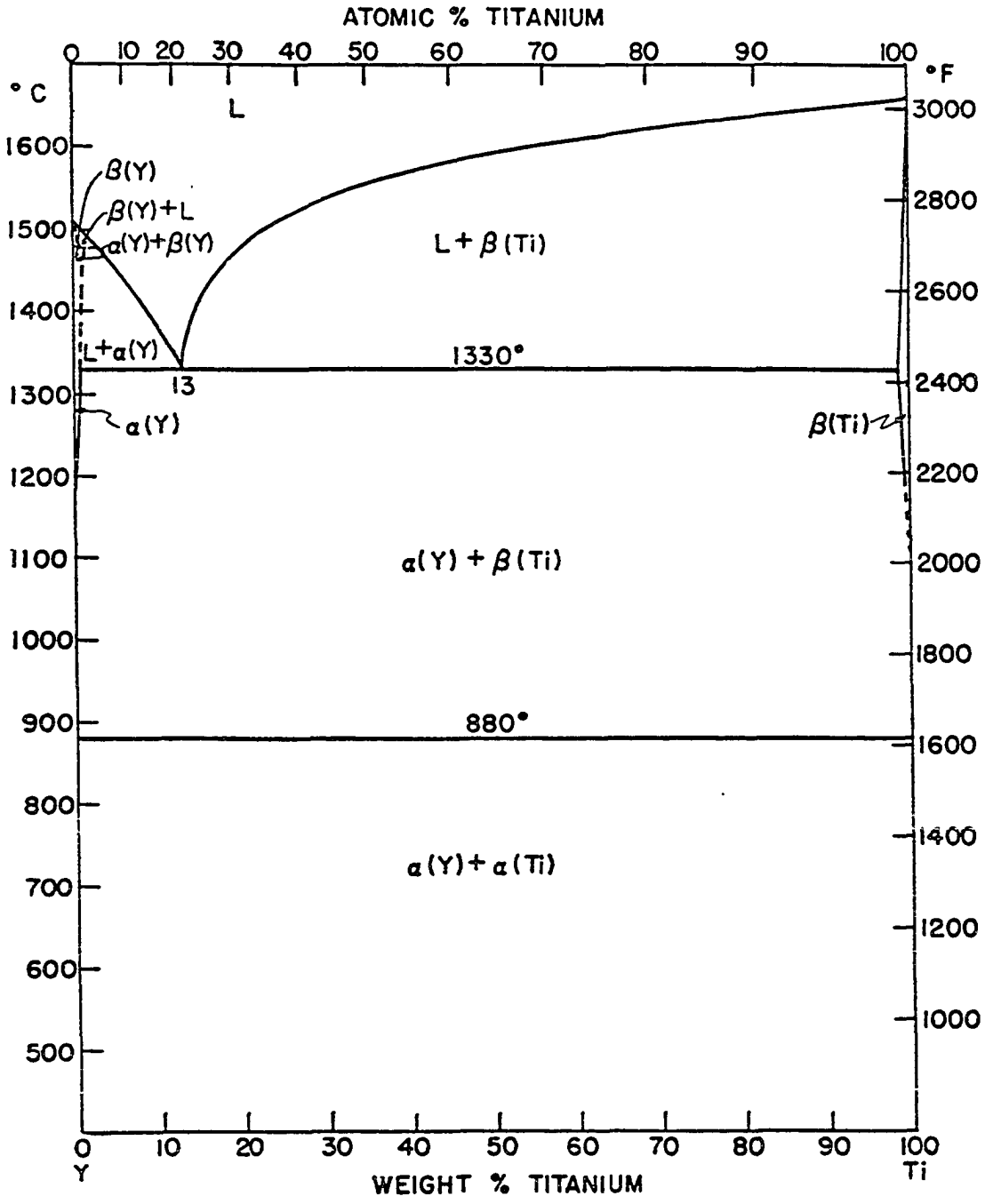

Figure 5. Equilibrium binary phase diagram for Ti and Y from Bare and Carlson [33]

Table 1. Impurity assay of titanium sponge used to produce Ti-20Y composite specimens (Source: TIMET Inc.)

Element	content in wt ppm
O	210
Pd	<100
Al	90
Mg	<60
Cu	50
Sn	<50
N	10
B, Cr, Fe, Mn, Mo,Ni, Si,V, & Zr	<10
Y	<4

The O and N analysis from TIMET in Table 1 is in approximate agreement with the analysis performed on this TIMET sponge at the MPC of the Ames Laboratory, which indicated O content of 171 wt ppm, N content of 6 wt ppm, as well as a C content of 81 wt ppm.

Although it was designated "high purity", the Y provided by the MPC lacked a complete analysis of its impurity content. A gas fusion analysis of this Y for interstitial impurities indicated O content of 976 wt ppm, N content of 103 wt ppm, and C content of 102 wt ppm. Although the O content of the Y was substantially higher than the O content of the Ti used, the cost of using Y with lower O content (e.g. distilled Y) would have been prohibitive.

These two metals were prepared for casting by machining (without lubricating fluid) the Y ingot on a lathe to reduce it to turnings which could be pressed with the pieces of Ti sponge to produce a rod-like electrode of 80 vol% Ti and 20 vol% Y. This electrode was then consumably arc melted into a water-cooled Cu mold to form a 76mm nominal diameter cylindrical casting (MPC record number F4-1-47). A cylindrical disc about 10mm thick

from the top of the rough casting was cut away to provide material for measurement of the Ti-20Y as-cast microstructure, tensile properties, crystallographic texture, and interstitial impurity content. The remainder of the casting was then machined to remove surface flaws formed at the mold wall, yielding a final cylinder 74.15mm in diameter, 91.60mm long, with a mass of 1780 g. The casting appeared sound; no voids or cracks were visible on the machined surfaces.

A second ingot of pure Ti (MPC record number F4-1-48) was consumably arc melted in the same manner from the same lot of TIMET Ti sponge to produce a control specimen of final machined dimensions 74.90mm in diameter, 78.50mm long, with a mass of 1550 g after a portion had been removed for measurement of the control specimen's as-cast microstructure, tensile properties, crystallographic texture, and interstitial impurity content.

The final machined castings of Ti-20Y and pure Ti were cleaned in an ultrasonic bath of trichloroethane to remove possible surface oil films and loaded into a thick-walled steel can machined from a solid billet of SAE 1018 steel, as shown in Figure 6. The two specimens were separated by a cylindrical SAE 1018 steel spacer 75mm in diameter and 31.5mm high. All internal can wall surfaces and spacer surfaces were also cleaned ultrasonically in trichloroethane. An end cap of SAE 1018 steel was electron beam welded in place, sealing the specimens inside a steel cylinder of approximate internal pressure 10^{-4} Torr. The sealed steel can was used to protect the Ti-20Y and pure Ti specimens from exposure to the atmosphere during the 800° C. extrusion planned to begin the deformation processing of the specimens.

The steel cylinder welded around the Ti-20Y and pure Ti specimens had a 95mm O.D., and it in turn was inserted into a Cu sleeve of 102mm O.D. (see Figure 6). The Cu sleeve was used to lubricate the extrusion die. The Cu sleeve/steel can assembly was then held in a furnace at 800° C. for four hours and placed in a 700-ton extrusion press to be extruded through a 25mm die. This first attempt at extrusion failed; the press had insufficient

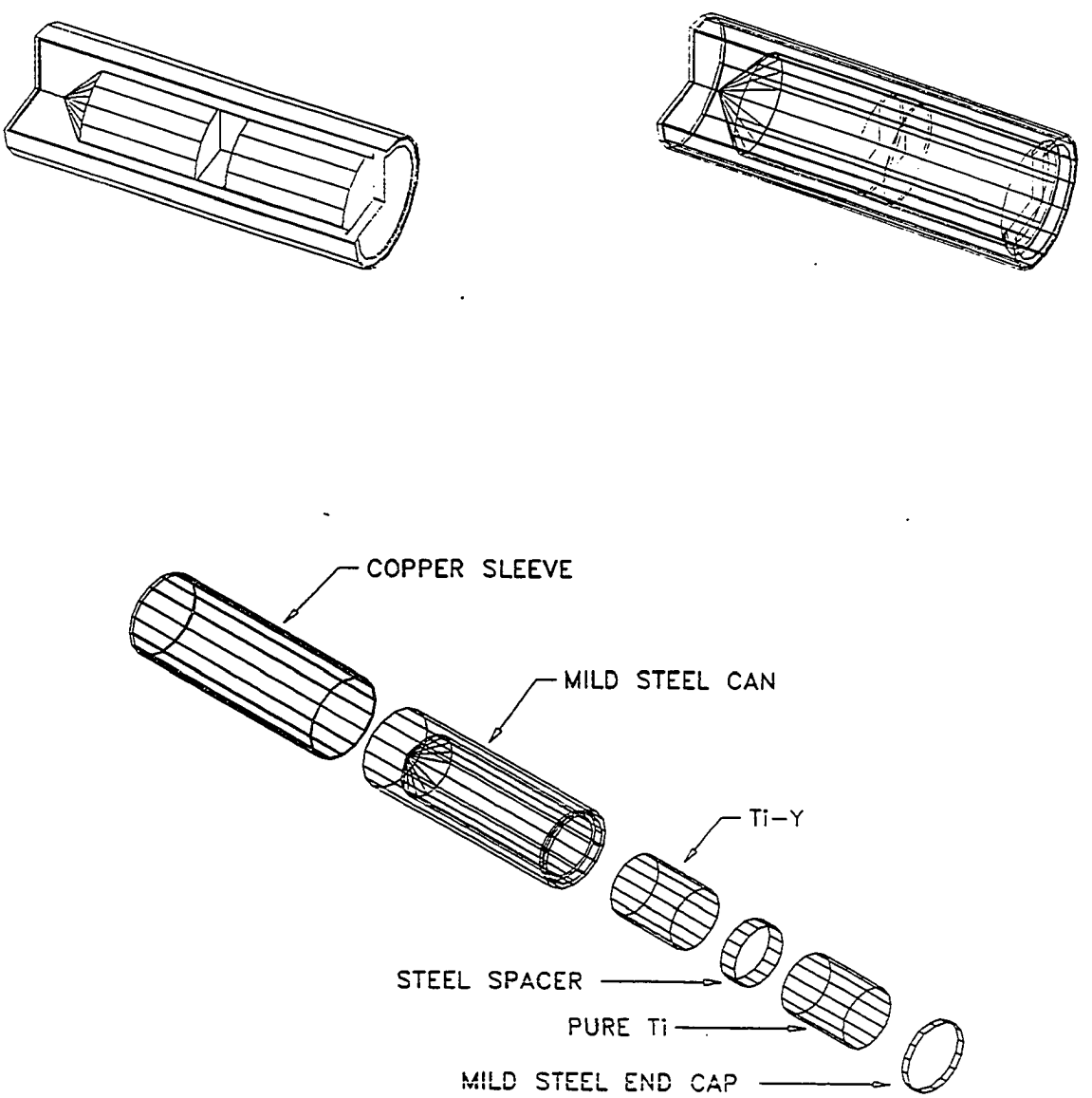

Figure 6. Wire-frame depictions of the extrusion can assembly for Ti-20Y and pure Ti ingots shown in pictorial half section views with and without hidden line removal (top) and in exploded pictorial (bottom). The forward end of the assembly is at left

force to push the canned specimens through a 25mm die. A small portion of the can nose was extruded before the press stalled, but the vacuum integrity of the can was not breached. The 25mm extruded portion was sawed away, and another attempt was made to extrude the assembly after an additional four hour soak in an 800° C. furnace. On this second extrusion attempt, a 33mm diameter die was used to reduce the force necessary to push the assembly through the die. This second extrusion attempt was successful, and the resulting rod (2.01m long and 33mm in diameter) was air cooled.

The middle 80% of the length of the extruded rod consisted of a 24mm diameter core of Ti-20Y/pure Ti encased in a steel tube of approximately 3.5mm wall thickness, which was in turn encased in a copper tube of 1mm wall thickness. The extrusion from a 75mm diameter to a 24mm diameter is a true strain(η) of 2.25. A band saw was used to cut the extruded rod into several shorter pieces, separating the Ti-20Y portion from the pure Ti portion and removing the nose, tail, and spacer sections which consisted of steel and Cu with no Ti-20Y or pure Ti within. In order to provide material for analysis and properties measurement, 250mm lengths of the Ti-20Y and pure Ti portions were cut and retained in Ames, while a 600mm length of Ti-20Y and a 500mm length of pure Ti were shipped to G & S Titanium Company in Wooster, Ohio for further deformation.

At G & S Titanium Company, the initial as-extruded specimens were swaged at room temperature while still in their steel and Cu jackets. Swaging was performed in stages with a 60% reduction in the specimen cross sectional area followed by a 30 minute stress-relief anneal in air at 700° C.; this was in turn followed by another 60% reduction in area by swaging followed by another 30 minute anneal in air at 700° C., and so forth until the specimens had been reduced to a 2.5mm diameter. The thin outer layer of Cu disintegrated rapidly in the early part of this room temperature swaging process, leaving steel-clad Ti-20Y rods and steel-clad pure Ti rods.

At a diameter of 2.5mm, both specimens were placed in a H_2SO_4 acid bath to etch away the steel jackets and expose the Ti-20Y and pure Ti. The deformation processing of the pure Ti was stopped at $\eta = 7.27$. Subsequent deformation was performed on the Ti-20Y material by room temperature wire drawing in dies with an 8° taper reducing the diameter by 20% in each pass. The wire drawing followed the same precept used in swaging: 60% reduction in area, followed by a 30 minute anneal in an inert atmosphere at 700° C., repeated several times until the specimens reached a final diameter of 0.127mm (true strain of 12.8). Coupons were removed from the specimens at several intermediate diameters for analysis and physical properties measurements.

After this deformation processing was completed, tensile test and TEM measurements on the Ti-20Y specimens deformed to η values in the range of 9.24 to 12.8 indicated that the 700° C. annealing temperature used was high enough to permit recrystallization of both the Ti and Y phases. This recrystallization changed the characteristic "convoluted ribbon" filamentary structure (shown in Figure 3 and in the "Phase Spacing Measurements and Phase Morphology Observations" section) to an approximately equi-axed grain structure with a substantially lower ultimate tensile strength. In an effort to produce Ti-20Y at higher η values with the convoluted ribbon structure, a 100mm long piece of steel-jacketed Ti-20Y rod which had been deformed to $\eta = 5.03$ at G & S Titanium was hot worked at 700° C. to $\eta = 5.71$. This rod, still encased in its steel jacket, was subsequently swaged at room temperature to $\eta = 10.0$ with periodic 20-minute anneals at 600° C. after each 25% reduction in area. A piece of the steel-jacketed pure Ti control material was also deformation processed in an identical fashion to $\eta = 10.0$.

Although most of the Ti-20Y specimen broke apart in the range of $8 < \eta < 9.5$, one piece remained intact to $\eta = 10.0$. The pure Ti control specimen experienced no breakage during swaging from $\eta = 5.03$ to $\eta = 10.0$. The Ti-20Y and pure Ti swaged in this second run are hereinafter referred to as the "second generation" specimens.

TESTING PROCEDURES USED ON THE Ti-Y COMPOSITE AND THE Ti CONTROL SPECIMEN

Introduction to Testing Procedures

Four tests were performed on the Ti-20Y and pure Ti specimens at several points in the deformation processing sequence:

1. gas fusion analysis to measure changes in interstitial (O and N) impurity content
2. tensile testing to measure mechanical properties (ultimate tensile strength and ductility as per cent reduction in area)
3. x-ray diffraction texture analysis to measure preferred crystallographic orientation
4. scanning electron microscopy (SEM) and transmission electron microscopy (TEM) to measure phase size and shape

The experiment was designed to measure the four materials properties described above at several different levels of deformation processing.

Gas Fusion Analysis for Measuring Interstitial Impurity Content

The mechanical properties of Ti are quite sensitive to the presence of interstitial impurites (O, H, C, and N). [35, 36] Changes in the concentrations of these impurities amounting to only a few hundred parts per million can substantially increase the strength and decrease the ductility of Ti. Consequently, analysis for O and N (the most likely of these interstitial solutes to contaminate the specimens from air leaks in vacuum systems) was conducted to assure that any strength increases observed were not caused by diffusion of O or N into the metals.

Gas fusion analysis consists of vaporizing a 0.1 gram piece of the sample and quantitatively analyzing the weight of O and N released. Specimens were cut from samples of both pure Ti and Ti-20Y deformation processed to $\eta = 0$ (as-cast), 2.25 (as-extruded) and 6.68. A sample of the Ti-20Y deformation processed to $\eta = 12.2$ was also analyzed.

X-ray Texture Measurement Procedures

As shown in Figure 7, transverse cross section specimens were cut from the pure Ti and the Ti-20Y composite at deformation levels of $\eta = 0$, 2.25, and 5.03. X-ray texture specimens were not prepared for specimens with $\eta > 6.8$ due to the difficulty in preparing a transverse section of fine wires with a large enough area to produce a strong diffraction signal. Each specimen was metallographically polished through a 1-μm abrasive and then electropolished in perchloric acid to remove surface material disturbed by abrasive polishing.

The electropolished specimens were mounted on a Philips PW1078/50 texture goniometer, and an initial 2θ scan from 10° to 50° was made with unfiltered Mo x-rays ($\lambda(K\alpha_{1\ \&\ 2})$ and $\lambda(K\beta_1)$) to locate diffraction peaks. Each diffraction peak corresponds to a particular plane of diffraction in the Ti or the Y. Several of these diffraction peak angles were then selected for pole figure measurements of x-ray texture of that particular plane's orientation with respect to the specimen's rod axis. Data acquisition and analysis were performed by a Philips APD1700 Automated Powder Diffraction System. Each pole figure was acquired using a 5mm sample lateral oscillation and a 5° per spiral psi pitch, where psi is the radial angle on the pole figure. A 5-second sampling time was used with a 7.5° step in phi (where phi is the circumferential angle on the pole figure) between samplings. Measurements were begun at psi = 0° and halted at psi = 80°. Each pole figure required 68 minutes acquisition time.

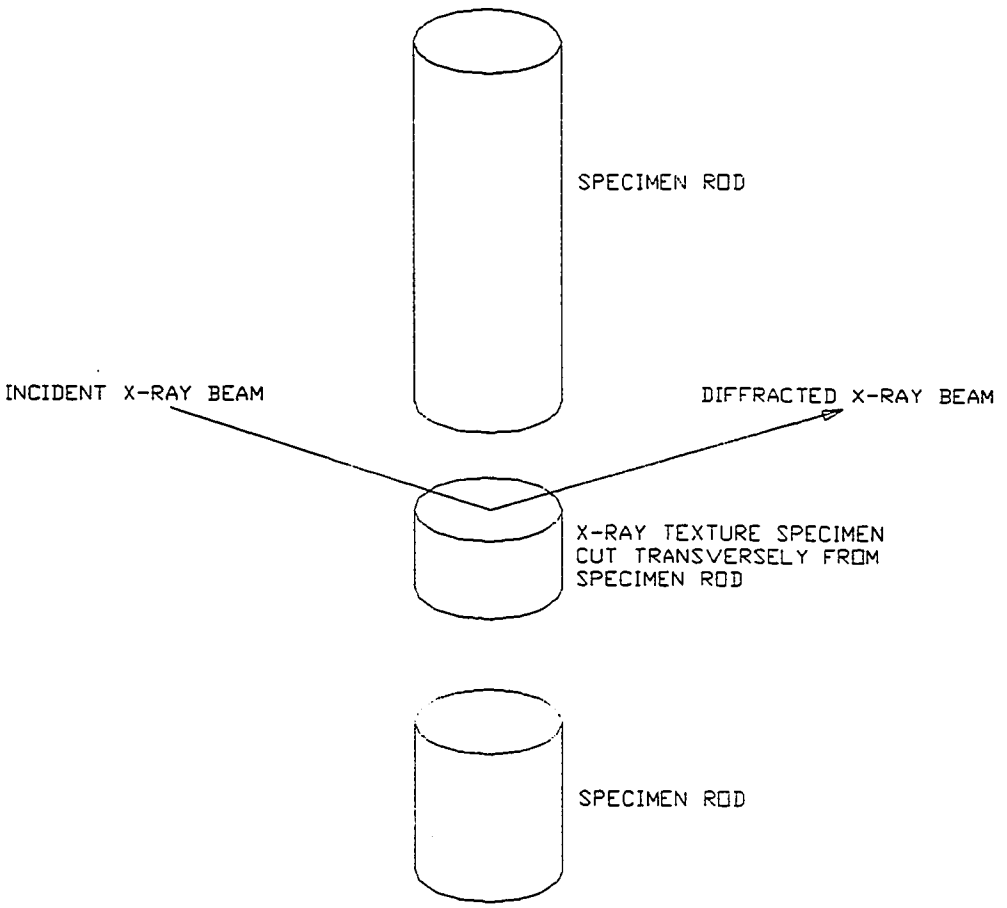

Figure 7. Method of cutting a transverse x-ray texture specimen from the main specimen rod

Tensile Testing Procedures

Tensile testing procedures for specimens in the range $\eta = 0$ to 9.2 followed ASTM Standard E8 [37], which requires a 4:1 ratio between the length and the diameter of the specimen gauge length. In the as-cast tests, specimens were cut radially from the upper surface of the Ti-20Y casting and from the lower surface of the pure Ti casting. All other tensile test specimens were simply machined in a lathe around the cylindrical specimen axis until ASTM E8 geometry was attained. Specimen gauge lengths were polished with 500-mesh abrasive paper to eliminate lathe tool marks around the gauge length circumference. Specimens in the range $\eta = 0$ to 9.2 were tensile tested on Instron 1125 and Instron 4505 tensile testing machines at a crosshead speed of 0.50 mm per minute. A minimum of two tensile specimens were made for each η value, except in cases where there was too little material available to make more than one specimen (see Table 4).

Specimens in the range $\eta = 9.2$ to 11 were wires of diameter 0.70 mm to 0.30 mm, and their small diameters made it impractical to machine them to the ASTM E8 geometry. The wires were fitted with soft Cu sleeves that slipped over the wire ends, leaving a gauge length of exposed specimen approximately four times the wire diameter between the copper sleeve ends. The Cu sleeves were cemented to the specimen wire ends, and the Cu was then forcefully compressed in a lathe collet while the cement was still wet to clamp it firmly around the specimen. Extremely light machining cuts were then made with a small rotating grinding stone (rather than a fixed cutting tool) on the rotating work piece to reduce the diameter of the specimen at the gauge length. During tensile testing, small pin vise grips were then tightened around the Cu sleeves to apply the tensile load. For these smaller tensile specimens, a crosshead speed of 0.12 mm per minute was applied.

The smallest tensile test specimens, where $\eta > 12$, were too fine to permit even the copper sleeve technique to be applied. Instead, a wire-pulling capstan device was used to apply the tensile load to an effective gauge length of 75mm. This capstan device thus gave a much larger ratio of gauge length-to-diameter (approximately 600:1 for the 0.127mm diameter wire of $\eta = 12.8$) than the 4:1 ratio specified in ASTM E8; however, no other means exist to provide tensile data on such fine wire. In this case, no attempt was made to reduce the diameter of the wire in the gauge length. Since tensile data are not critically sensitive to the length-to-diameter ratio of the specimen, it is believed that the capstan device still provides data approximately comparable to the data produced at the larger diameters, although the proportionally greater gauge length increases the possibility that an unrepresentatively low value of ultimate tensile strength may be produced due to the presence of an internal defect in the specimen's gauge length. This possibility can be reduced by testing several specimens, and this was done to the extent that material was available. A crosshead speed of 0.25 mm per minute was used with the capstan device tensile tests.

For all tensile tests, a value of engineering ultimate tensile strength was calculated from the quotient of the applied maximum load and the initial cross sectional area of the specimen. Ductility was calculated for each specimen by measuring the area of the fracture surface in a traveling microscope and comparing that area to the original cross sectional area of the specimen to calculate the per cent reduction in area.

Microscopy Procedures

Microscopy samples were made for both scanning electron microscopy (SEM) and transmission electron microscopy (TEM) to measure phase spacings and to allow visual

inspection of the phase morphology. SEM specimens were prepared at deformation levels of $\eta = 0$ (as-cast) and 2.25 (as-extruded). Both transverse and longitudinal cross section samples were made for the as-extruded samples. The samples were mounted in metallographic mounts and polished through a 1-μm diamond abrasive wheel with the final two polishing steps performed on oil-based abrasive suspensions (rather than water-based) to avoid any possible reaction between the yttrium and water. The large difference in the atomic numbers of Ti (22) and Y (39) provided excellent contrast between the two phases in the back-scattered electron imaging mode, and consequently no chemical etch was needed to show the phase boundaries in the SEM, a Cambridge S-200 unit operated at accelerating voltages of 15kV to 20kV.

TEM samples were prepared for deformation levels of $\eta = 5.03, 7.27, 12.3$ and 12.8. Sample discs were cut transversely with a diamond cut-off wheel and mechanically thinned on a VCR Group Dimpler and further thinned to perforation on a Gatan 600 ion mill using argon ions. The $\eta = 12.3$ and 12.8 specimen diameters were too small to permit direct sectioning, so three lengths of these wires were bundled and built up to a thicker cross section by electroplating Cu on the exterior of the bundle in a copper sulfate-sulfuric acid solution prior to cutting and thinning. A Philips CM30 TEM was used at an accelerating voltage of 300kV to photograph the TEM samples. Conical scan dynamic dark field imaging was employed in many of the TEM micrographs to distinguish between the Ti and Y phases in the TEM foils.

For specimens with ribbon-shaped phases, phase spacing determinations were made by measuring several hundred phase thicknesses across their short dimension and averaging these values. For all pure Ti specimens and for Ti-20 specimens with equi-axed phase shapes ($\eta > 7.27$), standard stereological techniques were employed to calculate phase sizes with the Heyn procedure, ASTM E112-63 [38].

RESULTS AND DISCUSSION

Gas Fusion Analysis Results

Oxygen and nitrogen have little effect on either strength or ductility in Y at the levels seen in these specimens [35]. However, O and N are powerful strengthening and embrittling agents in Ti [36], and for that reason it was necessary to monitor the content of these solutes in both the Ti-20Y and pure Ti specimens to avoid confusing strength and ductility changes caused by deformation processing with changes caused by increases or decreases in O and N content.

Based upon the gas fusion analyses performed on single samples for each line in Table 2 on the Ti and Y metal used to produce the initial castings, all Ti-20Y specimens should have had an O content of 332 weight ppm and a N content of 25 weight ppm, assuming no additional O or N were added to the specimens during casting and subsequent deformation processing. Similarly the pure Ti control specimen should have had an O content of 171 weight ppm and a N content of 6 weight ppm, assuming no additonal O or N was added to the specimens during casting and subsequent deformation processing. The O and N contents measured by gas fusion analysis are shown in Table 2.

Table 2. Gas fusion analysis results for Ti-20Y composite and pure Ti control specimens

SPECIMEN	O Content (wt ppm)	N Content (wt ppm)
Ti-20Y as-cast ($\eta = 0$)	827	37
Ti-20Y as-extruded ($\eta = 2.25$)	895	42
Ti-20Y ($\eta = 6.68$)	817	43
Ti-20Y ($\eta = 12.3$)	663	46
Pure Ti as-cast ($\eta = 0$)	434	21
Pure Ti as-extruded ($\eta = 2.25$)	499	32
Pure Ti ($\eta = 6.68$)	731	41

The N contents for both Ti-20Y and pure Ti show a slight increase from the casting and deformation processing, but the total N content, even at the highest level of 41 wt ppm, would be expected to have a negligible effect on mechanical properties. [36] The O contents in both specimens are substantially higher than the N contents but would still be considered low by industrial standards. The purest industrial grade Ti, ASTM Grade 1 ELI (extra low interstitial), has a specified maximum O content of 1000 wt ppm. Over the range of values seen (about 450 wt ppm), O increases the ultimate tensile strength in Ti by approximately 35 MPa [36]; and in Y the addition of 450 wt ppm O would have no discernible effect on ultimate tensile strength. [35] Since 25 MPa is only a few per cent of the amount of change observed in ultimate tensile strength during deformation processing (see data presented in the "Tensile Test Results" section), the effect of O content change was assumed to be a minor contributor to the observed changes in ultimate tensile strength.

No attempt was made to determine how the total O content was distributed between the Ti and Y phases in the Ti-20Y composite specimens. Both elements have a powerful affinity for O, and their ΔG of formation on a per atom basis is nearly identical: -212.6 kcal/mol for Ti and -216.5 kcal/mol for Y. [39] At equilibrium (an uncertain assumption in the rapidly cooled castings and subsequent processing operations), one might expect to see the Y take a slightly larger share of the O than the Ti, but the difference would presumably be small.

X-ray Texture Measurements

X-ray texture pole figures were acquired for both the pure Ti and Ti-20Y specimens at η levels of 0 (as-cast), 2.25 (as-extruded), and 5.03. The pole figures from the deformation processed specimens (i.e. those with $\eta > 0$) were taken in transverse cross section.

The as-cast ($\eta = 0$) specimen of pure Ti (Figures 8-10) shows essentially no texture. The pure Ti specimen had unusually large grain size, and this produces pole figures that give the appearance of a highly textured specimen. However, the as-cast pure Ti pole figures are essentially stereographic projections of the orientations of individual grains, rather than statistically significant distributions of the orientations of large numbers of grains. When several pole figures of the pure Ti are taken into consideration, there is no systematic pattern of grain orientation to suggest texturing.

The pole figures in Figures 11-13 for the as-cast ($\eta = 0$) Ti-20Y specimen show little evidence of texturing. The relative intensity levels span a small range from about 0.83 to 1.25, typical of a specimen without significant texture. Although one would expect some tendency for specific crystallographic alignments in the Ti-20Y dendritic structure, there is no long-range alignment of dendrites in the rapid cooling, vigorous mixing environment that prevails during consumable arc casting into a chilled mold.

The transverse cross section specimen of as-extruded pure Ti ($\eta = 2.25$) shows substantial evidence of texturing. This specimen was extruded at 800° C. through a die which reduced the specimen's diameter from 75mm to 25mm. Such a large deformation would be expected to introduce significant texture, and indeed the relative intensities in the pole figures for this as-extruded specimen range from as low as 0.39 to as high as 2.62. Figures 14 and 15 are pole figures for the as-extruded pure Ti; in each case the pole figure is consistent with a $<10\bar{1}0>$ fiber texture. The $<10\bar{1}0>$ fiber texture is the expected fiber texture for an axisymmetrically deformed pure Ti rod [29].

It should be borne in mind in comparing relative intensities on pole figures that different samples produce different total x-ray intensities, and thus, a maximum intensity of 10 on one sample is not directly comparable to a maximum intensity of 10 on a different sample.

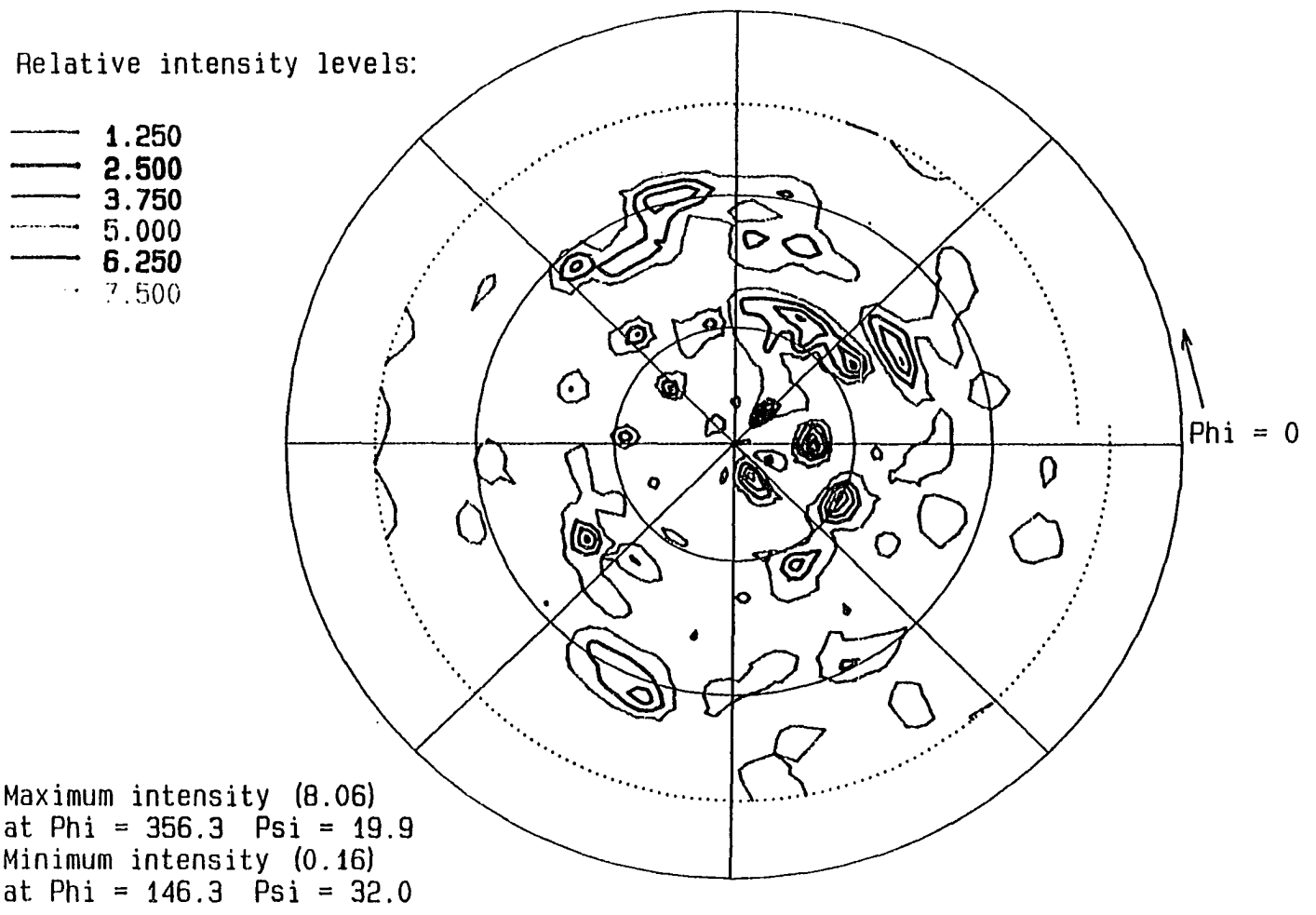

Figure 8. Pole figure for pure Ti as-cast ($\eta = 0$) on the $(01\bar{1}0)$ plane. Areas of high relative intensity correspond to individual grains in this coarse-grained specimen

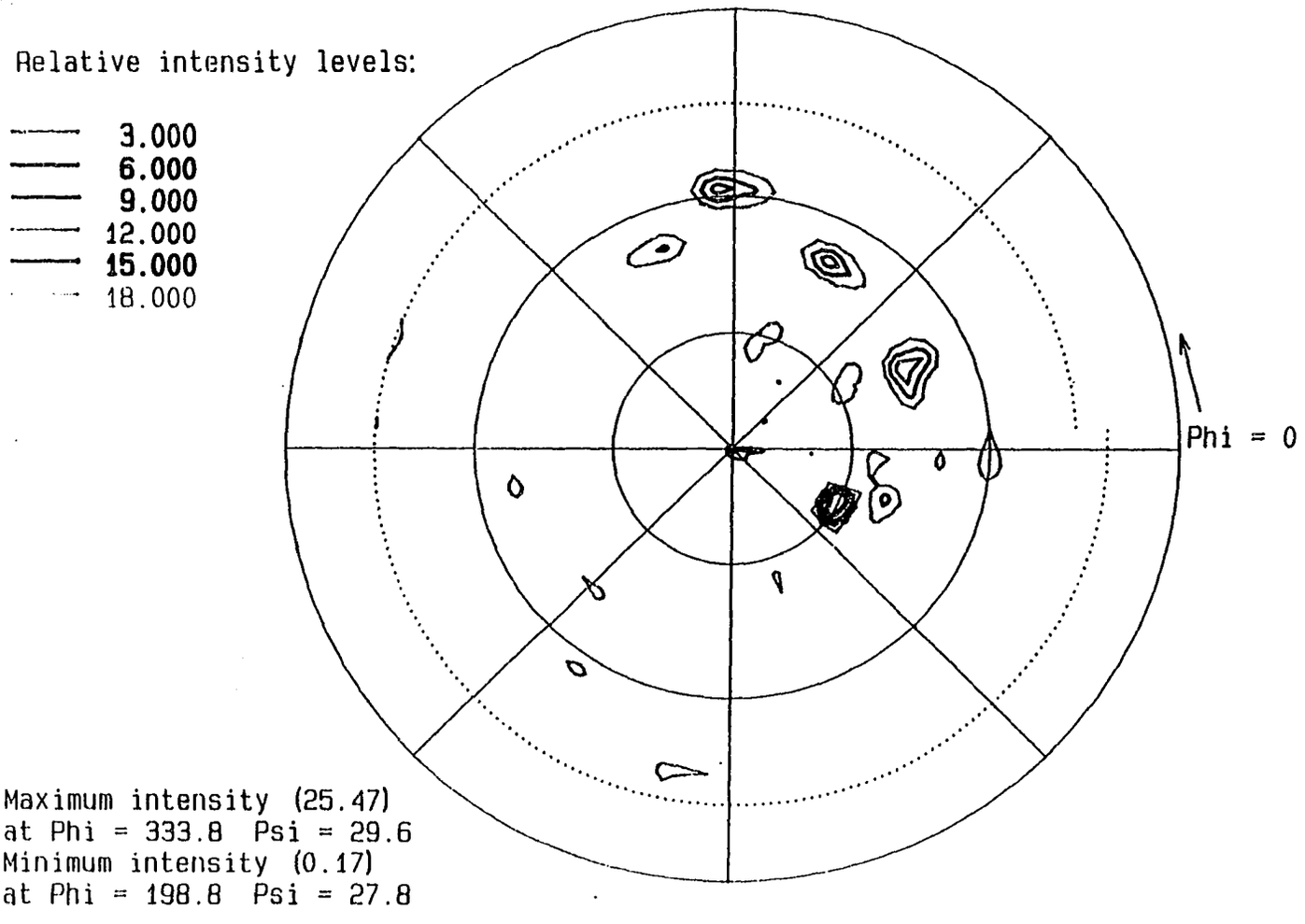

Figure 9. Pole figure for pure Ti as-cast ($\eta = 0$) on the (0002) plane. Areas of high relative intensity correspond to individual grains in this coarse-grained specimen

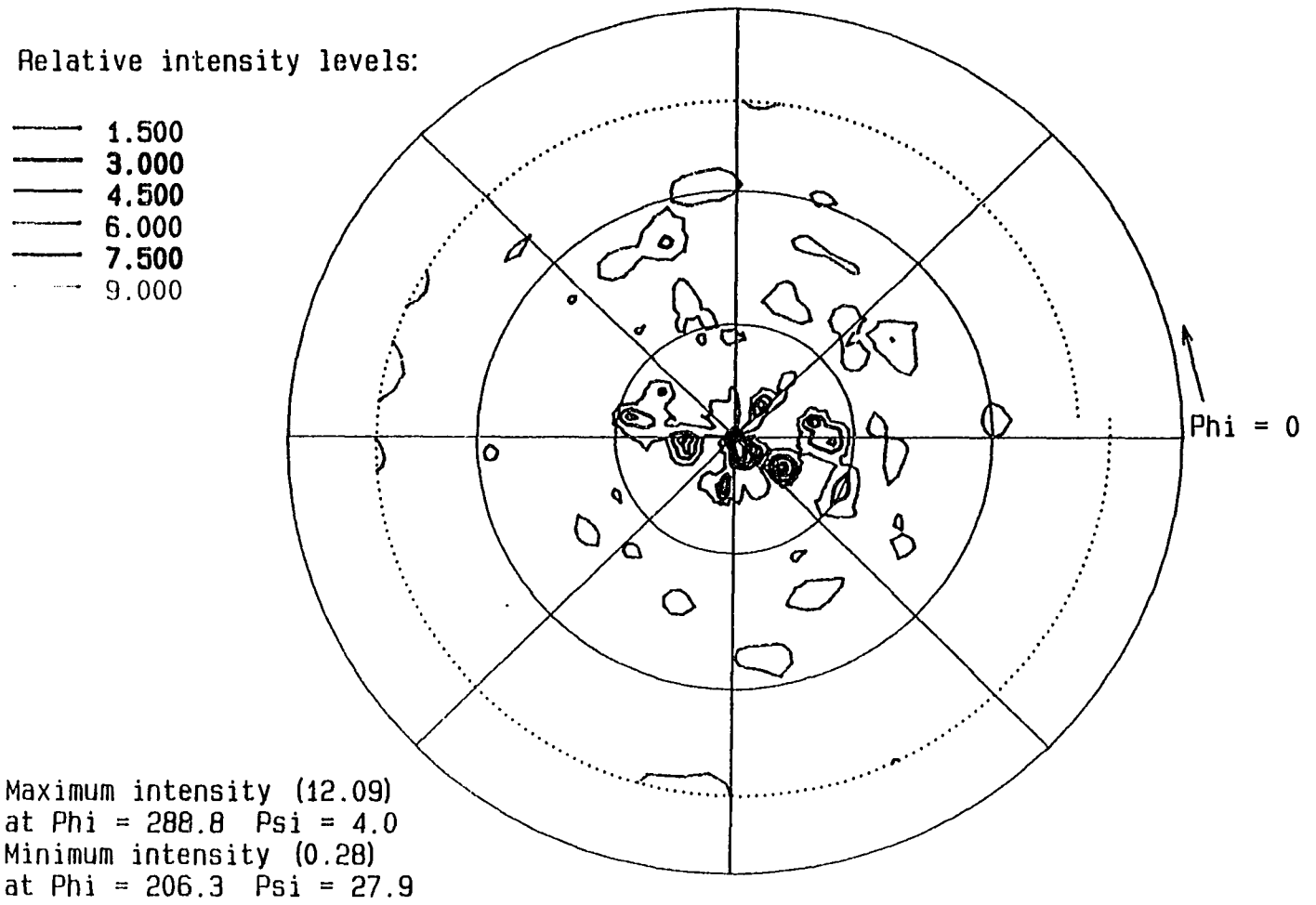

Figure 10. Pole figure for pure Ti as-cast ($\eta = 0$) on the $(01\bar{1}2)$ plane. Areas of high relative intensity correspond to individual grains in this coarse-grained specimen

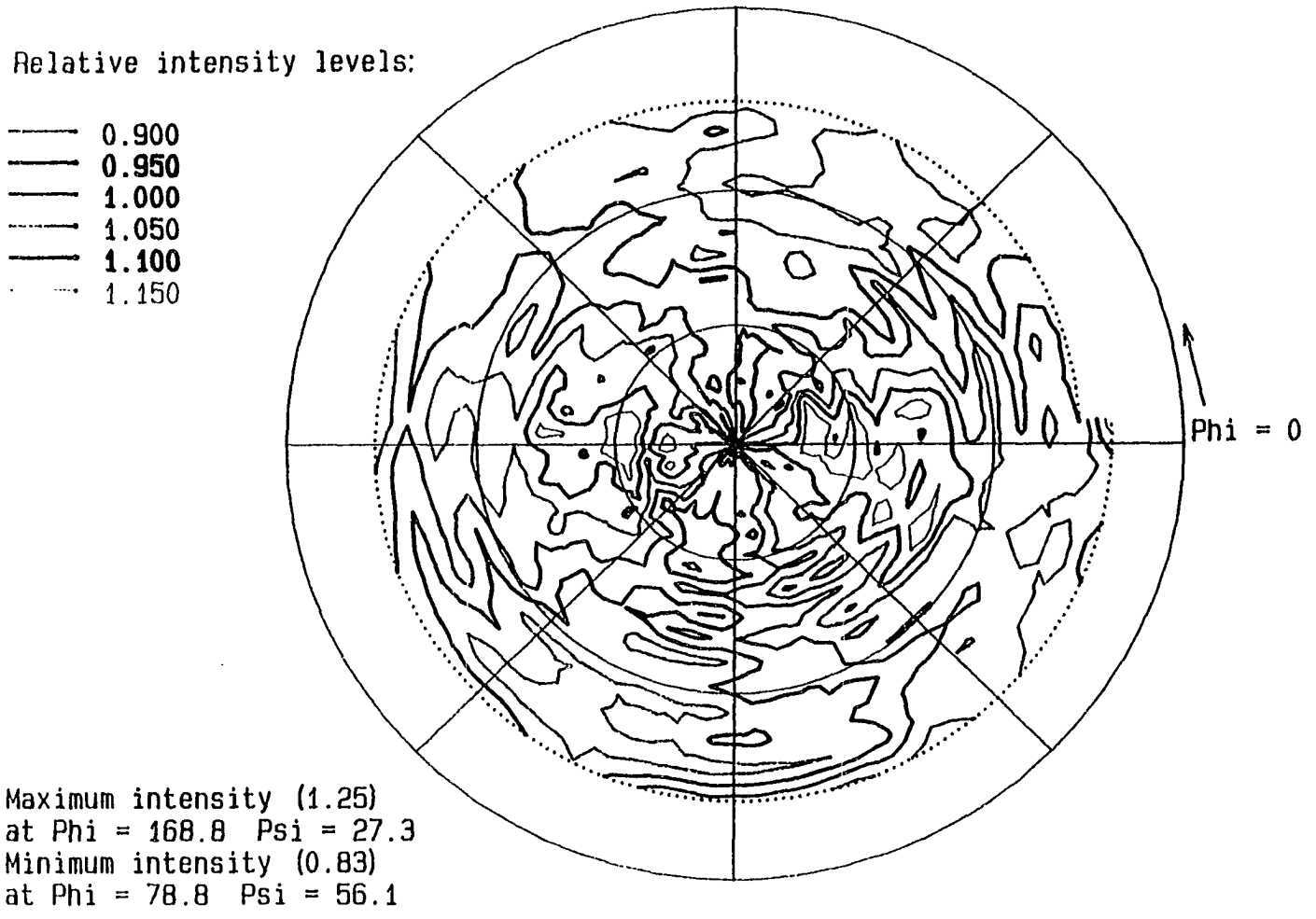

Figure 11. Pole figure for Ti-20Y as-cast ($\eta = 0$) on the Ti $(01\bar{1}0)$ plane. Note that all relative intensity levels are near unity , as is typical of a specimen with little texture

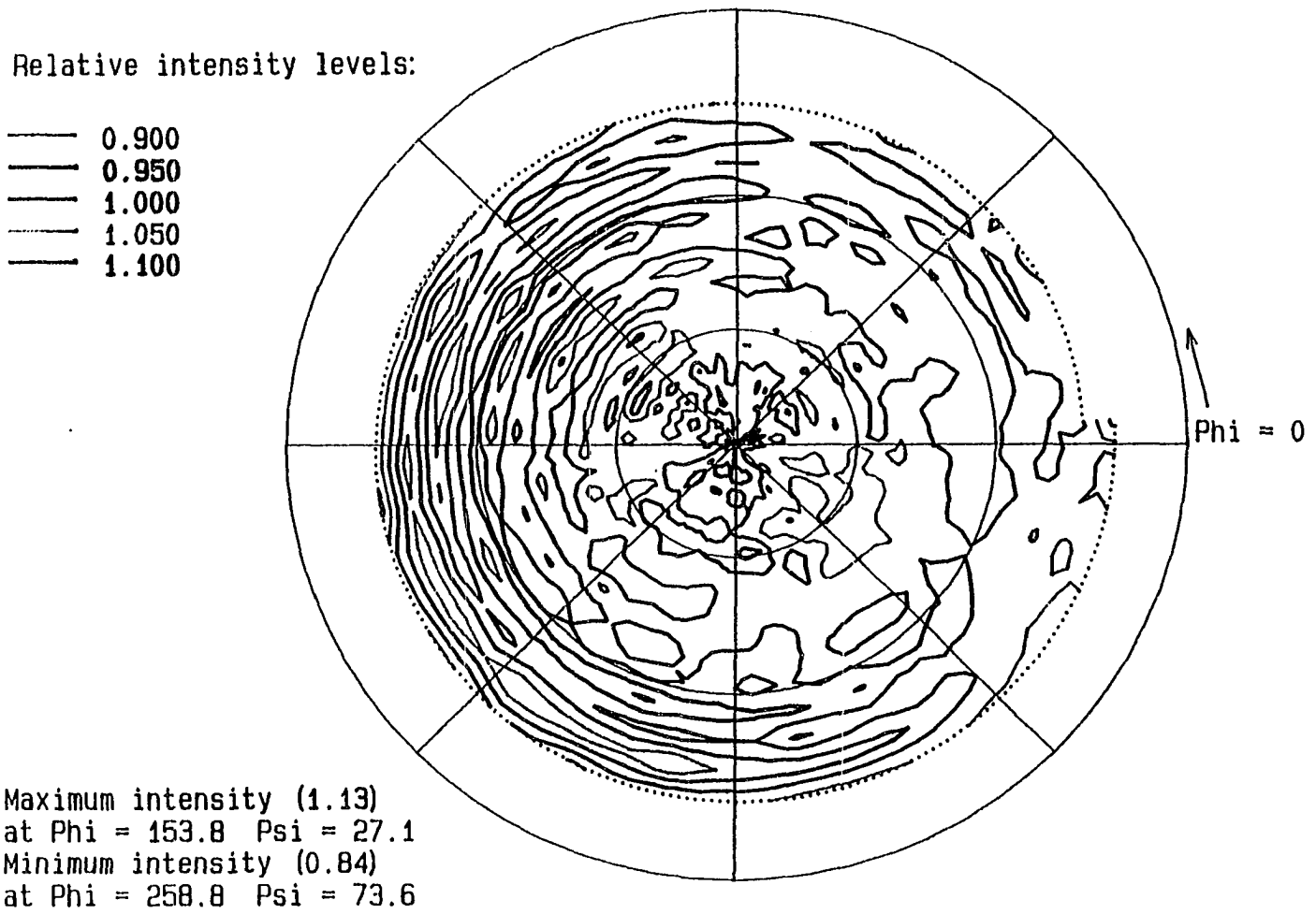

Figure 12. Pole figure for Ti-20Y as-cast ($\eta = 0$) on the Ti ($11\bar{2}0$) plane. Note that all relative intensity levels are near unity, as is typical of a specimen with little texture

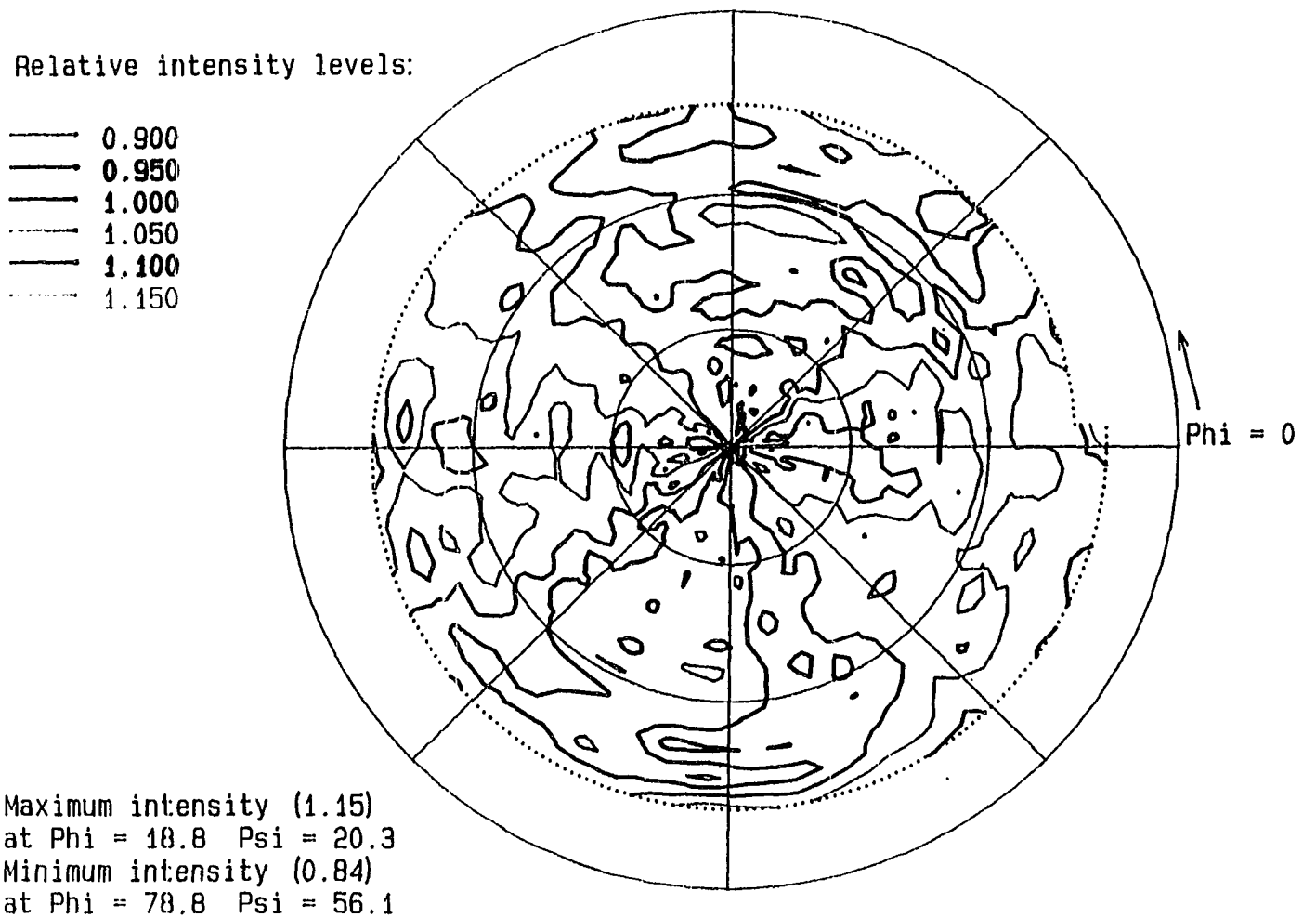

Figure 13. Pole figure for Ti-20Y as-cast ($\eta = 0$) on the Y $(01\bar{1}1)$ plane. Note that all relative intensity levels are near unity, as is typical of a specimen with little texture

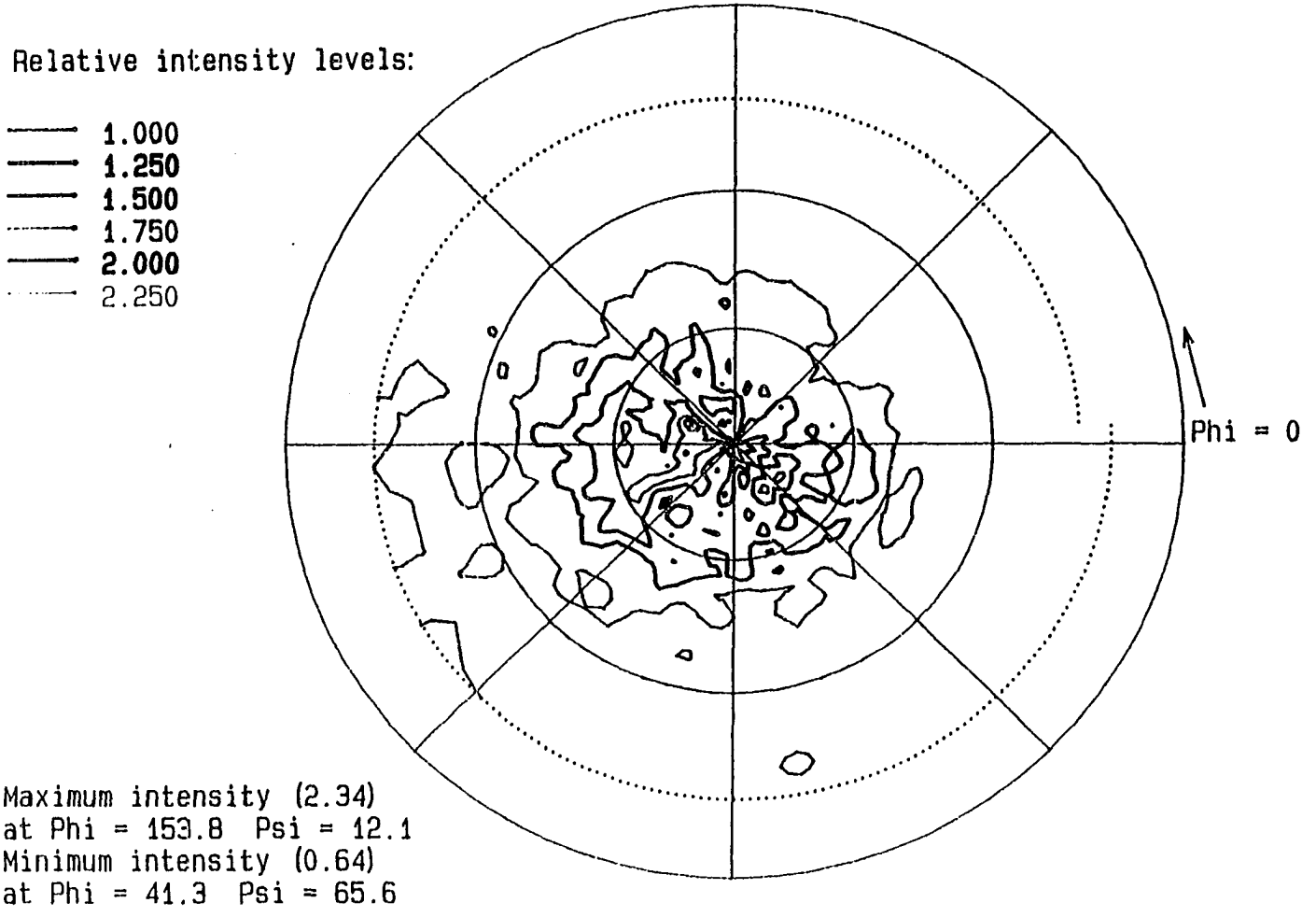

Figure 14. Pole figure for pure Ti as-extruded ($\eta = 2.25$) taken with x-rays diffracted from the $(01\bar{1}0)$ plane. An "ideally textured" Ti rod with a $<10\bar{1}0>$ fiber texture would display a central spot of high intensity and a ring at psi = 60° of moderate intensity. This pole figure shows clear evidence of the central spot but lacks a distinct ring at psi = 60°

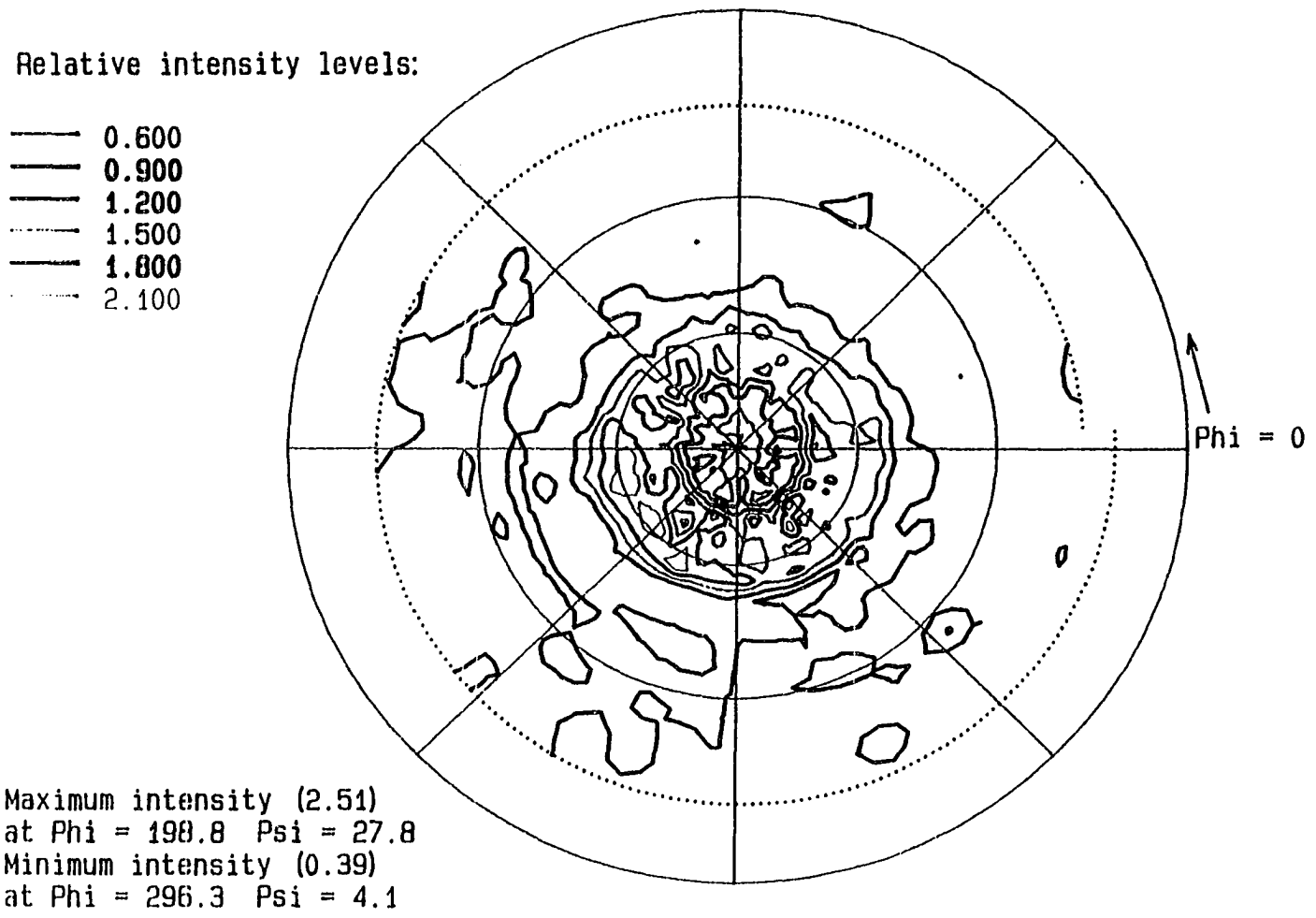

Figure 15. Pole figure for pure Ti as-extruded ($\eta = 2.25$) on the $(10\bar{1}1)$ plane. An "ideally textured" Ti rod with a $<10\bar{1}0>$ fiber texture would display a ring of moderate intensity at psi = 29°and a second ring at psi = 64° of lesser intensity. This pole figure shows clear evidence of the 29° ring but lacks a distinct ring at psi = 64°

The expected pole figure pattern from a hexagonal close packed metal with a $<10\bar{1}0>$ fiber texture can be predicted by applying simple vector calculations to the possible crystal positions within such a textured rod. Figure 16a depicts four individual hexagonal crystal cells aligned with their $<10\bar{1}0>$ direction parallel to the specimen's rod axis (centerline). (These four crystals represent the large number of such unit cells within an actual textured specimen.) It is relatively easy to visualize the possible pole figure (Figure 16b) that would result from a transversely sectioned $<10\bar{1}0>$ fiber textured specimen's $(10\bar{1}0)$ plane diffraction, since the $\{10\bar{1}0\}$ are the first order prism planes shown as the six rectangular surfaces on the sides of each hexagonal cell. Given the rotational freedom each crystal has (depicted in Figure 16a by the various positions of the four hexagonal crystals about the rod axis), one would expect to see a strong central spot from the two $(10\bar{1}0)$ planes lying parallel to the rod end, and one would also see a ring 60° distant (60° psi on the stereographic projection) from the central spot caused by diffraction from the four $(10\bar{1}0)$ planes in each crystal tilted 60° from the rod end. The pole figure is essentially the trace resulting from rotating the unit cell shown in Figure 16c about its vertical axis (i.e. the rod centerline). The ring would, of course, be of lesser intensity than the central spot since it results from the accumulated diffractions of thousands of grains within the sample, each of which is at a different angular position around the rod axis. Since these diffractions are spread over the 60° ring rather than focused on one spot, the relative intensity of the ring is lower on the x-ray pole figure.

A second easily visualized example for predicting the pole figure from a hexagonal close packed specimen with the $<10\bar{1}0>$ fiber texture is the (0002) basal plane pole figure. The (0002) plane is the hexagon at each end of the unit cells depicted in Figure 16a. Since all of these are perpendicular to the rod end, the pole figure for a transversely sectioned x-ray specimen will be a ring of intensity at 90° from the center of the stereographic projection. Since all data in this study were acquired at psi angles between 0°

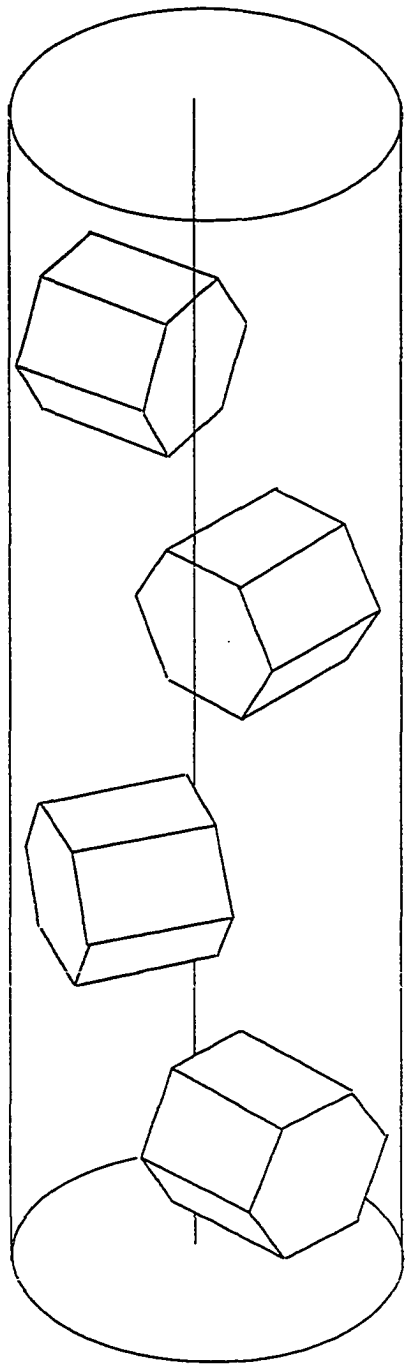

Figure 16a. Illustration of the $<10\bar{1}0>$ fiber texture in a hexagonal close packed rod. Each hexagonal prism depicts a unit cell with its $<10\bar{1}0>$ direction aligned along the rod axis

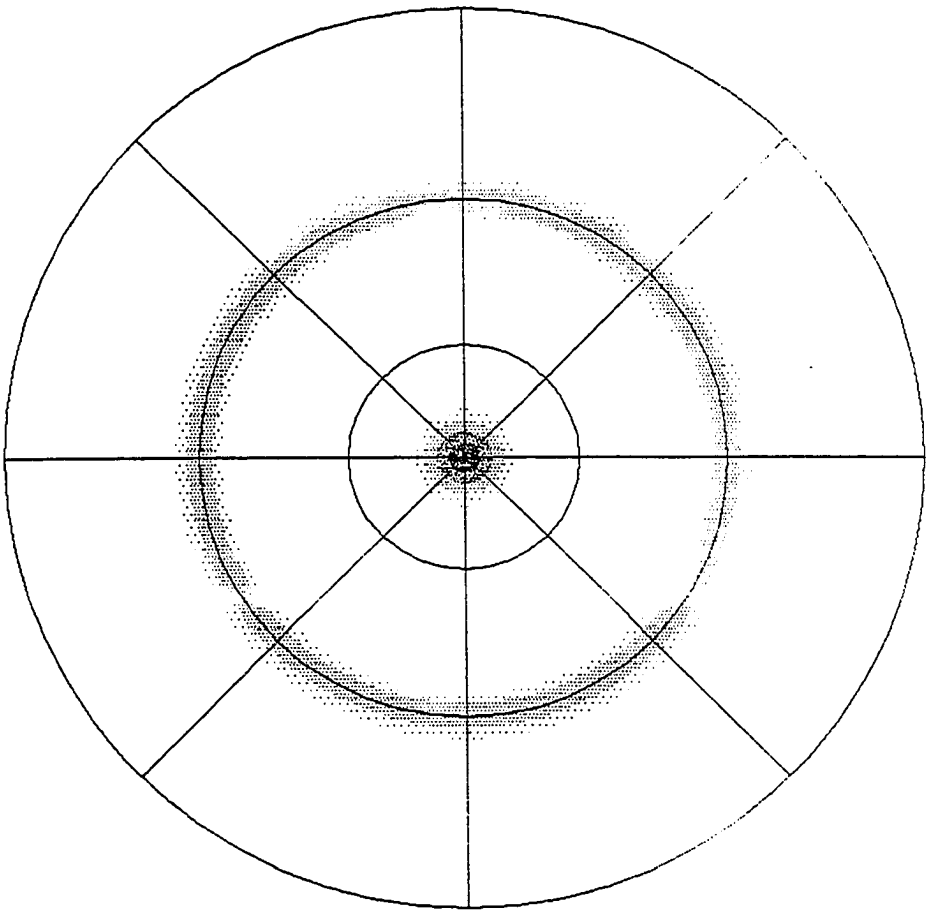

Figure 16b. Predicted pole figure for the $(01\bar{1}0)$ plane in any hcp lattice with a $<10\bar{1}0>$ fiber texture and approximately 5° to 10° dispersion from ideal texturing

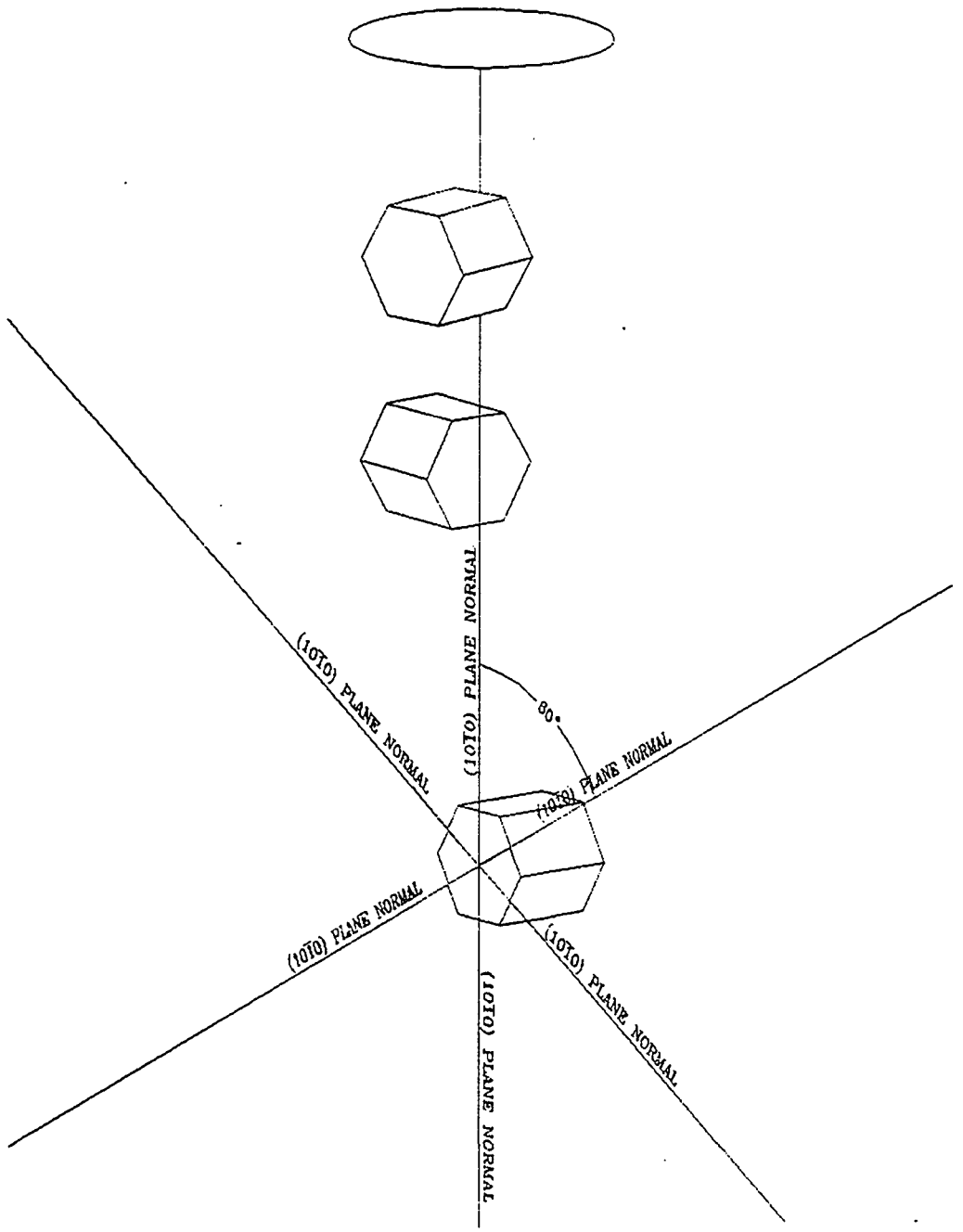

Figure 16c. This depiction is a modification of Figure 16a showing the plane normals to the $(01\bar{1}0)$ plane in any hcp lattice with a $<10\bar{1}0>$ fiber texture. The pole figure in Figure 16b results from rotating this hexagonal unit cell about its vertical axis (the rod specimen's centerline) and recording the trace of the plane normals on the stereographic hemisphere above the unit cell. The upper 3 normals produce the central spot and the ring in Figure 16b; the lower 3 normals are lost to the unrecorded hemisphere

and 80°, one would expect to see no intensity at all from the (0002) diffraction in a transverse section of an "ideally textured" specimen. (It should be noted that no specimen displays completely ideal texture; there is always some dispersion in the angles of the grains.)

Calculation of the predicted pole figures for other planes within the hexagonal close packed unit cell is somewhat more involved than the cases of the $(10\bar{1}0)$ and (0002) planes. For example, the $(11\bar{2}2)$ planes are second order pyramidal planes which lie at an angle to the basal planes (shown as the triangular plane segment OAC in Figure 17), and that angle varies with the c/a ratio of the particular hexagonal close packed cell. For Ti (and coincidentally for Y also), the c/a ratio is 1.587. To predict the pole figure for such a plane, it is useful to first calculate the vector normal to the $(11\bar{2}2)$ plane. This can be found from the cross product (vector product) of any two lines in that plane, such as:

$$\overline{AC} = -1.5i - .866j \text{ and } \overline{AO} = -i + \frac{1.587}{2}k$$

$$\overline{N}_{(11\bar{2}2)} = \overline{AC} \times \overline{AO} = \begin{vmatrix} i & j & k \\ -1.5 & -.866 & 0 \\ -1 & 0 & .7935 \end{vmatrix} = -.687i + 1.190j - .866k$$

The angle between the $<10\bar{1}0>$ direction and $\overline{N}_{(11\bar{2}2)}$ will then be:

$$\overline{N}_{(11\bar{2}2)} \bullet (-j) = |j| \left|\overline{N}_{(11\bar{2}2)}\right| \cos\varphi$$

$$-1.190 = 1.624 \cos\varphi$$

$$\varphi = 42.9°$$

Thus, one would expect a ring of intensity at angle psi = 42.9° from the center of the stereographic projection of the $(11\bar{2}2)$ pole figure for a specimen with a $<10\bar{1}0>$ fiber texture. Similar calculations were performed to predict the expected pole figures for the various planes of diffraction in Ti and Y discussed in this section.

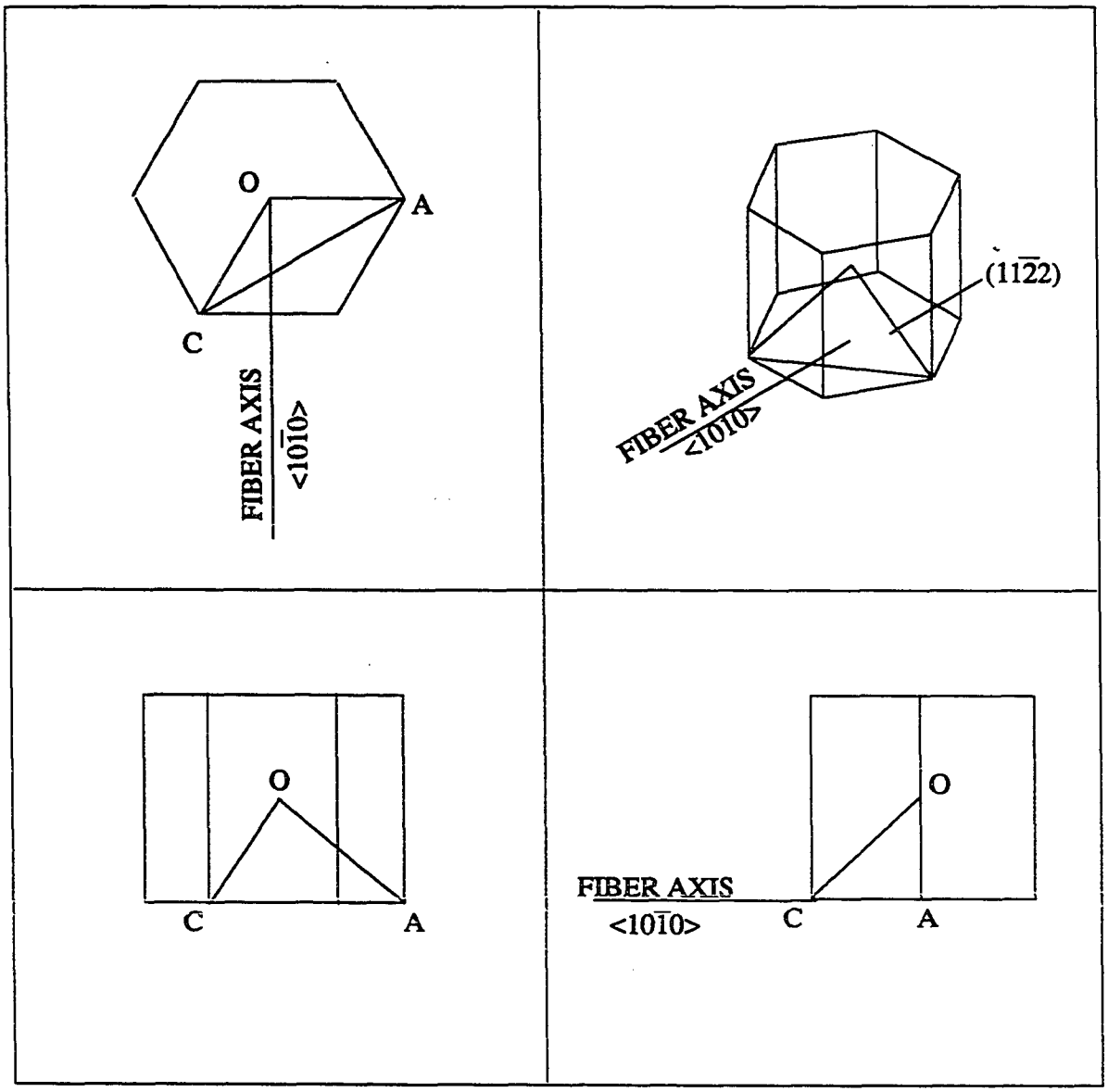

Figure 17. Top, front, right profile and isometric views of a hexagonal close packed unit cell with the $<10\bar{1}0>$ fiber axis direction and the $(11\bar{2}2)$ plane (OAC) marked

The x-ray pole figures show that the transversely sectioned specimen of as-extruded Ti-20Y ($\eta = 2.25$) is textured with the same $<10\bar{1}0>$ fiber texture seen in the pure Ti control specimen. However, the as-extruded Ti-20Y specimen is more highly textured than the as-extruded pure Ti specimen. Figures 18 and 19 show the same pole figure for the Ti $(10\bar{1}0)$ diffraction; Figure 18 shows six relative intensity contours, and Figure 19 shows 10 relative intensity contours. The ideal $<10\bar{1}0>$ fiber texture would show a strong central spot and a less intense ring at psi = 60°. The central spot is clearly evident in both figures, and a partial ring is visible in Figure 19. Both the central spot and the partial ring deviate slightly from the concentric symmetry one would expect from an axisymmetrically deformed specimen. This shift of roughly 3° to 5° may be caused by failure to cut the specimen on a plane perfectly perpendicular to the extrusion centerline. (Figure 7 depicts a perfectly perpendicular cut.) The as-extruded rods were not perfect cylinders; there was a slight "waviness" along the length of the rod that may have contributed to this shift. The relative intensities of this Ti $(10\bar{1}0)$ pole figure range from a minimum of 0.59 to a maximum of 7.02, which is roughly double the intensity range observed on the as-extruded pure Ti $(10\bar{1}0)$ pole figure.

Other pole figures from the as-extruded Ti-20Y x-ray specimen confirm the presence of the $<10\bar{1}0>$ fiber texture. The $(01\bar{1}1)$ Ti pole figure shown in Figure 20 would display a ring at psi = 29° and a second ring of lower intensity at psi = 64° for an ideal $<10\bar{1}0>$ fiber texture. With allowances for the slight deviation from concentricity discussed above, this is the pattern seen in Figure 20.

Although the Y is present as only 20% by volume in the Ti-20Y specimen, useful Y x-ray texture pole figures were measureable on the strongest Y peaks from the 2θ scans. In the case of as-extruded Ti-20Y, the Y $(10\bar{1}0)$ pole figure (Figure 21) shows clear evidence of the strong central spot and a portion of the 60° ring associated with $<10\bar{1}0>$ fiber texture in

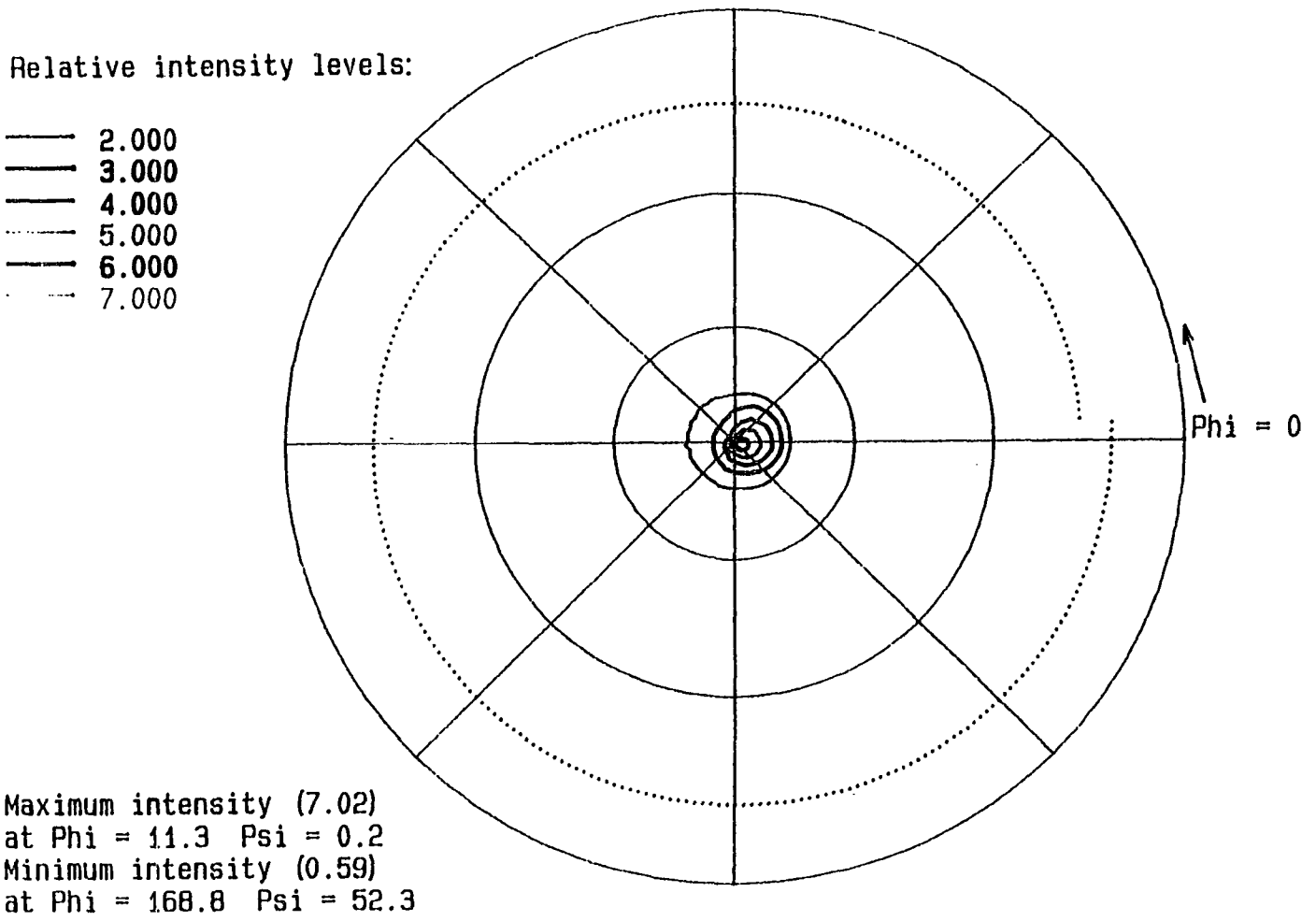

Figure 18. Ti $(10\bar{1}0)$ pole figure for as-extruded Ti-20Y ($\eta = 2.25$) plotted with five relative intensity contour levels. An ideally textured specimen with a $<10\bar{1}0>$ fiber texture would display a strong central spot and a less intense ring at psi = 60°

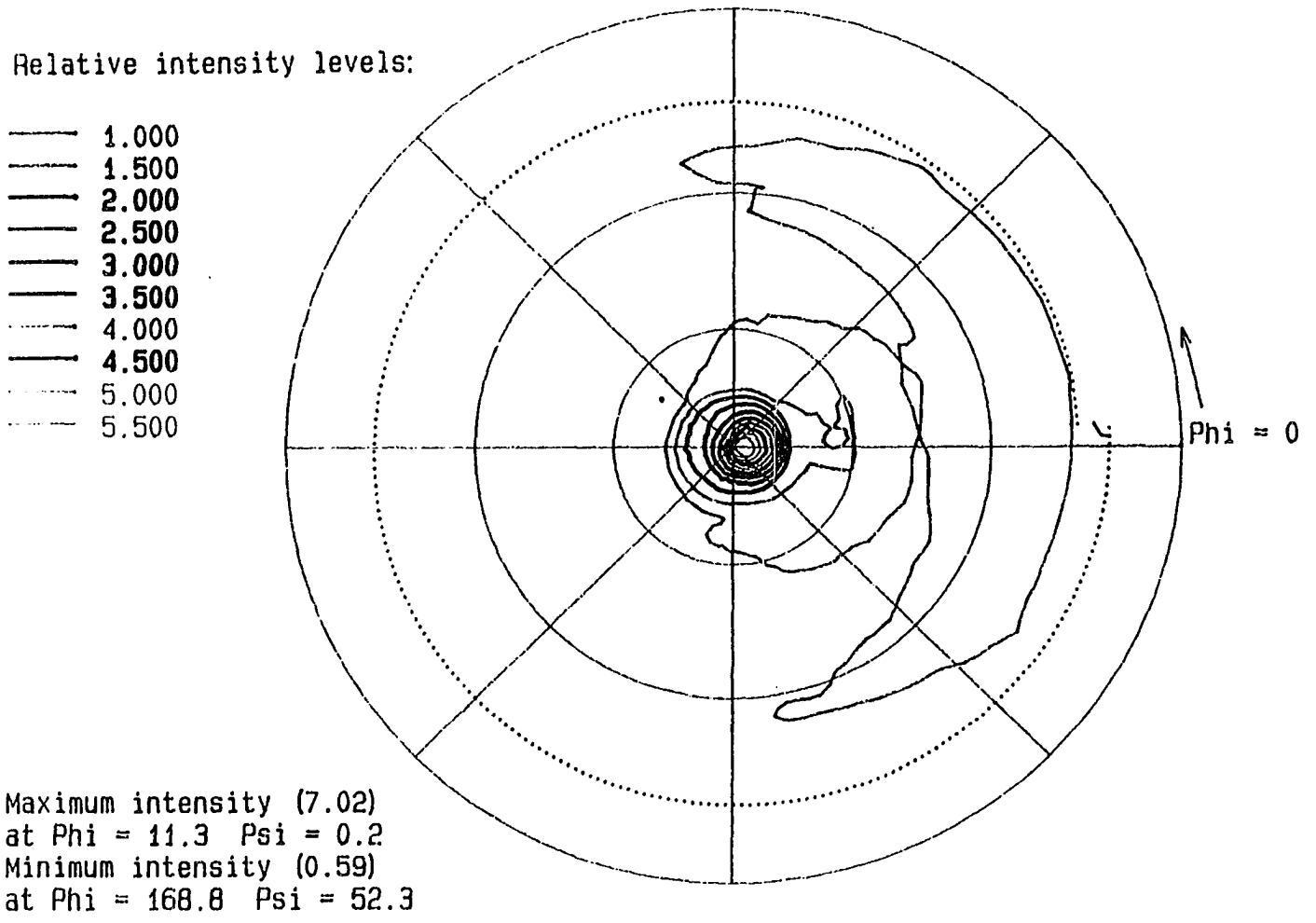

Figure 19. Ti $(10\bar{1}0)$ pole figure for as-extruded Ti-20Y ($\eta = 2.25$) plotted with 10 relative intensity contour levels. An ideally textured specimen with a $<10\bar{1}0>$ fiber texture would display a strong central spot and a less intense ring at psi = 60°

the Y filaments. Although a literature search found no texturing studies for axisymmetrically deformed Y, it seems reasonable to assume that Y with the same hexagonal close packed structure and the same c/a ratio as Ti would develop the $<10\bar{1}0>$ fiber texture so well documented for pure Ti. The $<10\bar{1}0>$ fiber texture is also seen in drawn Be, Zr, and Hf [29], all of which are hexagonal close packed metals with c/a ratios close to the Y and Ti c/a ratio.

Several factors could have caused the specimens to assume textures other than the $<10\bar{1}0>$ fiber texture actually observed in both Ti and Y. When pure Ti recrystallizes after wire drawing, a $<11\bar{2}0>$ fiber texture typically replaces the $<10\bar{1}0>$ fiber texture. The recrystallization texture of Y is unknown. Moreover, the plane strain deformation mode of both the Ti and Y phases during deformation processing could have introduced unexpected textures different from those seen in pure, single-phase Ti. In addition, the unusually high levels of true strain employed in this experiment are substantially higher than the strains often used to determine the "handbook values" of deformation-induced textures.

The pure Ti transverse sectioned x-ray specimens taken from material deformation processed to $\eta = 5.03$ shows the same $<10\bar{1}0>$ fiber texture as the as-extruded ($\eta = 2.25$) pure Ti but the relative intensities are greater. Figure 22 shows the $(10\bar{1}0)$ pole figure for pure Ti deformation processed to $\eta = 5.03$. The expected $<10\bar{1}0>$ fiber texture central spot and weaker ring at psi = 60° are clearly evident, and the relative intensity range of 0.68 to 4.58 suggests a more highly textured structure than was seen in Figure 14 (intensity range of 0.64 to 2.34) for the as-extruded pure Ti. Figure 23 shows the $(11\bar{2}0)$ pole figure for the pure Ti specimen deformation processed to $\eta = 5.03$. The expected $(11\bar{2}0)$ pole figure for an ideal $<10\bar{1}0>$ fiber texture would be a ring at psi = 30°, which closely matches the pattern observed in Figure 23.

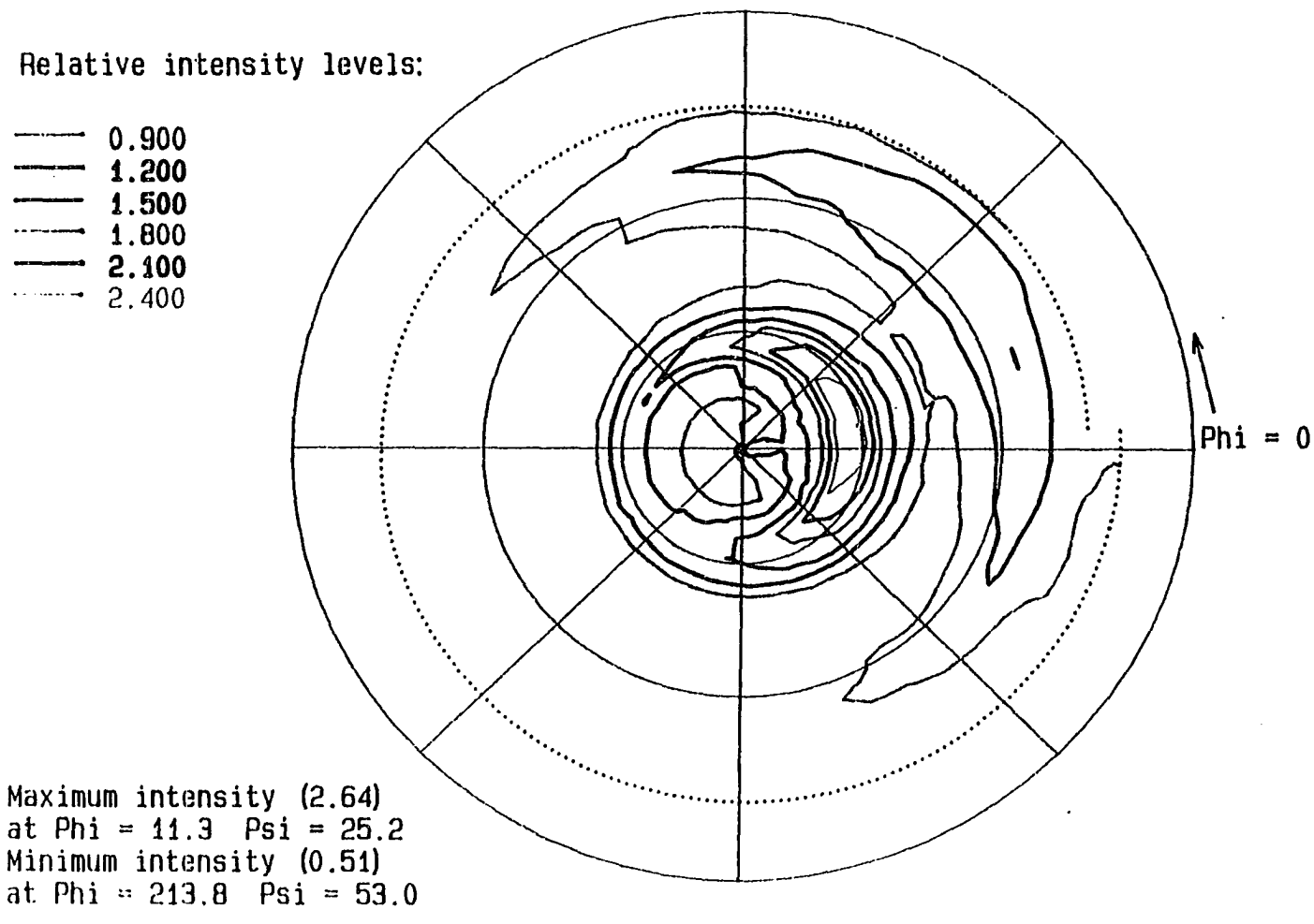

Figure 20. Ti (01$\bar{1}$1) pole figure for as-extruded Ti-20Y (η = 2.25). An ideally textured specimen with a $<10\bar{1}0>$ fiber texture would display a ring at psi = 29° and a less intense ring at psi = 64°

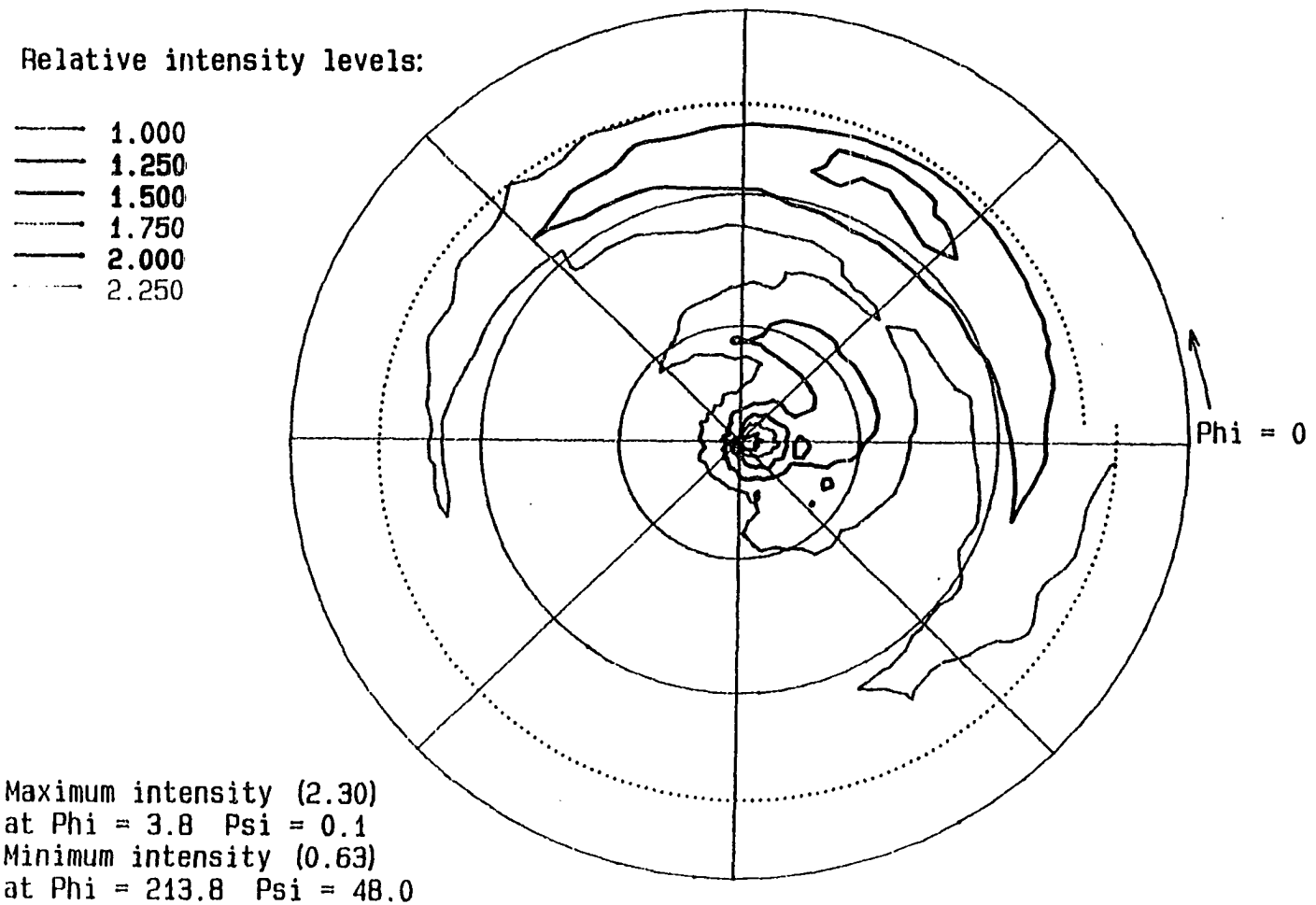

Figure 21. Y $(10\bar{1}0)$ pole figure for as-extruded Ti-20Y ($\eta = 2.25$). An ideally textured specimen with a $<10\bar{1}0>$ fiber texture would display a strong central spot and a less intense ring at psi = 60°

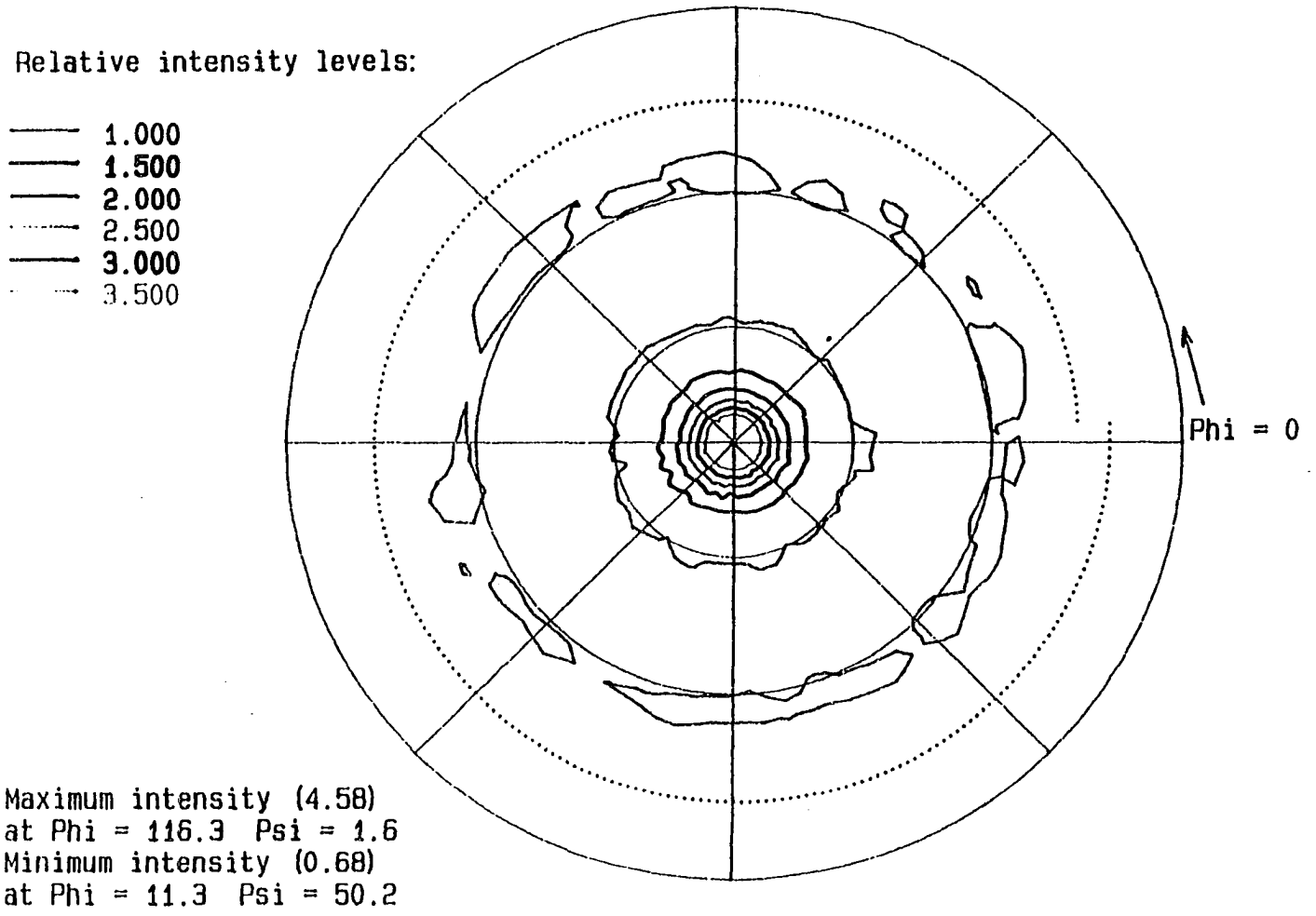

Figure 22. Pole figure for pure Ti deformation processed to $\eta = 5.03$ taken with x-rays diffracted from the $(01\bar{1}0)$ plane. An "ideally textured" Ti rod with a $<10\bar{1}0>$ fiber texture would display a central spot of high intensity and a ring at psi = 60° of moderate intensity

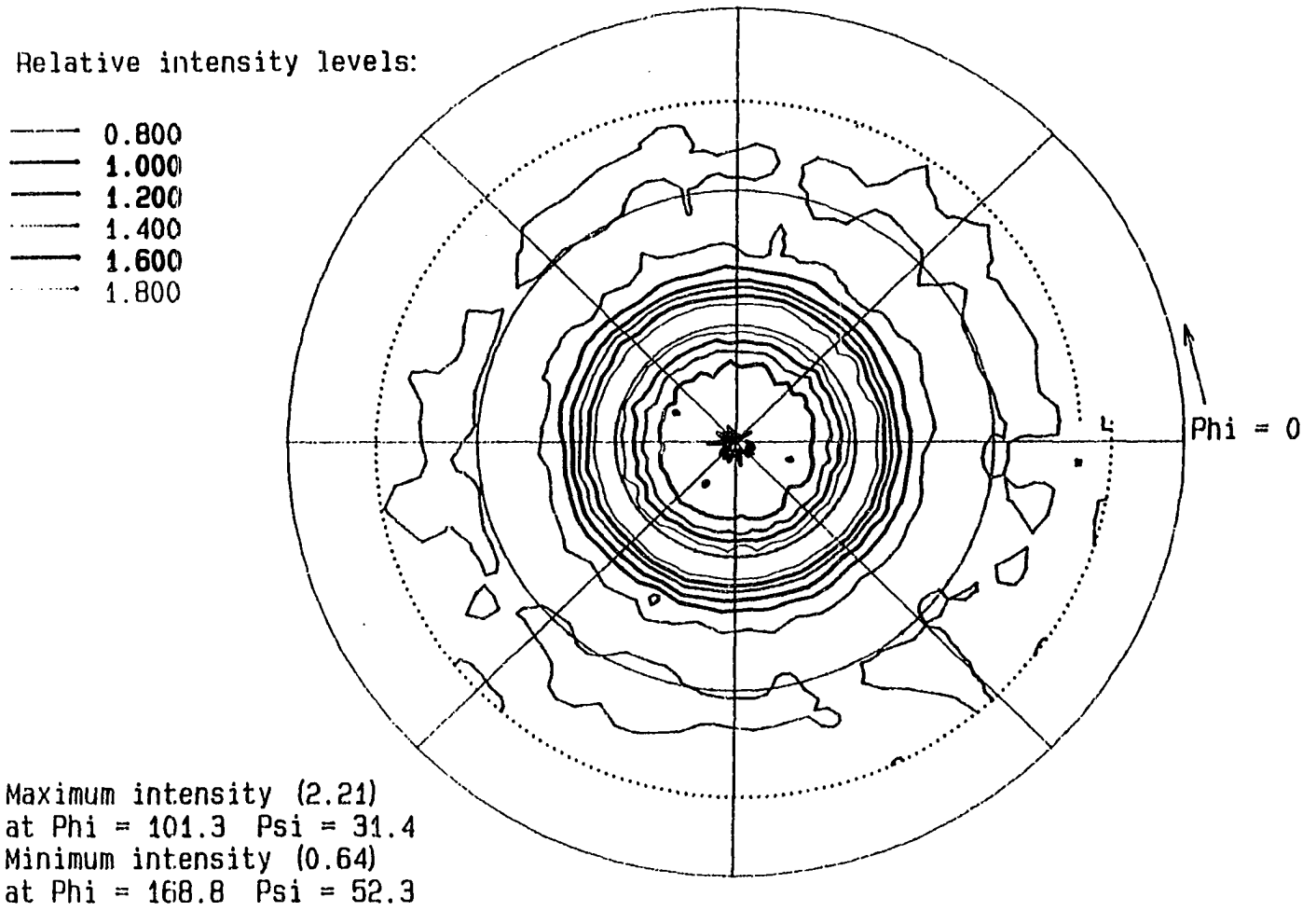

Figure 23. Pole figure for pure Ti deformation processed to $\eta = 5.03$ taken with x-rays diffracted from the $(11\bar{2}0)$ plane. An ideal $<10\bar{1}0>$ fiber texture would display a ring at psi = 30° on this pole figure

Pole figures for the Ti-20Y specimen deformation processed to $\eta = 5.03$ show the same $<10\bar{1}0>$ fiber texture for both the Ti and the Y phases. Figure 24 shows the $(01\bar{1}0)$ pole figure for transversely sectioned Ti-20Y at $\eta = 5.03$. The pattern and intensity levels are similar to those of Figure 19 for Ti-20Y at $\eta = 2.25$. Both the central spot and the ring at psi = 60° are clearly defined. The degree of texturing seems little changed between the two deformation processing levels ($\eta = 2.25$ and 5.03). Other Ti pole figures for the Ti-20Y specimen deformation processed to $\eta = 5.03$ are shown in Figures 25-27 for some of the higher index planes. The Y $(01\bar{1}0)$ pole figure for this Ti-20Y specimen deformation processed to $\eta = 5.03$ is presented in Figure 28.

The collection of pole figures for both the pure Ti control specimen and the Ti-20Y composite show that the inital castings were essentially without texture and that a $<10\bar{1}0>$ fiber texture developed in both the Ti and Y phases upon extrusion at 800° C. to $\eta = 2.25$ and was maintained during room temperature deformation processing to $\eta = 5.03$. This finding is consistent with the well documented existence of the $<10\bar{1}0>$ fiber texture in axisymmetrically deformed Ti.

In a study of deformation mechanisims active in Ti, Anderson, Jillson, and Dunbar [40] found that two slip systems are active in pure Ti. The critical resolved shear stress (CRSS) for slip in the $<11\bar{2}0>$ direction on the (0002) basal plane (illustrated in Figure 29) was found to be 110 MPa, and the CRSS for slip in the $<11\bar{2}0>$ direction on the $\{10\bar{1}0\}$ first order prism planes (illustrated in Figure 30) was found to be 50 MPa.

In a study of deformation mechanisims active in Ti, Anderson, Jillson, and Dunbar [40] found that two slip systems are active in pure Ti. The critical resolved shear stress (CRSS) for slip in the $<11\bar{2}0>$ direction on the (0002) basal plane (illustrated in Figure 29) was found to be 110 MPa, and the CRSS for slip in the $<11\bar{2}0>$ direction on the $\{10\bar{1}0\}$ first order prism planes (illustrated in Figure 30) was found to be 50 MPa.

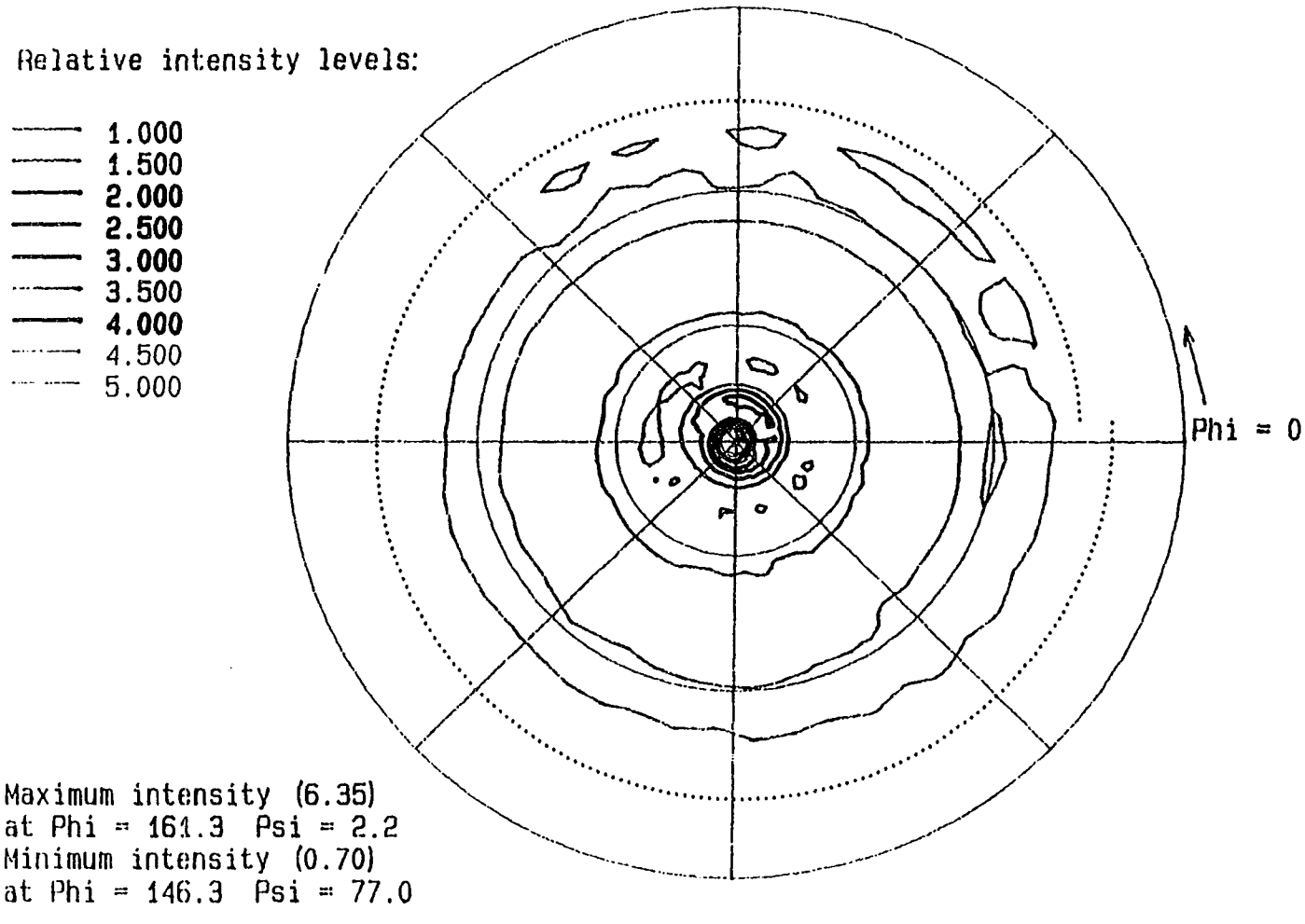

Figure 24. Ti $(10\bar{1}0)$ pole figure for Ti-20Y (η = 5.03). An ideally textured specimen with a $< 10\bar{1}0 >$ fiber texture would display a strong central spot and a less intense ring at psi = 60°

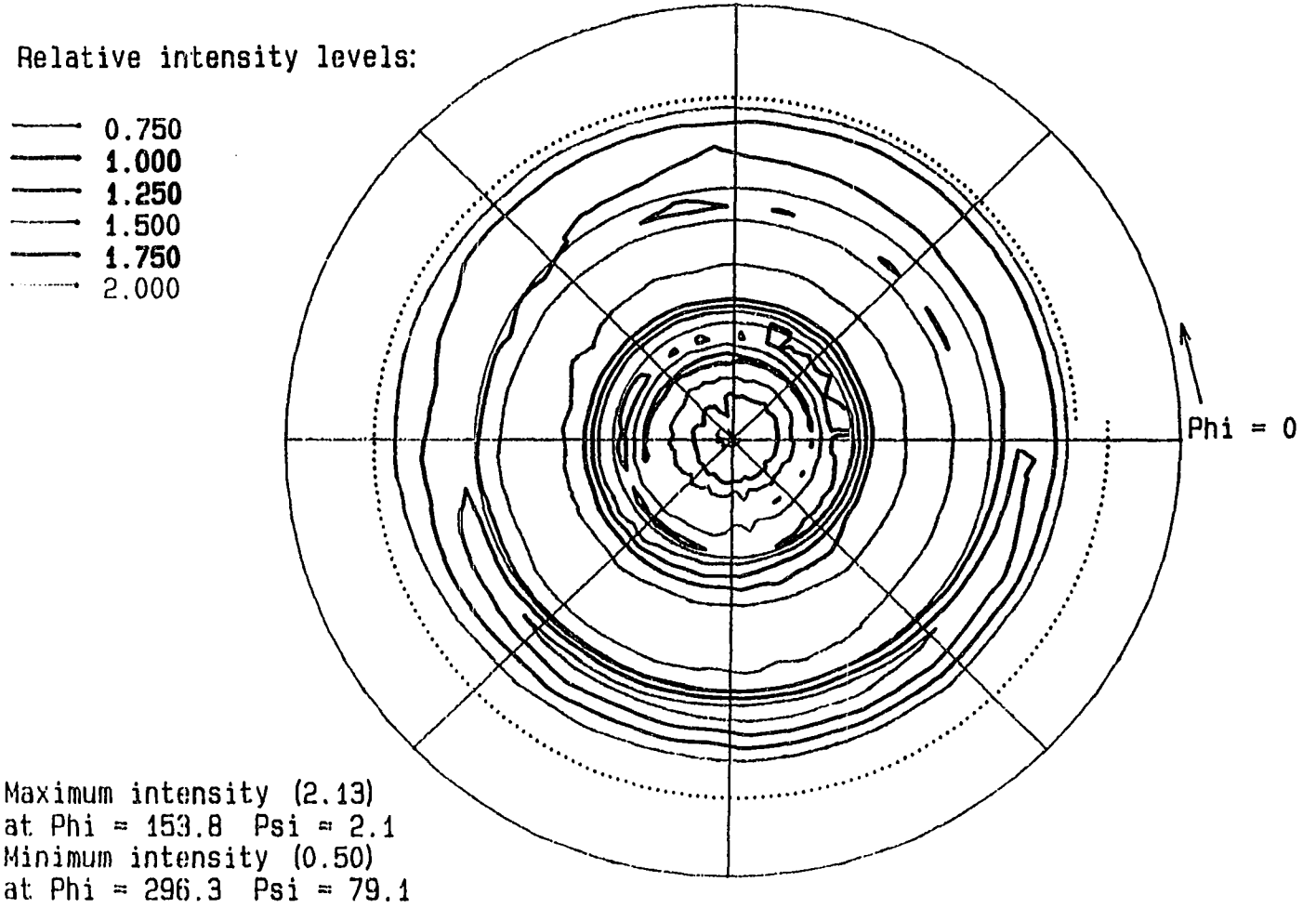

Figure 25. Ti (01$\bar{1}$1) pole figure for Ti-20Y (η = 5.03). An ideally textured specimen with a $<10\bar{1}0>$ fiber texture would display a ring at psi = 29° and a second, weaker ring at psi = 64°

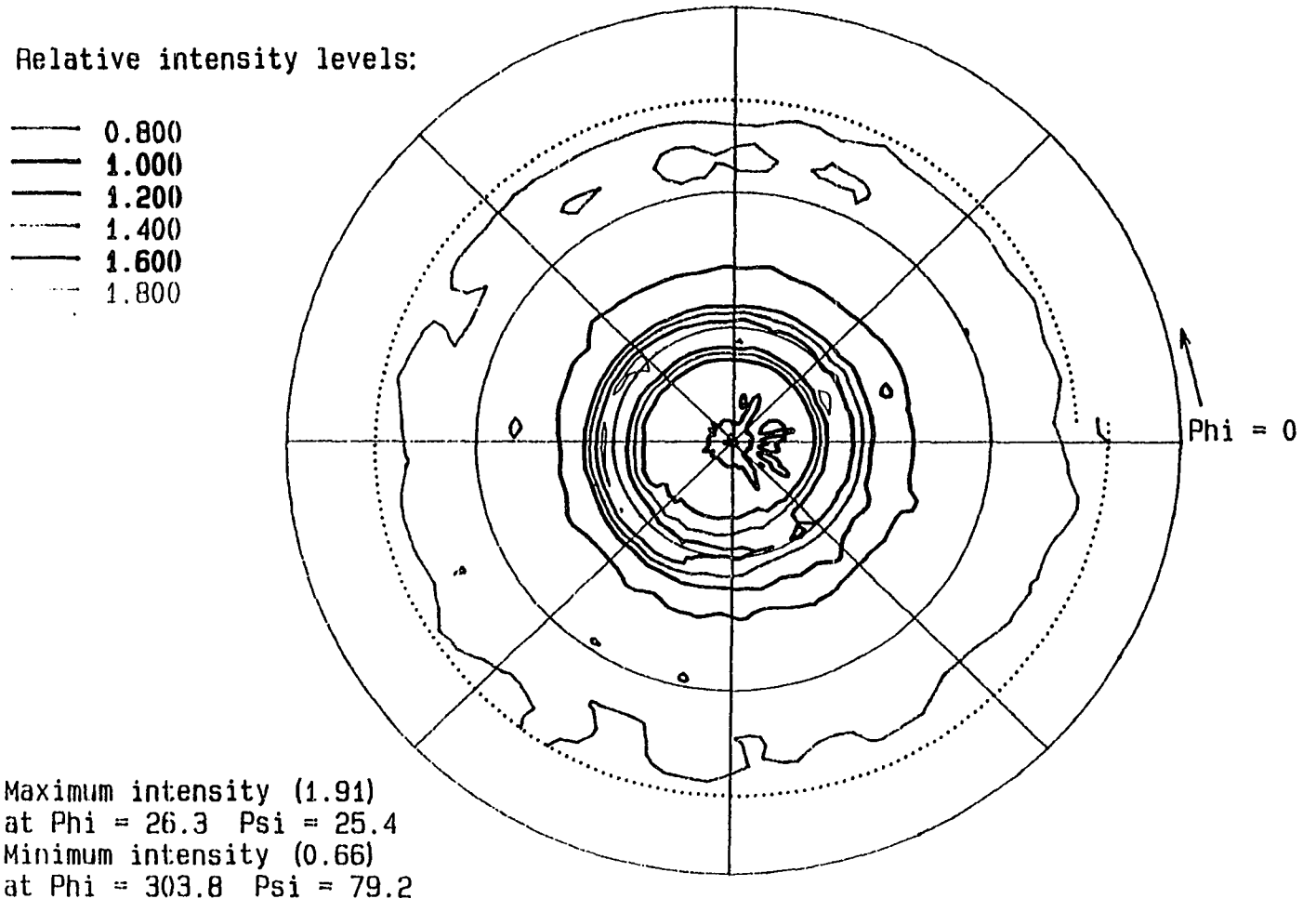

Figure 26. Ti $(11\bar{2}0)$ pole figure for Ti-20Y ($\eta = 5.03$). An ideally textured specimen with a $<10\bar{1}0>$ fiber texture would display a ring at psi = 30°

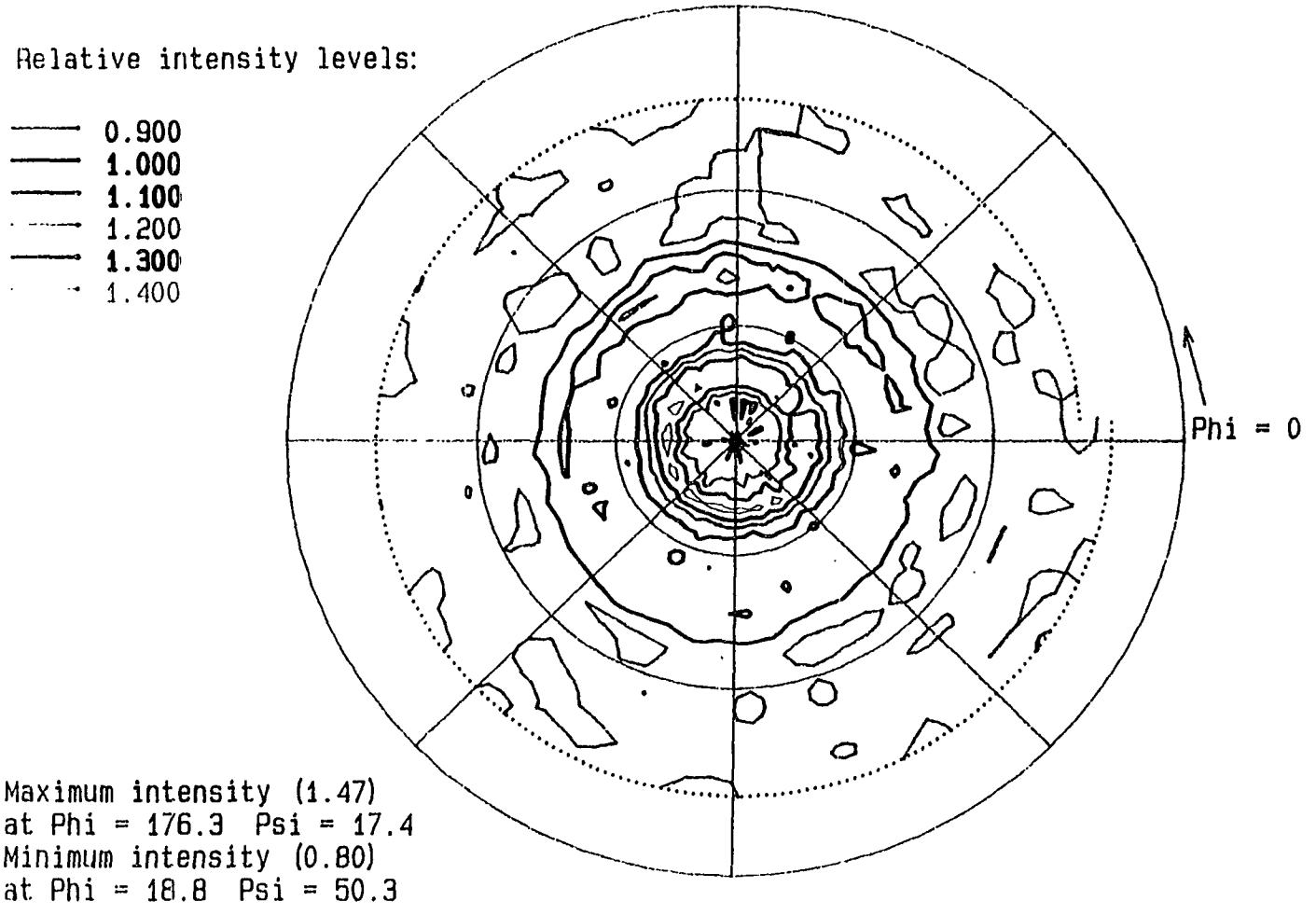

Figure 27. Ti (12$\bar{3}$1) pole figure for Ti-20Y (η = 5.03). An ideally textured specimen with a <10$\bar{1}$0> fiber texture would display a ring at psi = 22° and a second, weaker ring at psi = 42°

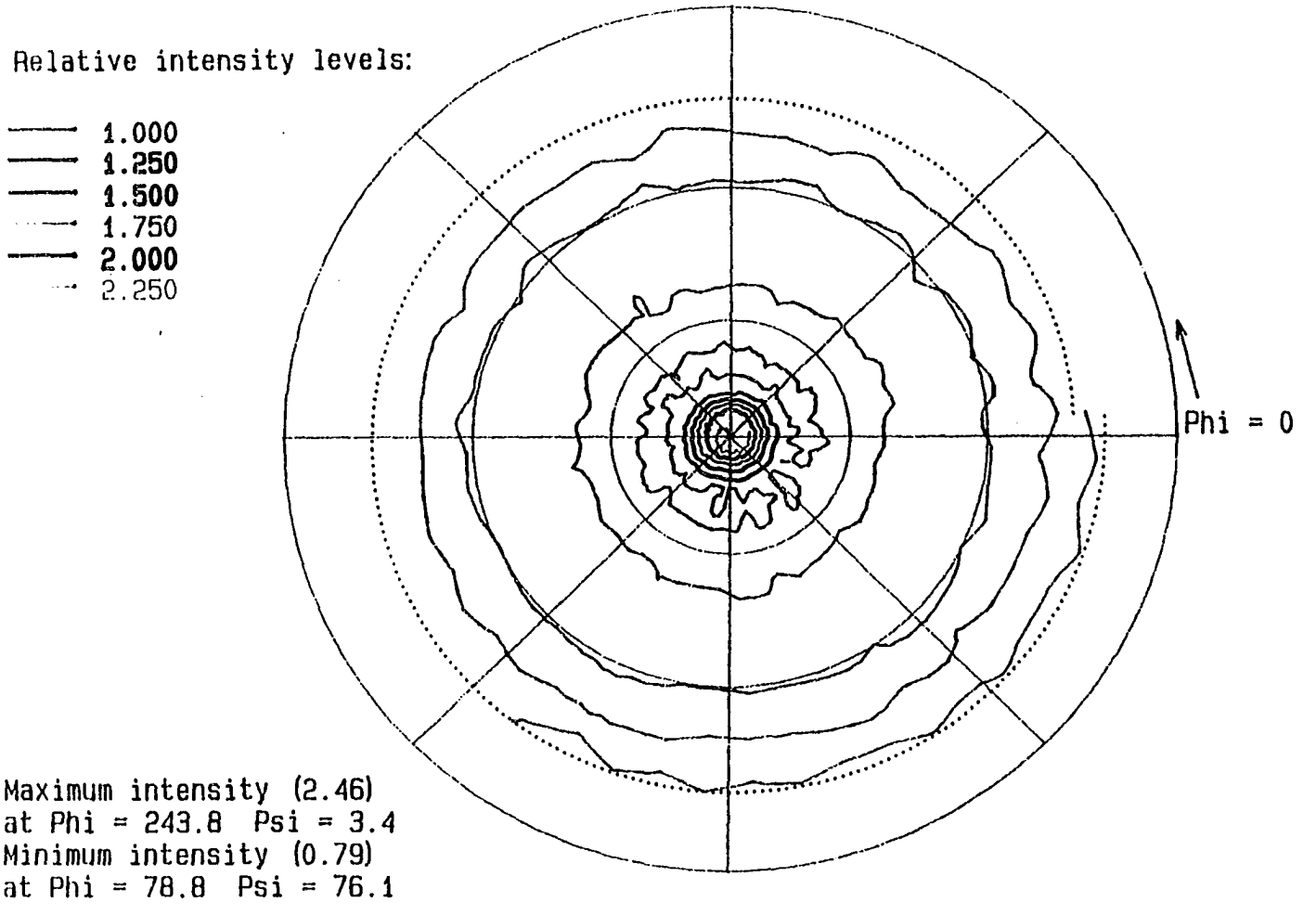

Figure 28. Y $(10\bar{1}0)$ pole figure for Ti-20Y ($\eta = 5.03$). An ideally textured specimen with a $<10\bar{1}0>$ fiber texture would display a strong central spot and a less intense ring at psi = 60°

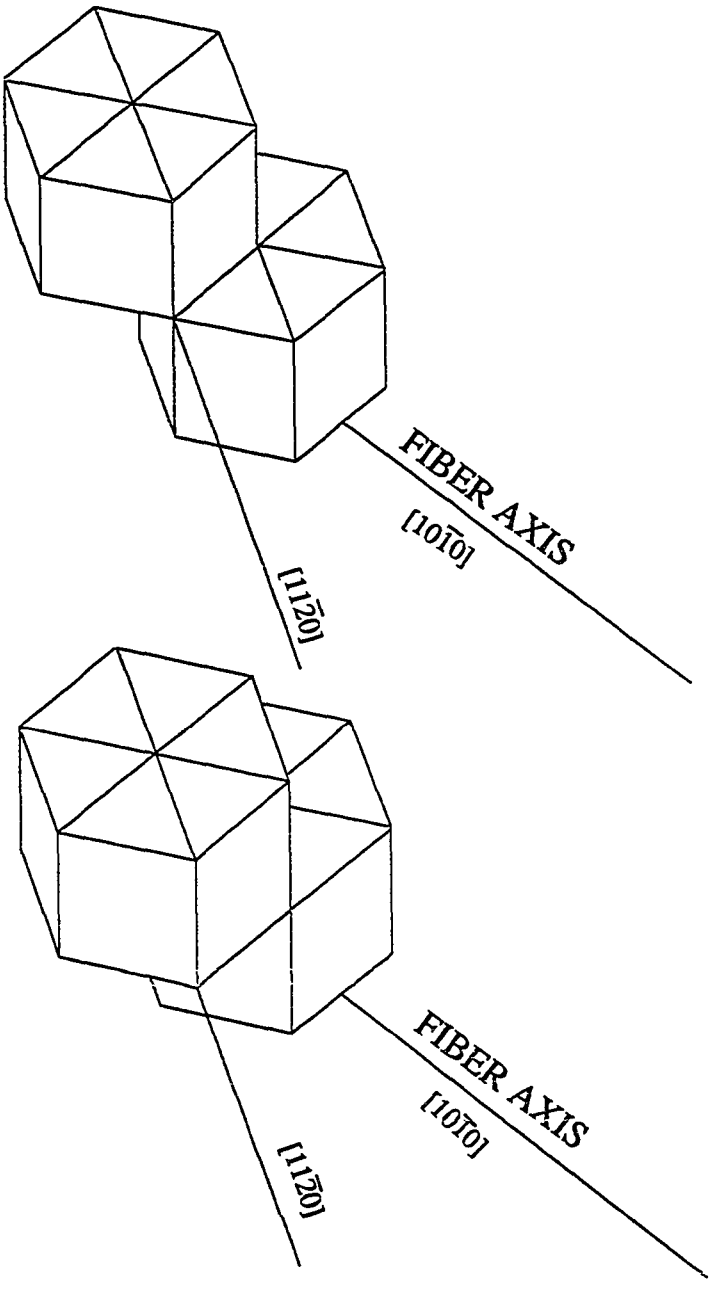

Figure 29. Illustration of the relative orientations of two hexagonal close packed unit cells with a $<10\bar{1}0>$ fiber texture before and after a slip of one Burger's vector magnitude on the (0002) $<11\bar{2}0>$ slip system. This slip system actually has a resolved shear stress of zero in this orientation, and thus would be inactive in $<10\bar{1}0>$ fiber textured metal

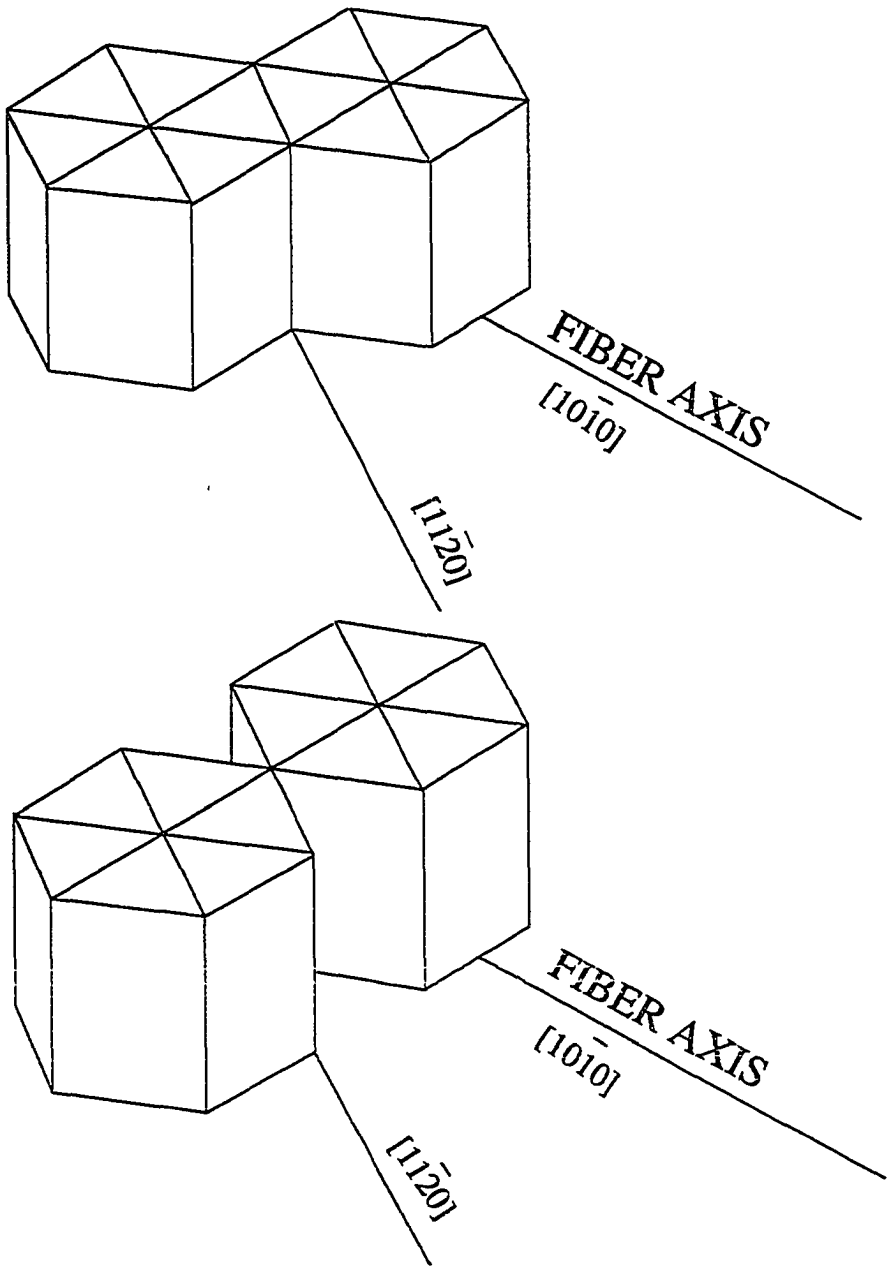

Figure 30. Illustration of the relative orientations of two hexagonal close packed unit cells with a $<10\bar{1}0>$ fiber texture before and after a slip of one Burger's vector magnitude on the $\{10\bar{1}0\}\ <11\bar{2}0>$ slip system

The CRSS in the Ti basal plane is unusually high compared to the basal plane CRSS of other hexagonal close packed metals such as Zn (0.18 MPa), Cd (0.57 MPa), or Mg (0.43 MPa). Reed-Hill and Abbaschian [41] comment that this large difference in basal plane CRSS values is apparently related to the c/a ratio. In metals with a low CRSS for basal slip, such as Zn, Cd, and Mg, the c/a ratios are high (Zn: 1.856, Cd: 1.886, and Mg: 1.624). Ti has a c/a ratio of 1.587 which is less than the 1.632 c/a ratio that would be seen if the atoms were perfect spheres in a hexagonal close packed lattice. Be and Zr also have low c/a ratios; in Be the basal plane CRSS is high (39 MPa), and basal slip has never been observed in Zr. Since the basal planes of Ti (and also of Y, which has the same c/a ratio as Ti) are closer together than would be seen in the perfect sphere model, basal slip is thought to require more energy than basal slip in lattices with a high c/a ratio where the basal planes are more widely spaced. By comparison, CRSS values for the {111} closest-packed planes in high-purity fcc metals are typically low; the CRSS value for the {111}<110> slip system is 0.37 MPa in Ag, 0.63 MPa in Cu, 0.91 MPa in Au, and 1.02 MPa in Al.

With a CRSS of 110 MPa in the (0002) $<11\bar{2}0>$ slip system in Ti, it is not surprising that Ti textures to optimize slip on the $\{10\bar{1}0\}$ $<11\bar{2}0>$ slip system, where the CRSS is lower at 50 MPa. It seems likely that Y, with the same low c/a ratio as Ti, behaves similarly. With the $<10\bar{1}0>$ fiber texture observed for both Ti and Y in this experiment, applying Schmid's Law to calculate the shear stress for basal plane slip yields:

$$\tau_r = \sigma \cos\phi \cos\lambda = 0$$

where τ_r = the resolved shear stress on the given slip system, σ = the stress on the rod (force/cross section area), λ= the angle between the rod axis and the slip direction (30° or 90°), and ϕ = the angle between the rod axis and the normal to the slip plane (90°). Thus, basal slip would not occur in a $<10\bar{1}0>$ fiber textured rod.

If Schmid's Law is applied to the $\{10\bar{1}0\}<11\bar{2}0>$ slip system in a rod with the $<10\bar{1}0>$ fiber texture, λ becomes 30° and ϕ becomes 60°, which yields a resolved shear stress of:

$$\tau_r = \sigma\cos\phi\cos\lambda = \sigma\cos(60°)\cos(30°) = 0.433\sigma$$

A resolved shear stress of 0.433σ is near the maximum possible value of 0.5σ, and this slip system must be the active one in axisymmetrically deformed specimens with the $<10\bar{1}0>$ fiber texture.

There is a striking similarity between the arrangement of available slip systems in a hexagonal close packed lattice with the $<10\bar{1}0>$ fiber texture and the body-centered cubic lattice with the <110> fiber texture. As illustrated in Figures 4 and 31, both situations limit slip to two directions that are opposite one another across the rod center line (as compared with the three or four slip directions possible in a fcc lattice), and both would be expected to result in plane strain of each individual phase within the composite specimen. Thus, this analysis would predict that a deformation processed composite comprised of hexagonal close packed metals would undergo the same filament shaping processes that have been observed in the bcc filaments of Cu-X composites. Since both the Ti and the Y are limited to plane strain in the $<10\bar{1}0>$ fiber texture orientation, the twisted ribbon shape so frequently seen in the bcc filaments of Cu-X composites would be expected for <u>both</u> phases in the Ti-Y composite. The very thin filaments with exceptionally large interfacial boundary area inherent in such phase morphology might in turn produce the anomalous strengthening observed with the fcc/bcc Cu-X composites but absent in the fcc/fcc composites such as Ag-Cu. [3]

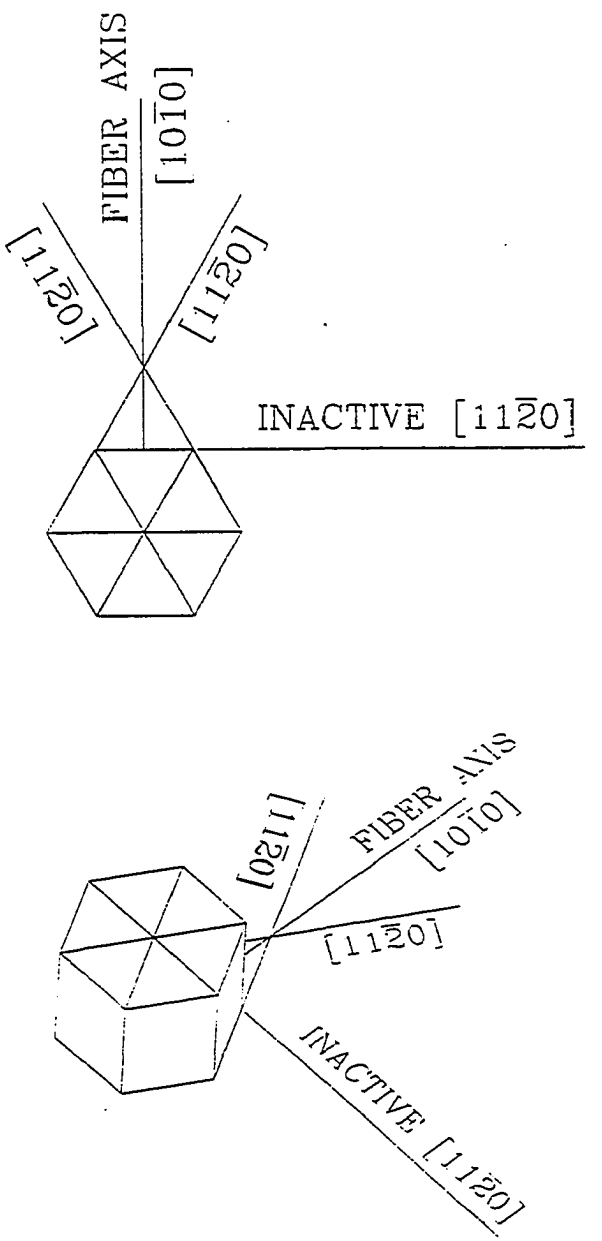

Figure 31. Depiction of the two available positions of the $\{10\bar{1}0\}<11\bar{2}0>$ slip system in Ti and Y textured with a $<10\bar{1}0>$ fiber texture. The top illustration is shown in plan view; the bottom illustration is the same configuration oriented pictorially. Note that the two active $<11\bar{2}0>$ slip directions are opposite from one another across the fiber axis, which constrains the crystal to deform by plane strain only. The third $<11\bar{2}0>$ slip direction is orthogonal to the fiber axis and is therefore inactive

Phase Spacing Measurements and Phase Morphology Observations

Optical microscope photographs and SEM and TEM photographs were measured to determine the average phase thicknesses presented in Table 3 for both the Ti and Y phases of the composite Ti-20Y and to measure the average grain diameter of the pure Ti control specimen. These micrographs also provided information on the phase morphology of the specimens at various levels of deformation processing.

Table 3. Average phase thicknesses measured by optical microscopy, SEM, and TEM for the Ti control and Ti-20Y

True Strain (η)	Pure Ti Average Grain Diameter (μm)	Ti-20Y Average Ti Phase Thickness (μm)	Ti-20Y Average Y Phase Thickness (μm)	Ti-20Y Average Phase Thickness (μm)
0	760	9.6	2.4	
2.25	65	3.8	0.96	
5.03	70	0.69	0.17	
7.27		0.16	0.041	
12.2				0.23
12.8				0.20

In the pure Ti control specimen, the as-cast ($\eta = 0$) specimen showed large, equiaxed grains of average diameter 760 μm. Since the grains in the pure Ti specimens at $\eta = 0$, 2.25, and 5.03 were all approximately equi-axed and showed no evidence of elongation from their extensive axisymmetric deformation, it appears the coarse grains in the as-cast pure Ti ($\eta = 0$) recrystallized during extrusion, and the recrystallized grains then assumed the $<10\bar{1}0>$

fiber texture shown in x-ray texture analysis at η = 2.25 and 5.03. The Ti control specimen average grain size was 65 μm after extrusion (η = 2.25) and 70 μm at η = 5.03.

The as-cast (η = 0) Ti-20Y composite showed the dendritic structure (see Figure 32) typical of two co-melted immiscible metals. Extrusion (η = 2.25) changed the Ti-20Y phase structure to elongated filaments of Y and Ti (see Figures 33-34), and subsequent deformation processing through η = 7.27 greatly reduced the thickness and spacing of these filaments, as shown in Figures 35-36. It is particularly significant that the Y filaments and Ti matrix display the convoluted ribbon shape predicted by the plane strain texture-slip system analysis described in the preceding section.

At deformation processing true strains greater than η = 7.27, the convoluted ribbon phase morphology was replaced by a simple equiaxed grain structure (Figures 37-38). Although this microstructure had a small average grain size (200 to 230nm), the change in the shape of both the Ti and Y grains indicates that the plate-like filaments of Ti and Y were changed to shapes nearer those of cylinders and/or spheres. The driving force for such change is the reduction in surface energy associated with reducing the interphase surface area within the sample and by increasing the radii of curvature of these boundaries, as described by Malzahn, Kampe, and Courtney [42-43] during the 700° C recovery anneals used in the wire drawing process at G & S Titanium. This process occurs more readily at high η levels since the filament edge radii become exceedingly small for filaments smaller than about 50 to 100nm, and the Gibbs-Thomson force for coarsening associated with interfacial surface energy becomes large as the total interfacial area increases at high η values. The selection of 700° C for the annealing temperature was based upon handbook values for pure Ti recovery and recrystallization, hot-stage TEM studies conducted on Ti-50Y specimens deformation processed to η = 4.8, and upon experience with earlier specimens of Ti-20Y and Ti-50Y deformation processed to η = 7.6. None of these sources of information was entirely

appropriate to a Ti-20Y composite deformation processed beyond $\eta = 7.6$, and it appears the filamentary structure was unstable to spheroidization at 700° C.

As noted earlier, x-ray texture specimens were not prepared at η values greater than 5.03 due to the small wire diameter at high η. Therefore, there was no x-ray confirmation of the presumed recrystallization. Moreover, the small size of the grains at $\eta > 12$ made it difficult to follow Kikuchi bands to ascertain crystallographic orientation by electron diffraction in the TEM. This lack of direct confirmation of recrystallization notwithstanding, the presence of equi-axed phases with a size at $\eta > 12$ that is coarser than the phase spacing at lower η leaves little alternative but to conclude that the material has recrystallized.

At deformation processing true strains greater than $\eta = 7.27$, the convoluted ribbon phase morphology was replaced by a simple equiaxed grain structure (Figures 37-38). Although this microstructure had a small average grain size (200 to 230nm), the change in the shape of both the Ti and Y grains indicates that the plate-like filaments of Ti and Y were changed to shapes nearer those of cylinders and/or spheres. The driving force for such change is the reduction in surface energy associated with reducing the interphase surface area within the sample and by increasing the radii of curvature of these boundaries, as described by Malzahn, Kampe, and Courtney [42-43] during the 700° C recovery anneals used in the wire drawing process at G & S Titanium. This process occurs more readily at high η levels since the filament edge radii become exceedingly small for filaments smaller than about 50 to 100nm, and the driving force for coarsening associated with interfacial surface energy becomes large as the total interfacial area increases at high η values. The selection of 700° C for the annealing temperature was based upon handbook values for pure Ti recovery and recrystallization, hot-stage TEM studies conducted on Ti-50Y specimens deformation processed to $\eta = 4.8$, and upon experience with earlier specimens of Ti-20Y and Ti-50Y deformation processed to $\eta = 7.6$. None of these sources of information was entirely

appropriate to a Ti-20Y composite deformation processed beyond $\eta = 7.6$, and it appears the filamentary structure was unstable to spheroidization at 700° C.

As noted earlier, x-ray texture specimens were not prepared at η values greater than 5.03 due to the small wire diameter at high η. Therefore, there was no x-ray confirmation of the presumed recrystallization. Moreover, the small size of the grains at $\eta > 12$ made it difficult to follow Kikuchi bands to ascertain crystallographic orientation by electron diffraction in the TEM. This lack of direct confirmation of recrystallization notwithstanding, the presence of equi-axed phases with a size at $\eta > 12$ that is coarser than the phase spacing at lower η leaves little alternative but to conclude that the material has recrystallized.

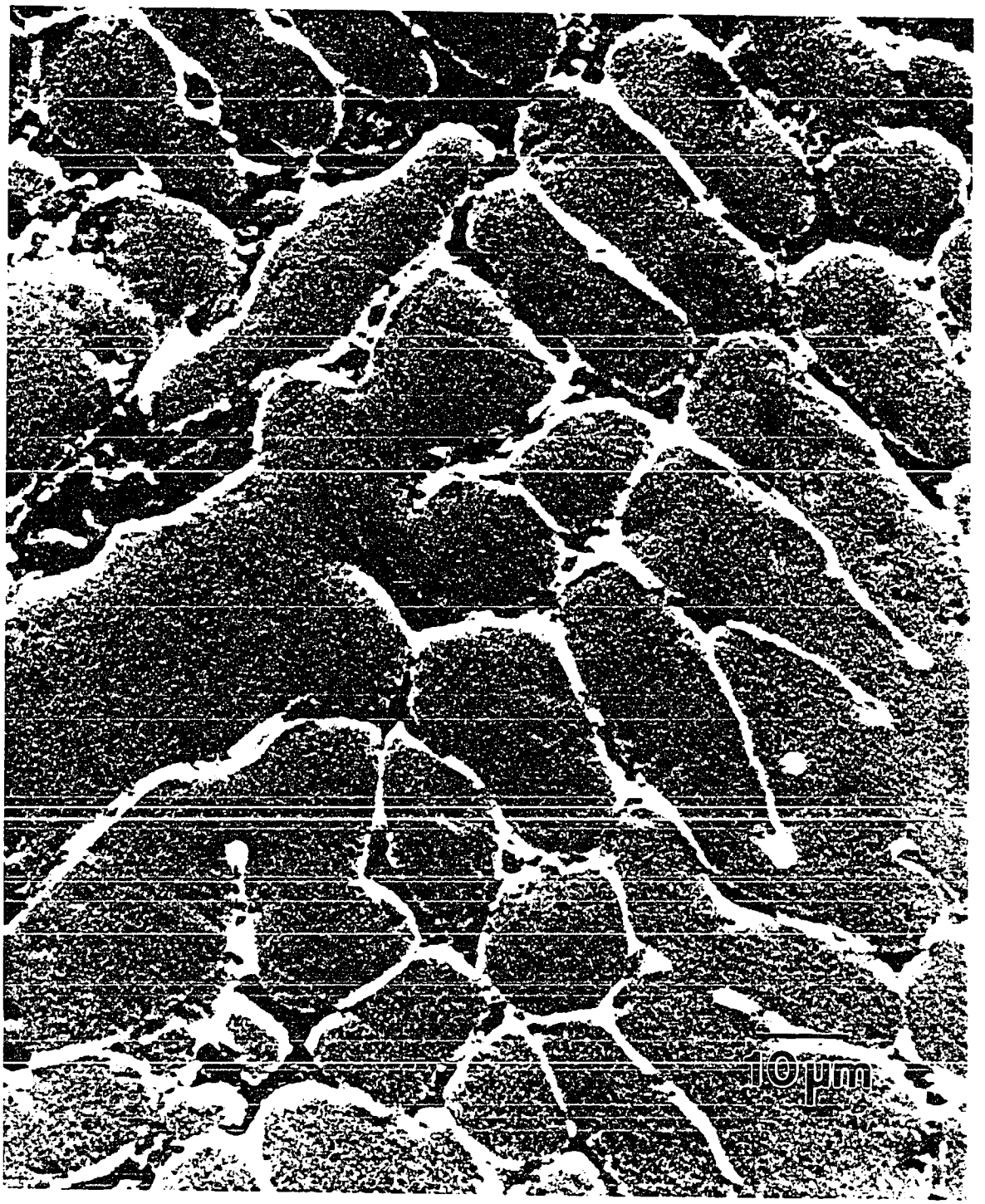

Figure 32. Back-scattered electron image SEM micrograph of Ti-20Y as-cast ($\eta = 0$). The light gray areas are Y and the dark gray areas are Ti

Figure 33. Back-scattered electron image SEM micrograph of Ti-20Y as-extruded ($\eta = 2.25$) shown in transverse section. The light gray areas are Y and the dark gray areas are Ti

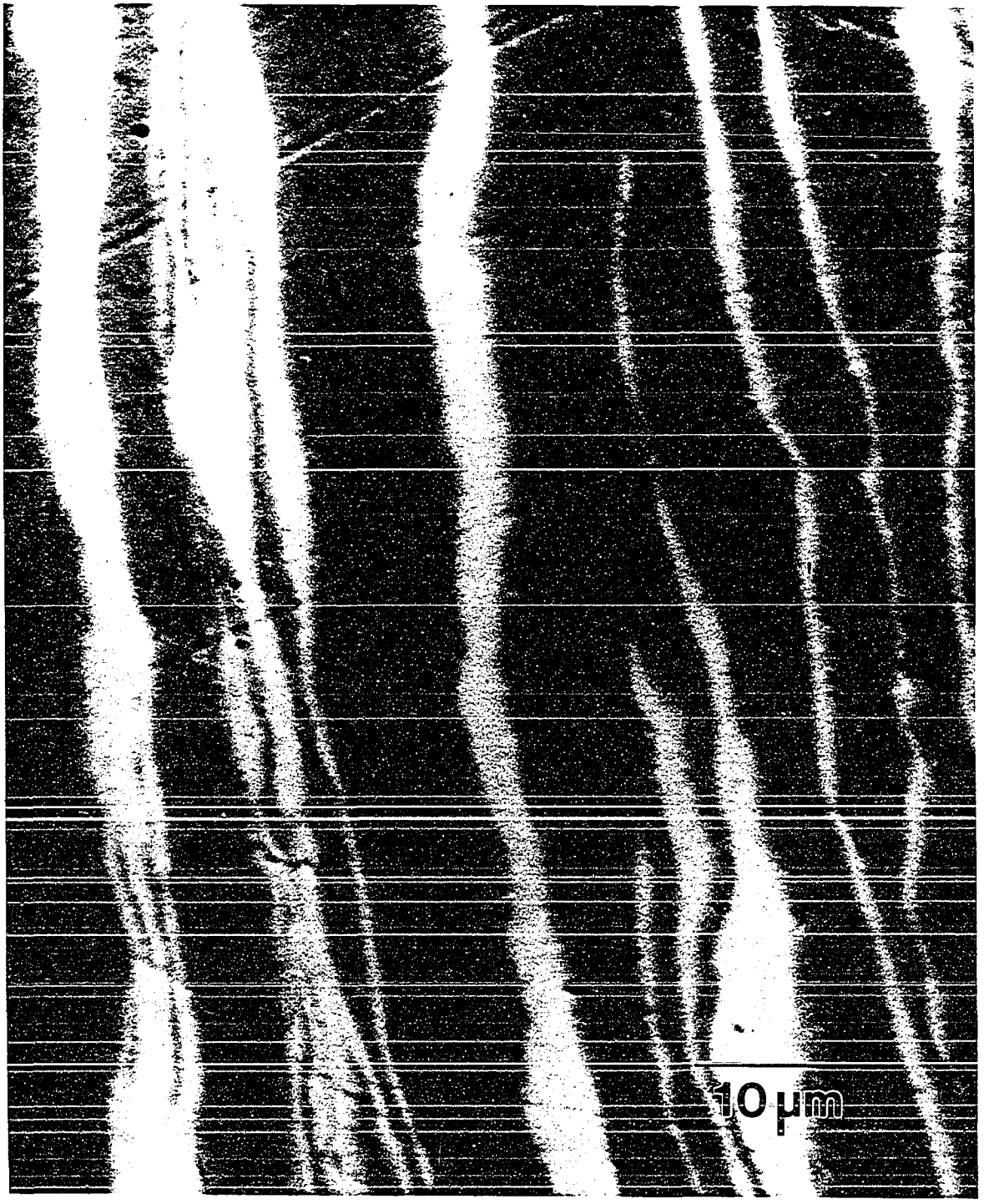

Figure 34. Back-scattered electron image SEM micrograph of Ti-20Y as-extruded ($\eta = 2.25$) shown in longitudinal section. The light gray areas are Y and the dark gray areas are Ti

Figure 35. Conical scan dynamic dark field TEM micrograph of Ti-20Y deformation processed to $\eta = 5.03$ and sectioned transversely. The light gray areas are Ti and the dark gray areas are Y. Note the similarity in phase shape to the Cu-20Nb specimen shown in Figure 3.

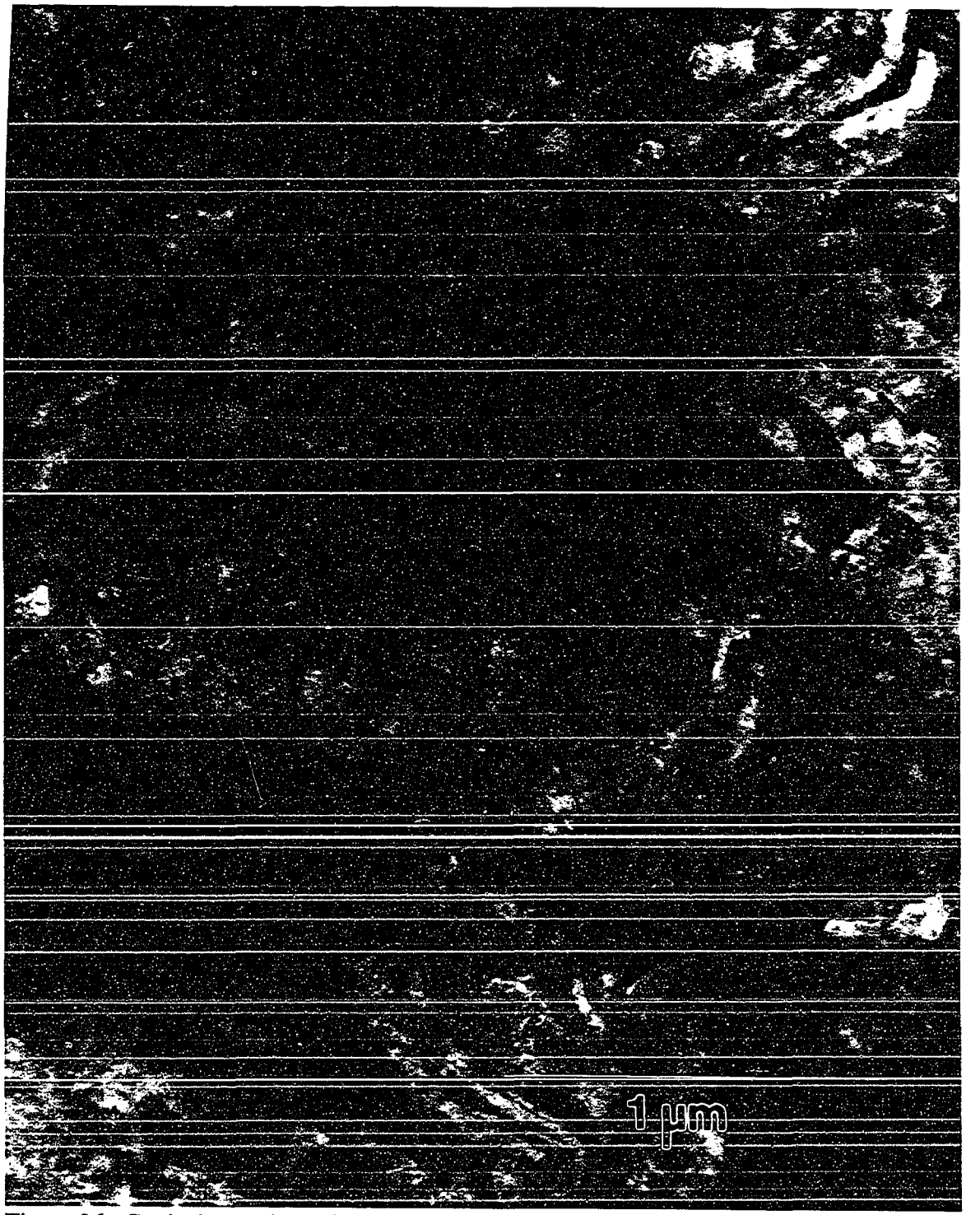

Figure 36. Conical scan dynamic dark field TEM micrograph of Ti-20Y deformation processed to $\eta = 7.27$ and sectioned transversely. Note the presence of some recrystallized phase shapes among the preponderance of convoluted ribbon shapes.

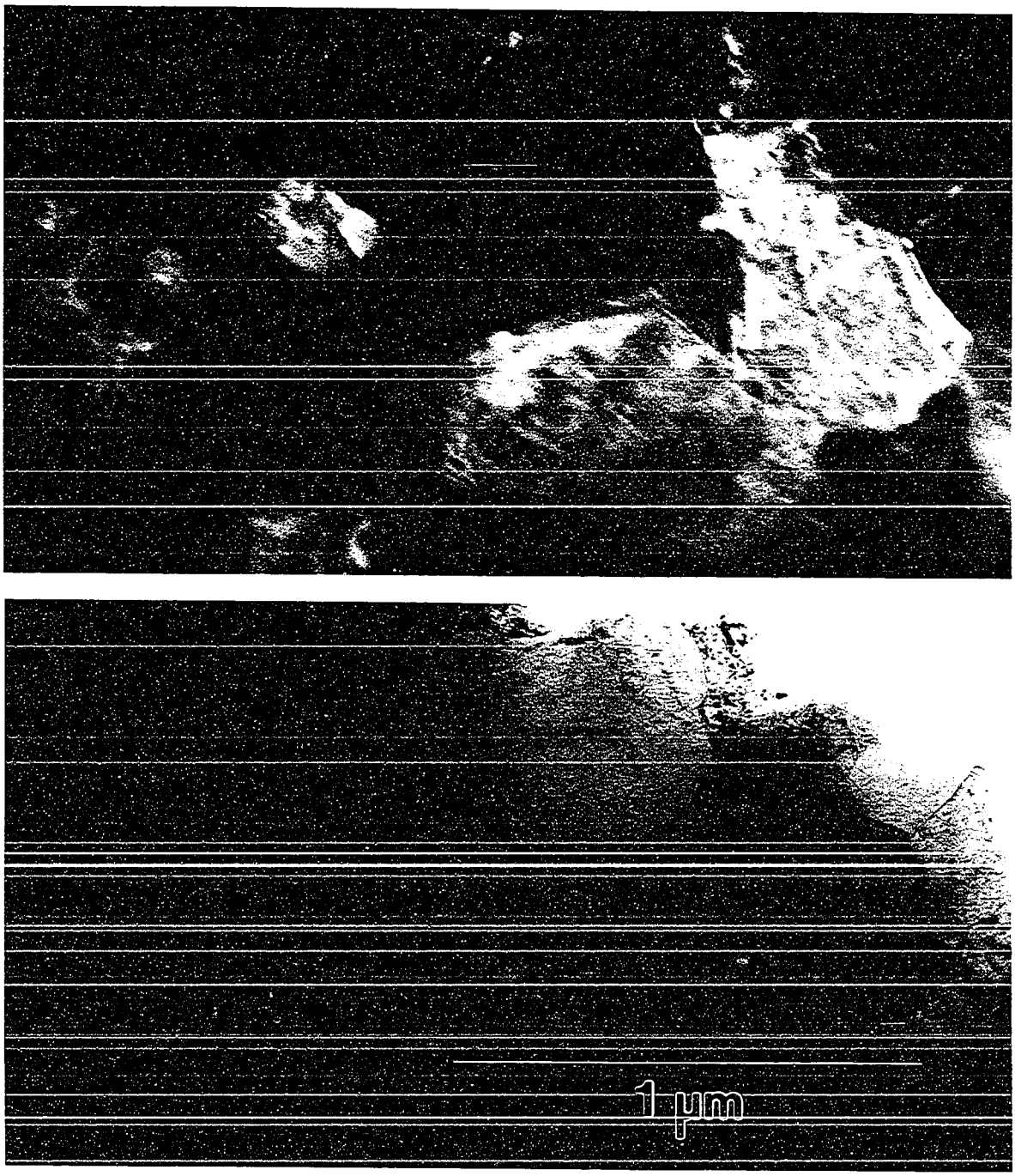

Figure 37. Conical scan dynamic dark field (top) and bright field (bottom) TEM micrographs of Ti-20Y deformation processed to $\eta = 12.3$, annealed at 700° C., and sectioned transversely. In dark field the light gray crystals are Y; the dark gray crystals are Ti, as confirmed by energy dispersive spectrometry. Note the generally equi-axed grains and the lack of filamentary microstructure compared to Figures 33-35

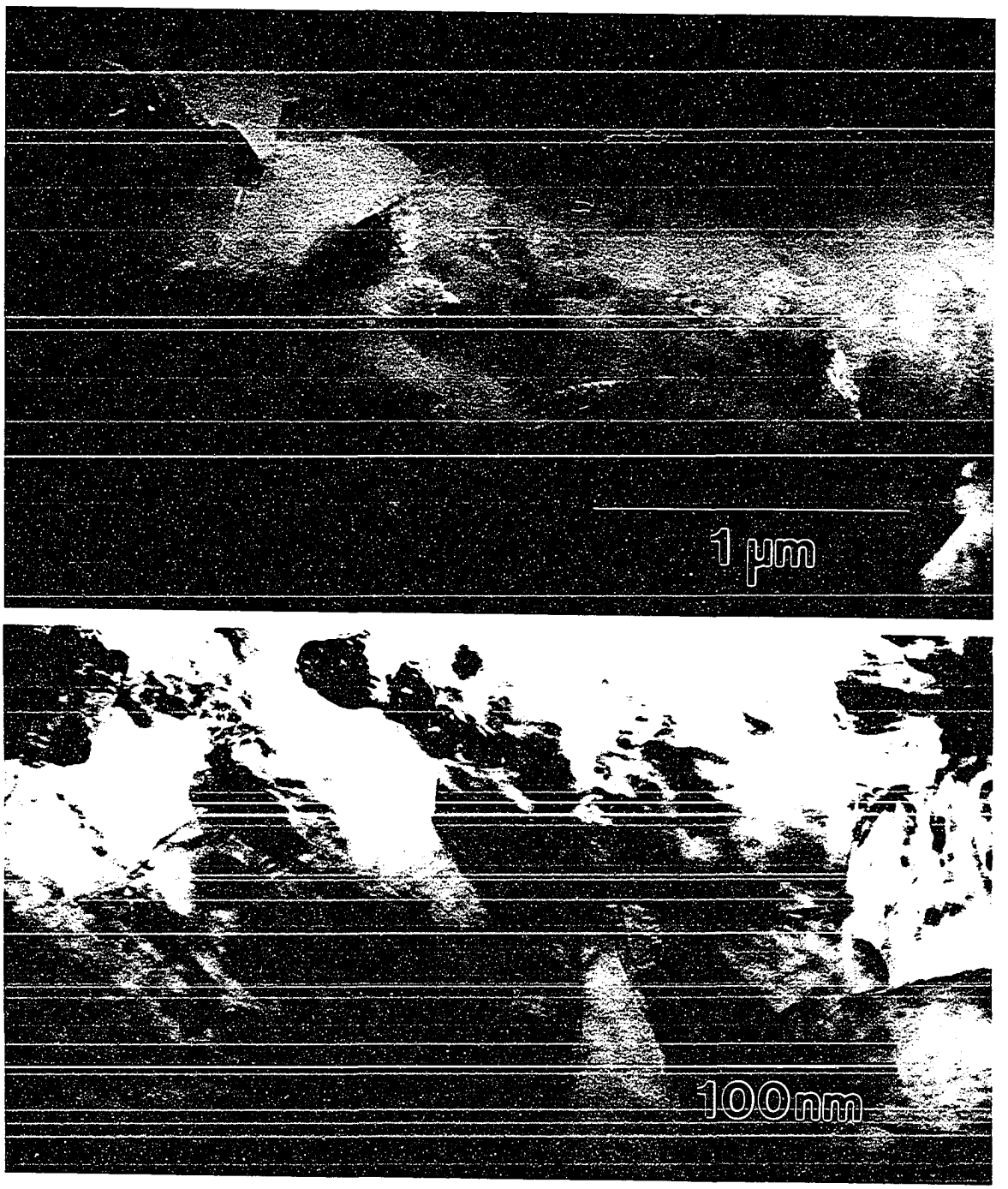

Figure 38. Conical scan dynamic dark field (top) and bright field (bottom) TEM micrographs of two different areas in Ti-20Y deformation processed to $\eta = 12.8$ and sectioned transversely. This specimen was cold-worked to a 60% reduction in area by drawing with no subsequent anneal. Note incipient formation of chevron pattern phase boundaries presumably caused by plane strain in the Ti and Y phases

Since the Ti-20Y at η = 12.3 and 12.8 had recrystallized, probably repeatedly, and lost the phase shape seen at lower η values, the phase thickness measurements obtained with these specimens were not included in the semilogarithmic plot of average phase thickness versus deformation processing true strain (η) shown in Figure 39. Comparison of phase thicknesses between those phases in Ti-20Y possessing the ribbon-shaped filaments and those phases in Ti-20Y possessing an approximately equi-axed structure would be of limited interest, since the different phase shapes would presumably change the strength-microstructure relationship. It should be noted also that, although the Cu matrix in Cu-X deformation processed composites undergoes dynamic recrystallization at room temperature, the X phase ribbon-shape is maintained to the highest η values observed.

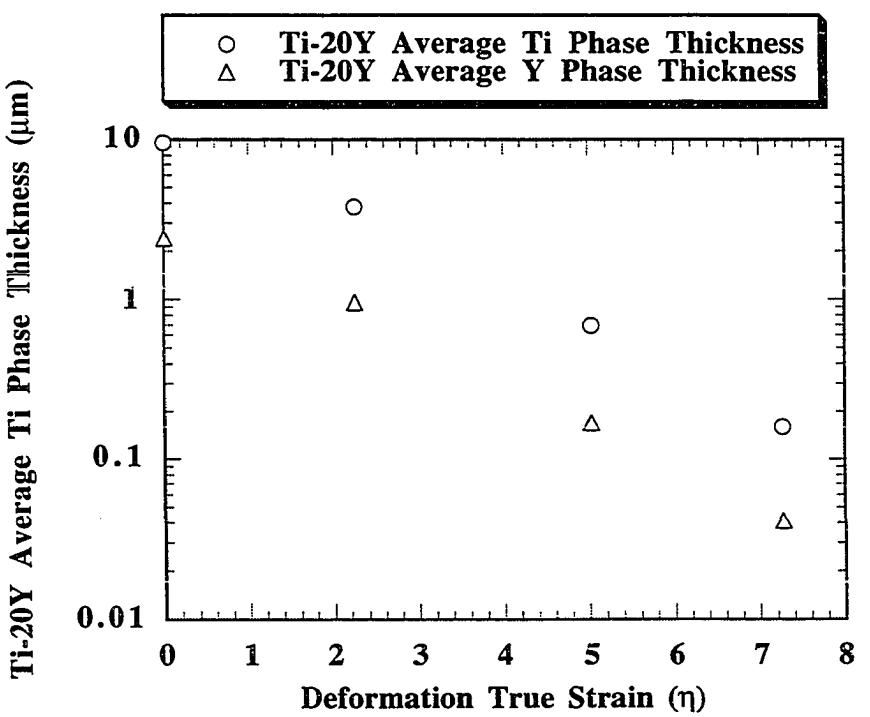

Figure 39. Plot of average phase thicknesses versus deformation processing true strain for Ti-20Y

Tensile Test Results

The Cu-X and other cubic crystal deformation processed composites are greatly strengthened by deformation processing. Higher levels of true strain (η) have resulted in higher yield strengths and higher ultimate tensile strengths in every cubic deformation processed composite studied to date. One of the purposes of this study was to determine whether a deformation processed composite comprised of two immiscible hexagonal close packed metals would also be strengthened and to compare such strengthening with the strengthening experienced by a similarly processed specimen of pure Ti. The ultimate tensile strength and ductility measurements for the pure Ti and Ti-20Y are shown in Table 4.

Table 4. Ultimate tensile strength and ductility measurements for tensile specimens of Ti-20Y and pure Ti

Specimen	Ultimate Tensile Strength (MPa)	Ductility: Reduction in Area at Fracture Surface
Ti-20Y as-cast ($\eta = 0$)	242	38%
Ti-20Y as-cast ($\eta = 0$)	242	36%
Ti-20Y as-extruded ($\eta = 2.25$)	307	47%
Ti-20Y as-extruded ($\eta = 2.25$)	298	48%
Ti-20Y ($\eta = 5.03$)	649	45%
Ti-20Y ($\eta = 5.03$)	662	45%
Ti-20Y ($\eta = 6.82$)	813	37%
2nd generation Ti-20Y ($\eta = 7.0$)	731	52%
Ti-20Y ($\eta = 7.27$)	949	42%
Ti-20Y ($\eta = 9.24$)	753	45%
2nd generation: Ti-20Y ($\eta = 10.0$)	705	59%
2nd generation: Ti-20Y ($\eta = 10.0$)	671	63%
2nd generation: Ti-20Y ($\eta = 10.0$)	695	55%
Ti-20Y ($\eta = 12.3$) (full anneal)	708	61%

Table 4. (continued)

Ti-20Y (η = 12.3) (full anneal)	678	37%
Ti-20Y (η = 12.3) (full anneal)	708	56%
Ti-20Y (η = 12.8)(60% cold work)	727	11%
Pure Ti as-cast (η = 0)	275	79%
Pure Ti as-cast (η = 0)	265	76%
Pure Ti as-extruded (η = 2.25)	272	88%
Pure Ti as-extruded (η = 2.25)	268	88%
Pure Ti (η = 5.03)	550	68%
Pure Ti (η = 5.03)	542	70%
Pure Ti (η = 6.82)	684	70%
Pure Ti (η = 6.82)	690	68%
2nd generation Pure Ti (η = 7.00)	557	84%
Pure Ti (η =7.27)	832	63%
2nd generation Pure Ti (η = 7.87)	490	75%
2nd generation Pure Ti (η = 7.87)	491	76%
2nd generation Pure Ti (η = 9.19)	597	75%
2nd generation Pure Ti (η = 9.19)	547	76%
2nd generation Pure Ti (η = 9.53)	530	76%

These data, plotted in Figures 40-43, show pure Ti steadily increasing in UTS as η increases from 0 to 7.27, the highest level of deformation processing performed on the pure Ti during the deformation processing done at G & S Titanium. This increase presumably results from the grain size refinement and work hardening accompanying such large strains.

In the previously described "second generation" deformation processing performed at Ames Laboratory from η = 5.03 to 10.0, the pure Ti specimens had ultimate tensile strengths (UTS) somewhat lower than the values seen for the material drawn at G & S Titanium. The pure Ti at η = 6.82 from G & S Titanium averaged 687 MPa while the pure Ti produced in the second generation at Ames had a UTS of 557 MPa at η = 7.00. This difference is not

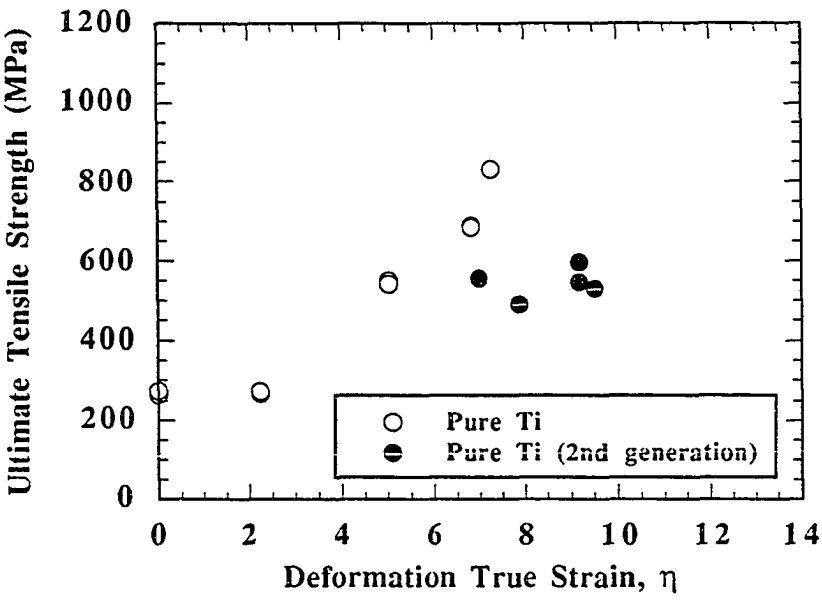

Figure 40. Ultimate tensile strength versus deformation processing of pure Ti by extrusion, swaging, and wire drawing

surprising since the second generation piece was hot worked from $\eta = 5.03$ to 5.71, which would be expected to produce less work hardening than the piece deformation processed at G & S Titanium by cold work from $\eta = 2.25$ to 6.82.

The $\eta = 7.27$ pure Ti piece from G & S Titanium (UTS = 832 MPa) was markedly stronger than the second generation pure Ti pieces deformation processed in Ames to $\eta =$ 7.87, 9.19, and 9.53 which all had UTS values in the range 490 to 597 MPa. The specimen deformed at G & S Titanium was wire drawn and annealed at 700° C. after each 60% reduction in area; the specimens deformed in Ames were swaged and annealed at 600° C. after each two swaging dies (corresponding to approximately a 25% reduction in area). The piece received from G & S Titanium had been cold worked to the full 60% reduction in area

and was not subsequently annealed, while the Ames Laboratory specimens had all been cold-worked to about 25% prior to tensile testing. Thus, the higher strength of the drawn material may be attributable to its higher level of cold work. The ductilities of these pure Ti specimens are consistent with this explanation; there was less ductility in the pure Ti tensile specimen at $\eta = 7.27$ (63% reduction in area) compared to the second generation pure Ti specimens at $\eta = 7.00$ (84% reduction in area) and $\eta = 7.87$ (75% and 76% reduction in area).

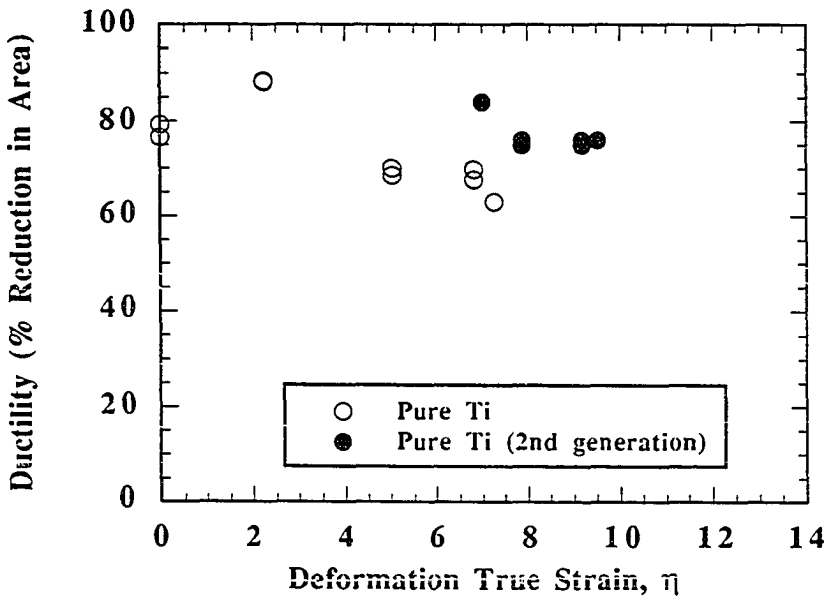

Figure 41. Ductility as percent reduction in area of the tensile specimen fracture surface for pure Ti

The most noteworthy feature of the Ti-20Y plot of ultimate tensile strength versus deformation true strain (Figure 42) is the decline in strength seen at high η values. This decrease is seen in both the Ti-20Y deformation processed at G & S Titanium with 700° C. anneals and in the second generation material deformation processed at the Ames Laboratory

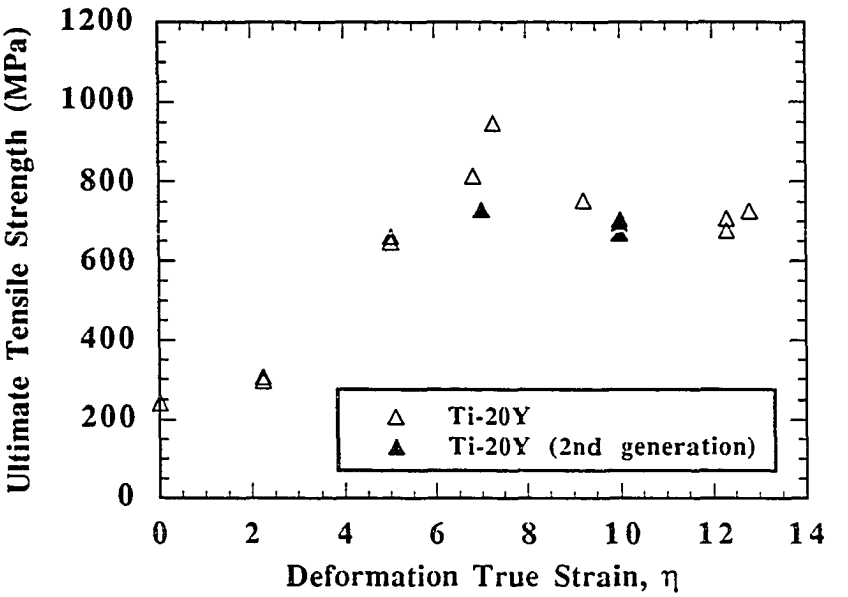

Figure 42. Ultimate tensile strength versus deformation processing of Ti-20Y composite by extrusion, swaging, and wire drawing

with 600° C. anneals. The decrease in strength is to be expected with the spheroidization and loss of filamentary structure of the high η specimens noted in the previous section (Figures 37-38). Since this loss of filamentary structure represents a major change from the phase morphology for which the various mathematical models of strengthening in a deformation processed composite were developed [2,6,9,17,18,19,21-24,27], the following discussion for Ti-20Y is limited to the deformation processing range $0 \leq \eta \leq 7.27$.

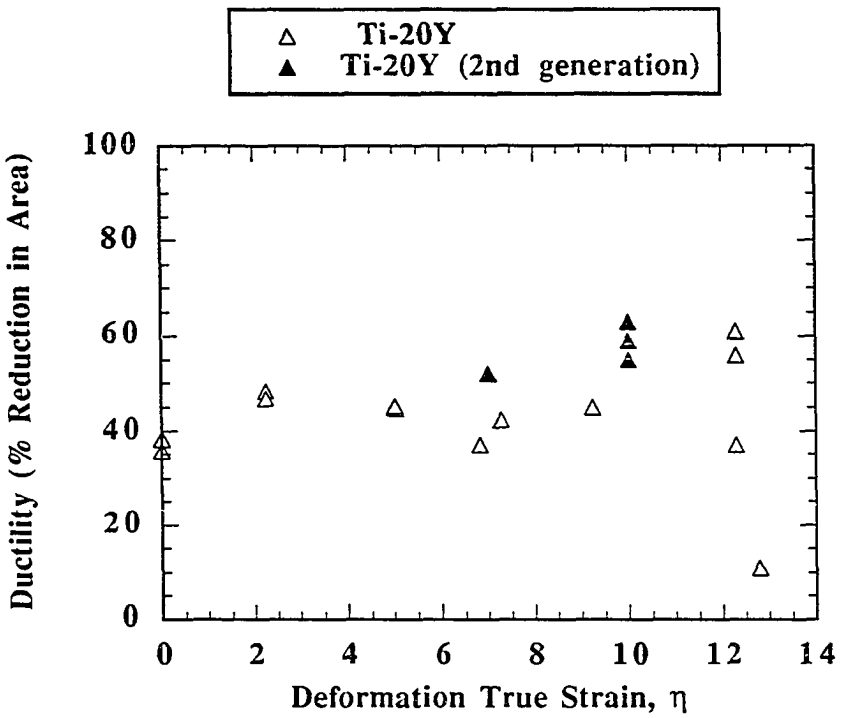

Figure 43. Ductility as percent reduction in area of the tensile specimen fracture surface for Ti-20Y composite

The Ti-20Y data obtained in this study were used in three of the mathematical models described in the introductory section to compare the predicted fit of the models to the data obtained in this study. The three models employed were:

1. The rule of mixtures [18]
2. The Embury and Fisher modified Hall-Petch relation [2]
3. The Verhoeven, Chumbley, Laabs, and Spitzig adaptation [21] of Sevillano's [22] modification of the rule of mixtures

The other three models discussed in the introductory section were deemed a poor fit to the conditions of this Ti-20Y deformation processing experiment. The Funkenbusch, Lee, and Courtney model [24] is predicated on the assumption that the increase in dislocation density in the metals of the composite is the principal reason for the composite's high strength. However, the Ti-20Y specimens differ from the Cu-X composites because they were periodically annealed at temperatures well above the recovery temperatures for Ti and Y. The large dislocation densities associated with deformation processing would be greatly reduced during each anneal. This is corroborated by the TEM specimens of the Ti-20Y; although no quantitative data were taken from these micrographs, they did not display particularly high dislocation densities.

The model of Morris and Morris [19] was developed to account for both phase size/spacing effects and for the solute strengthening effect of Fe dissolved in the Cu matrix. Since the mutual solubilities of Ti and Y are essentially zero [34] in the temperature range of the Ti-20Y deformation processing (20° - 800° C.), solute strengthening effects should be negligibly small in Ti-20Y.

Finally, the Koehler strengthening model was postulated for lamellar structures having nearly equal lattice parameters. Since the Ti and Y phases in these Ti-20Y composite specimens were not lamellar and the lattice parameters of these two metals differ by 24%, the Koehler model assumptions were a poor fit to the Ti-20Y situation.

The simple rule of mixtures model assumes that the two phases present (in this case, Ti and Y) act as simple "load sharing columns" which bear the load placed upon the composite in direct proportion to the volume fraction of each phase present in the composite. The model assumes no losses or gains in the strength of the overall composite attributable to the bonding strength between the two phases or to the effects of phase boundaries and spacing on dislocation propagation and motion. Mathematically, the rule of mixtures can be expressed as:

$$\sigma_{c,uts} = \sigma_{f,uts} V_f + \sigma_{m,uts} V_m$$

where $\sigma_{c,uts}$ is the ultimate tensile strength of the deformation processed composite, $\sigma_{f,uts}$ and $\sigma_{m,uts}$ are the ultimate tensile strengths of the fiber and matrix materials respectively, each deformed to the same true strain as the composite, and V_f and V_m are the volume fractions of the filament and matrix components of the composite.

Substituting the data from Tables 3 and 4 into this equation along with data from Carlson, et alia, for pure Y [35], one can calculate a predicted $\sigma_{c,uts}$ value for Ti-20Y for each η value from 0 to 7.27. The resulting values are tabulated in Table 5 and plotted in Figure 44. As is the case with the Cu-X and other deformation processed composites, the rule of mixtures underestimates $\sigma_{c,uts}$. Although the prediction error is not large, the fact that the rule of mixtures underestimation grows steadily worse as the phase thickness decreases at higher η values, suggests that phase thickness plays an increasingly important role in strengthening Ti-20Y as the phase thickness becomes smaller.

No data were available on the work hardening rate of pure Y at very large strains. The value of 245 MPa for predicted $\sigma_{c,uts}$ at both $\eta = 0$ and $\eta = 2.25$ follows from the assumption that no work hardening occurs in the Y phase during the 800° C. extrusion (i.e. $\sigma_{Y,UTS}$ does not change). This assumption is consistent with the fact that the averages of the experimentally measured $\sigma_{Ti,\,UTS}$ values in the pure Ti control specimen are the same for both $\eta = 0$ and $\eta = 2.25$ (see Table 4).

The values of $\sigma_{Y,UTS}$ used at $\eta = 5.03$ and $\eta = 7.27$ were obtained from large extrapolations of the Y tensile test work hardening rate data measured by Carlson, et alia, [35]; consequently, the values of $\sigma_{Y,UTS}$ used may be somewhat inaccurate. However, since the Y term constitutes only 20% of the total for $\sigma_{c,uts}$ the effect of this possible error on the predicted value of $\sigma_{c,uts}$ will presumably be modest.

Table 5. Experimental values of $\sigma_{c,uts}$ and values of $\sigma_{c,uts}$ predicted by the rule of mixtures for Ti-20Y

	$\eta = 0$	$\eta = 2.25$	$\eta = 5.03$	$\eta = 7.27$
actual $\sigma_{c,UTS}$ (MPa)	242	302	655	949
predicted $\sigma_{c,UTS}$ (MPa)	245	245	514	747

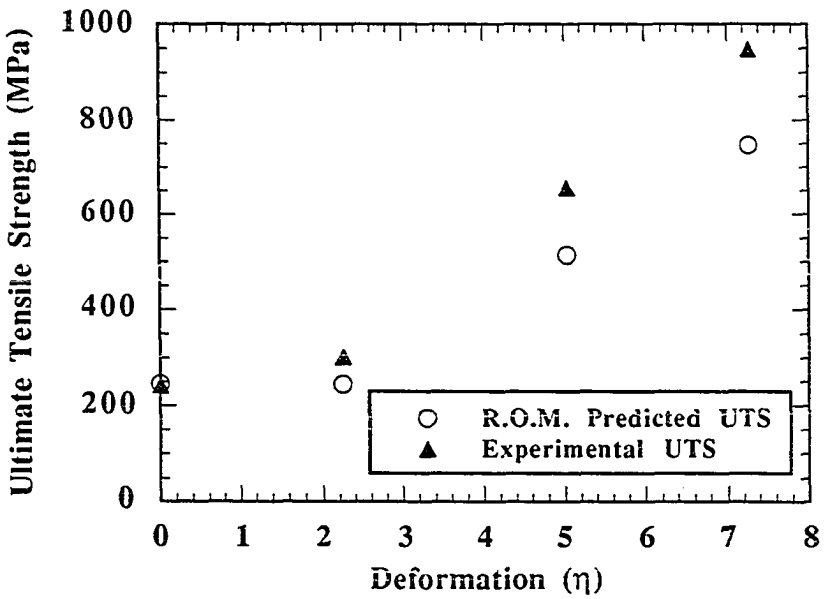

Figure 44. Comparison of the $\sigma_{c,uts}$ values predicted by the rule of mixtures with the experimental values obtained for Ti-20Y

The data obtained in this experiment were also compared with the predicted fit of the Embury and Fisher modified Hall-Petch model. As described in the introduction, Embury and Fisher reasoned that the spacing of barriers to dislocations within and between phases will be reduced in direct proportion to the reduction in the overall diameter of the specimen wire as it is drawn:

$$1/r_e = (1/r_o)(D_o/D_e)$$

where the barrier spacing before strain is r_o, the barrier spacing after strain is r_e, the specimen diameter before strain is D_o, and the specimen diameter after strain is D_e. As described previously, this expression can be combined with the Hall-Petch relation to obtain:

$$\sigma_y = \sigma_0 + K(c)^{-0.5}(r_o)^{-0.5}(\exp \varepsilon/4)$$

where c is a geometrical factor of the lattice relating the mean slip distance to the barrier spacing. In pearlite, the ferrite slip planes are at angles of 20° to 70° to the lamellae, so a value of 2 was assumed for c. (A slip plane tilted at these angles to a shortest connecting line between barriers will be roughly twice as long as that shortest connector.) In Ti and Y textured with a $<10\bar{1}0>$ fiber texture, c would also have a value of 2.

To apply this model to the Ti-20Y data, one must first establish the optimal value for the empirical constant K. Optimizing K with the available data on Ti-20Y established a value of K = 800. Using this value of K with the data in Tables 3 and 4 produced the predicted values of $\sigma_{c,uts}$ presented in Table 6 and Figure 45. It should be noted that Embury and Fisher developed their model to predict yield strength, not ultimate tensile strength (UTS). However, the comparison to the experimental UTS values is valid if the ratios of $\sigma_{c,uts}$ to $\sigma_{c,yield}$ are similar for Ti-20Y and pearlitic steel.

The Embury-Fisher model is structured such that it assures a perfect match at $\eta = 0$. The fit of the prediction to the actual measured values is excellent for η = 5.03 and 7.27,

Table 6. Experimental values of $\sigma_{c,uts}$ and values of $\sigma_{c,uts}$ predicted by the Embury-Fisher model for Ti-20Y

	$\eta = 0$	$\eta = 2.25$	$\eta = 5.03$	$\eta = 7.27$
actual $\sigma_{c,UTS}$ (MPa)	242	302	655	949
predicted $\sigma_{c,UTS}$ (MPa)	245	445	648	952

but the predicted value is too high for $\eta = 2.25$. The deviation at $\eta = 2.25$ may be at least partially caused by recrystallization of Ti-Ti grain boundaries within the Ti phases and Y-Y grain boundaries within the Y phases at the 800° C temperature of the extrusion. Recall that the Embury and Fisher model is based on the assumption that no new barriers (i.e. Ti-Y phase boundaries, grain boundaries within a Ti or Y phase, or cell walls within a grain) are generated during deformation and that no existing barriers are destroyed during deformation. However, the data in Table 3 disregard the grain boundaries within the Ti and Y phase fields. These grain boundaries would be expected to grow during the several hours the Ti-20Y cast specimen was held at 800° C during the two extrusion attempts, and it may be that this grain growth substantially reduced the total number of barriers within the Ti and Y phase fields, violating one of the precepts upon which the Embury-Fisher model is established by reducing the number of barriers during the deformation from $\eta = 0$ to $\eta = 2.25$. The constant K was essentially optimized for the $\eta = 5.03$ and 7.27 cases in this calculation since no reasonable fit was possible to the $\eta = 2.25$ case; thus, a good fit at the two higher η values is consistent with this possible explanation of the deviation at $\eta = 2.25$.

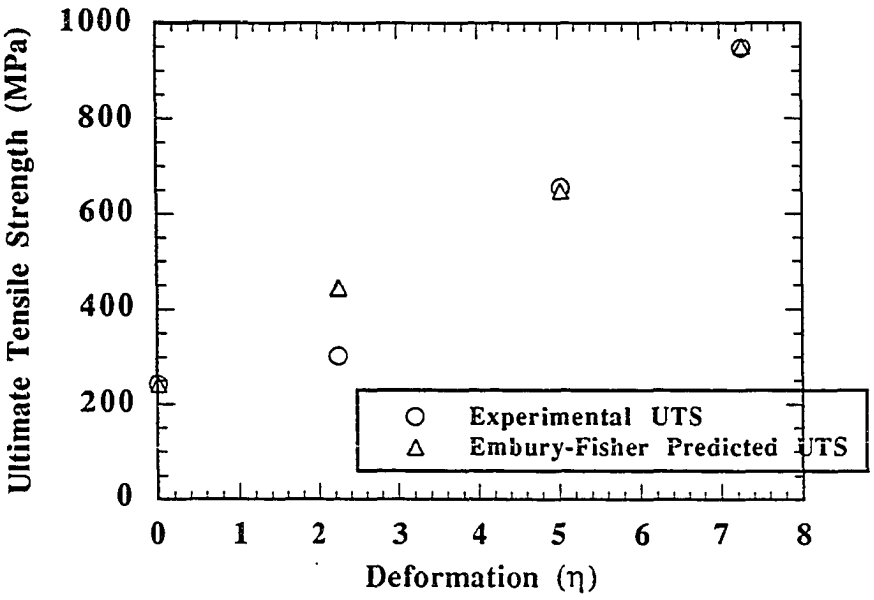

Figure 45. Comparison of the values predicted by the Embury-Fisher model with the experimental values obtained for Ti-20Y

Verhoeven, Chumbley, Laabs, and Spitzig [21] proposed a modification of the rule of mixtures similar to a model proposed by Sevillano [22] for strengthening in pearlite that takes into account the dislocation propagation in both the Cu and Nb phases in a 80 vol. % Cu and 20 vol. % Nb composite:

$$\sigma_c = 0.8\left[\sigma_o + \frac{\mathrm{MAGb}}{2\pi t}\ln\frac{t}{b}\right]_{Cu} + 0.2\left[\sigma_o + \frac{MAGb}{2\pi t}\ln\frac{t}{b}\right]_{Nb}$$

where σ_O(Cu) and σ_O(Nb) = ultimate tensile stress of similarly deformation processed Cu and Nb respectively, M is the Taylor factor (M = 3 in fcc metals, M = 2 in bcc metals), A = 1.21 (weighted average of edge and screw dislocations), G is the shear modulus, b is the Burger's vector magnitude, and t is the thickness between barriers. Adapting this expression to the Ti-20Y case requires use of the following parameters:

$$M = \text{Taylor factor (the reciprocal of the Schmidt factor)} = \frac{1}{0.433} = 2.3$$

A = 1.21 (a weighted average for screw and edge dislocations)

G = shear moduli (45.6 GPa for Ti and 46.1 GPa for Y)

b = Burger's vector magnitude on the $\{10\bar{1}0\}<11\bar{2}0>$ slip system in Ti (0.295 nm) and Y (0.367 nm)

Performing these calculations yields the values presented in Table 7 and Figure 46.

Table 7. Experimental values of $\sigma_{c,uts}$ and values of $\sigma_{c,uts}$ predicted by the Verhoeven, Chumbley, Laabs, and Spitzig model for Ti-20Y

	$\eta = 0$	$\eta = 2.25$	$\eta = 5.03$	$\eta = 7.27$
actual $\sigma_{c,UTS}$ (MPa)	242	302	655	949
predicted $\sigma_{c,UTS}$ (MPa)	256	269	352	605

The model of Verhoeven, Chumbley, Laabs, and Spitzig substantially underestimates the $\sigma_{c,uts}$ values at $\eta = 5.03$ and 7.27. The model is based upon the critical stress necessary to propagate dislocations between phases, and it works well to predict deformation processing strength increases in Cu-X composites. Its inability to do so in Ti-20Y suggests that propagation of dislocations between phases may not be the dominant factor in the strengthening that occurs at low to moderate η values in Ti-20Y. The model of Verhoeven, Chumbley, Laabs, and Spitzig predicts relatively little increase in UTS for phase spacings larger than a few hundred nm; thus, these Ti-20Y composites are predicted to have small increases in their UTS values, since their phase spacings are substantially coarser than those seen in the high η Cu-Nb deformation processed composites. The most pronounced strengthening in Cu-X composites occurs at η values higher than the 7.27 upper limit reached with the Ti-20Y. This is at least qualitatively reasonable since the finest average Ti phase spacing measured in the Ti-20Y specimens was about 160nm, which is somewhat coarser than the phase sizes in Cu-X where the anomalous strengthening becomes pronounced.

The effect of narrow spacings between phases to inhibit the generation of dislocations at Frank-Read sources and their motion through the lattice would not be expected to produce large UTS increases until the phase spacings are reduced to about 100nm or smaller; thus, the observed UTS increases in the Ti-20Y specimens which are larger than this model predicts suggests that ordinary strain hardening and the conversion to a textured structure that limits strain to a plane strain mode may be the primary strengthening factors operating at these lower η levels in Ti-20Y.

It is unfortunate that higher levels of true strain could not be tolerated without either recrystallizing or breaking the Ti-20Y specimens. It is only at phase spacings of about 100nm or smaller that a true test of the validity of the Verhoeven, Chumbley, Laabs, and Spitzig model to the Ti-20Y composites could be made.

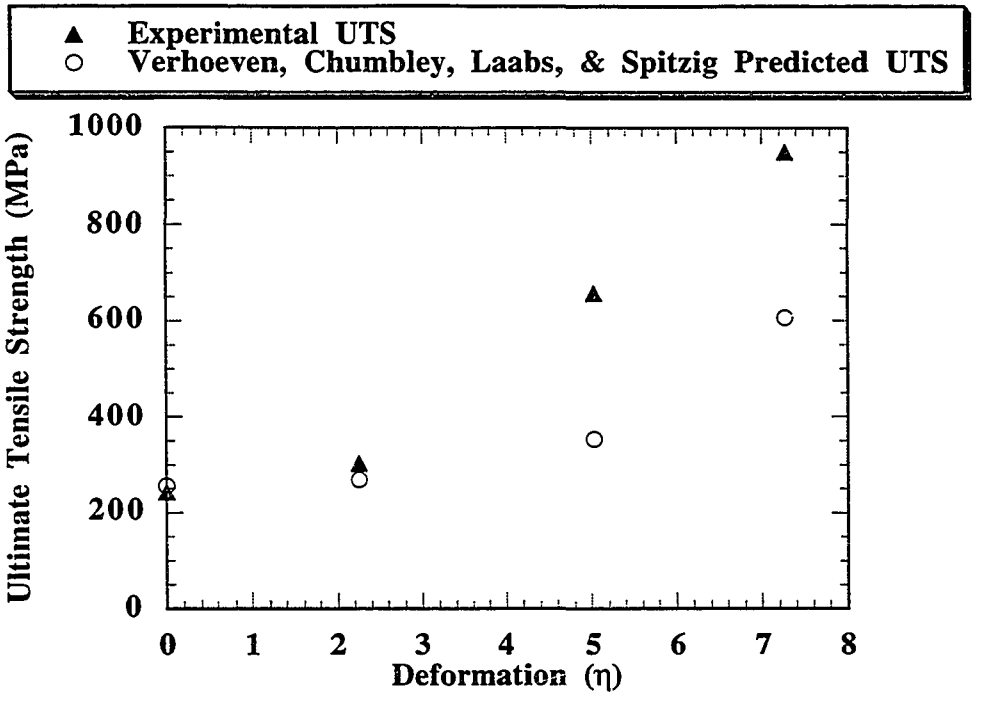

Figure 46. Comparison of the values predicted by the model of Verhoeven, Chumbley, Laabs, and Spitzig with the experimental values for Ti-20Y

Another comparison to the Cu-X data can be made with regard to the relation between phase thickness and ultimate tensile strength. As plotted in Figure 47, the dependence of UTS on Ti phase spacing follows a power function relationship:

$$\sigma_{c,uts} = 522(t_{Ti})^{-0.35}$$

where $\sigma_{c,uts}$ is expressed in MPa and t_{Ti} is the average Ti phase thickness expressed in μm. The absolute value of the slope on a log-log plot of -0.35 for Ti-20Y is somewhat lower than that of -0.47 reported [21] for Cu-20Nb deformation processed composite in the range $0 \leq \eta \leq 4$ and is similar to the slope of -0.38 found for higher η values.

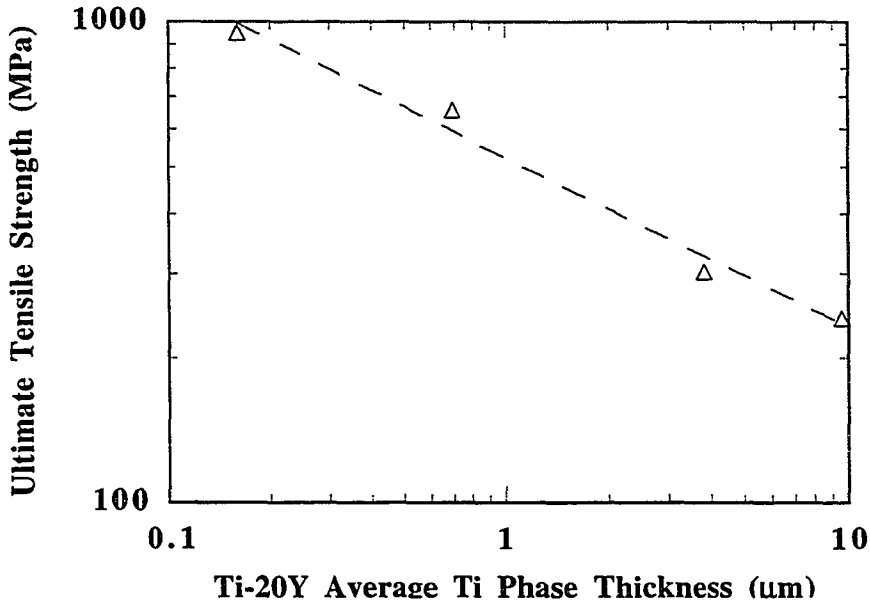

Figure 47. Relation between Ti phase thickness and ultimate tensile strength in Ti-20Y

Verhoeven, et alia attributed the slope change of their Cu-20Nb composite to the change from dendritic structure to the filamentary structure. The observation that no change in slope is apparent in the Ti-20Y composite over the range of $0 \leq \eta \leq 7.27$, even though the Ti-20Y microstructure also changed from a dendritic as-cast structure to a convoluted ribbon structure, suggests that other factors may be involved in the Cu-Nb slope change.

Strengthening model comparisons between Cu-X and Ti-Y composites will always be limited in usefulness by the fact that all phases in Ti-Y are constrained to plane strain. Thus, the key microstructure parameter in Ti-Y may not be the phase thickness used in this analysis, but rather the spacings within each phase between kinks, since these would serve as the real barriers to dislocation motion in plane straining phases.

Geometrical Factors in the Inability of Ti-20Y to Tolerate High Deformations

Throughout the deformation processing operations performed at both G & S Titanium and at Ames Laboratory, the Ti-20Y specimen was never cold worked to a true strain of more than 5.02 without either recrystallizing during recovery anneals or breaking. This same behavior was also observed with earlier experiments performed on smaller specimens of Ti-20Y and Ti-50Y [44] at the Ames Laboratory. This suggests that some fundamental difference exists between the Cu-X composites (which have undergone true strains as large as 13 without breaking) and the Ti-20Y composite.

One possible explanation for this difference in behavior is the number of available slip systems in the Cu matrix of the Cu-X composites and the Ti matrix in the Ti-20Y composite. As previously discussed in the section on "Crystallographic Texture in Cu-X Composites", the Cu matrix acquires a mixture of <111> and <001> fiber textures in these materials, having three or four slip systems respectively, either of which is sufficient to permit axisymmetric deformation. The Ti matrix in Ti-20Y, however, is constrained to plane strain once the $<10\bar{1}0>$ fiber texture develops. Thus, in the Cu-X composites, the Cu matrix comprising 80% of the material volume can flow axisymmetrically to accommodate a plane strain flow of the remaining 20% volume of X. By contrast in Ti-20Y, both the Ti matrix and the Y second phase are constrained to flow by plane strain in a specimen with an overall axisymmetric (cylindrical) shape. This latter situation imposes severe problems of geometrically fitting a material comprised of 100% plane straining phases within a cylinder of diminishing radius.

Figure 48 depicts the extensive shape change that would result from deforming a rectangular prism with initial dimensions of 1 x 1 x 2 units (roughly equivalent to the Ti dendrite aspect ratio in Ti-20Yas can be seen in Figure 32) through plane strains of 0.69 and

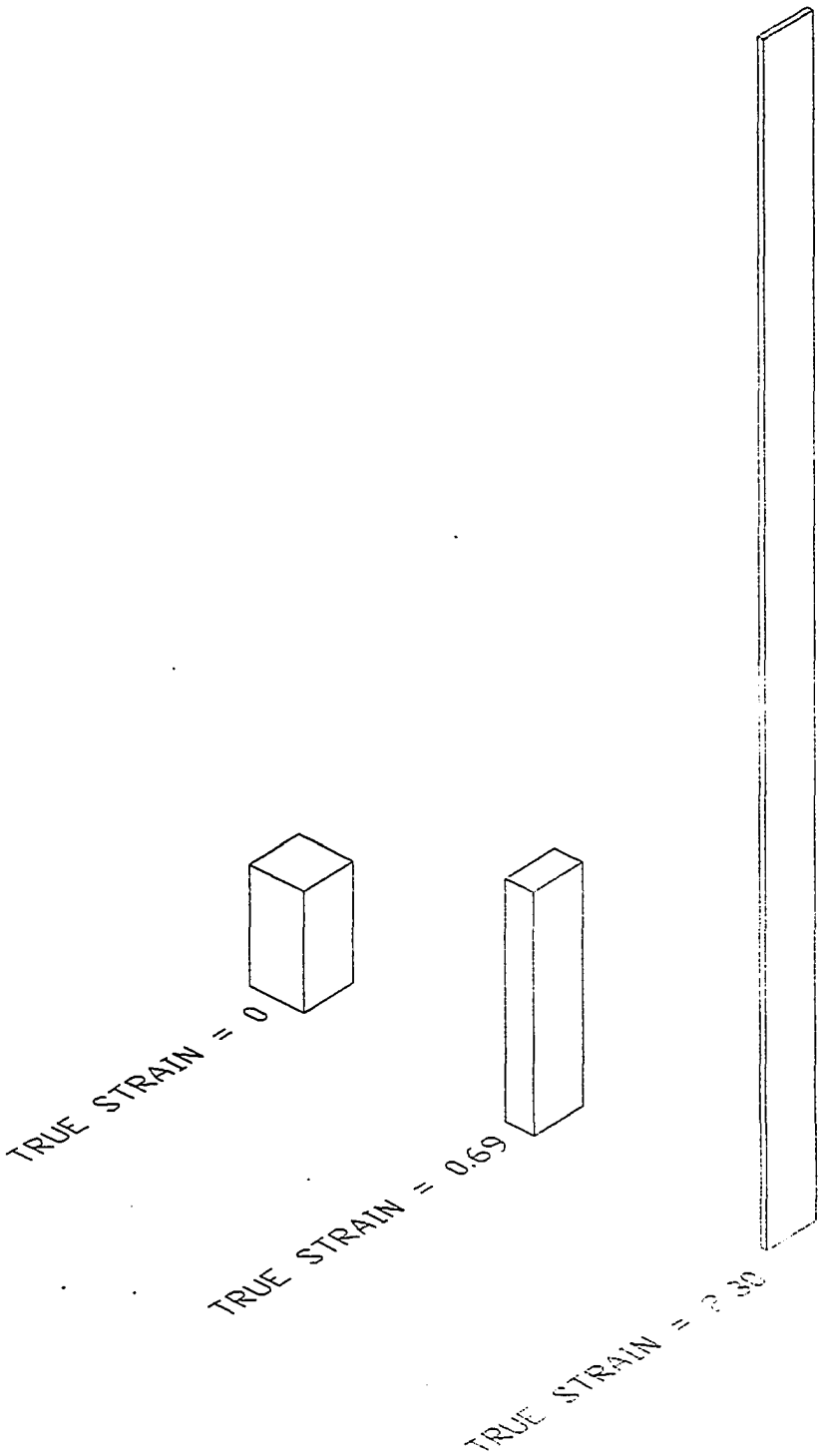

Figure 48. A 1 x 1 x 2 rectangular prism deforming by plane strains of 0.69 and 2.30

2.30. Note that the prism elongates in the vertical dimension and narrows in one, the $<11\bar{2}0>$, of the two transverse dimensions while the other transverse dimension, the <0001> , remains unchanged. Assuming no volume change during this deformation, the prism deformed by plane strain to $\eta = 2.30$ increases 10-fold in height while decreasing 10-fold in thickness. Although not shown on Figure 48, a further deformation by plane strain to a total strain of $\eta = 5$ would result in a prism with a height of nearly 300 units and a thickness of 0.0067 units. Fitting many such plane straining ribbons into an overall cylindrical specimen shape is not a simple task. A valid mathematical determination of a geometrical limit of η for such a situation is unquestionably a formidable problem and may be so complex as to be beyond the "state of the art" of current foliation theory [45]; however, qualitative consideration of some of the possible geometric arrangements to accomodate such deformation is possible and is presented in the following paragraphs.

The upper portion of Figure 49 shows a transverse section of a "tiled" array of polygons representing Ti and Y in an arrangement of 80% by volume Ti and 20% by volume Y which is roughly equivalent to the geometry of the as-cast dendrites observed in Figure 32. The lower portion of Figure 49 depicts one possible geometry for the deformation by plane strain to $\eta = 1.39$ of the "as-cast" polygons. The cruciform array resulting from this deformation is consistent with a plane strain mode of deformation in both the Ti and Y phases, but such a cruciform array allows no contiguous, void-free tiling with neighboring phases also possessing such a cruciform arrangement.

Figure 50 depicts two possible modifications to the simple cruciform array in Figure 49 that permit the arrays to achieve better compatibility with their neighbors. Both Ti and Y textured with the $<10\bar{1}0>$ fiber texture can bend by slip on the basal (0002) plane (see Figures 16 and 29) to achieve the shapes in Figure 50, and in so doing they develop tile shapes which can more nearly fit in a contiguous, void-free arrangement with neighboring arrays, as shown in Figure 51. Figures 52-53 depict an alternative to the cruciform array

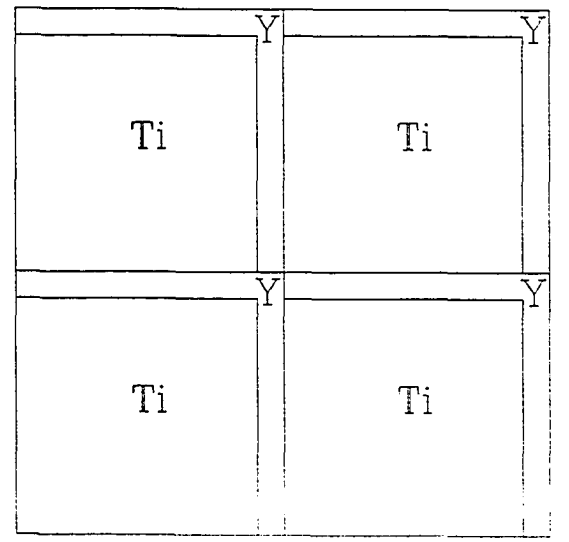

TRUE STRAIN = 0
AS-CAST DENDRITES

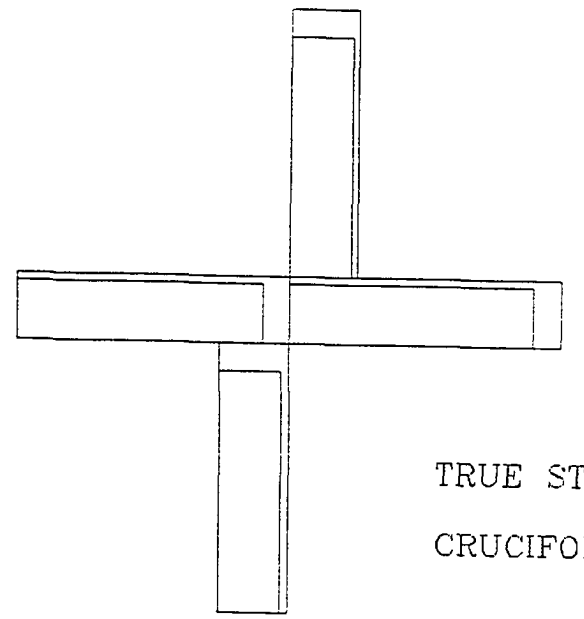

TRUE STRAIN = 1.39

CRUCIFORM ARRAY

Figure 49. Possible tiling arrays for as-cast (above) and $\eta = 1.39$ (below) Ti-20Y

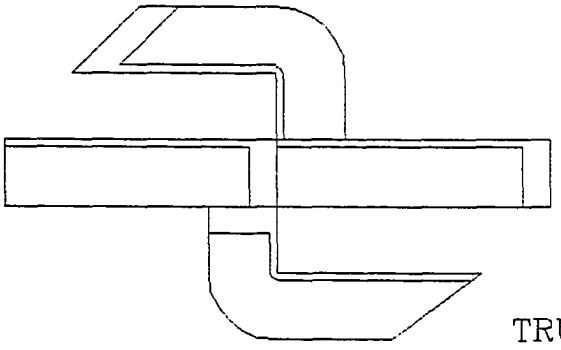

TRUE STRAIN = 1.39
CRUCIFORM ARRAY WITH
PARTIAL PINWHEEL
BENDING

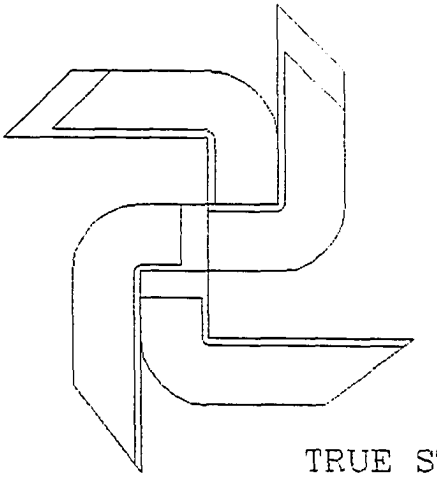

TRUE STRAIN = 1.39
CRUCIFORM ARRAY WITH
PINWHEEL BENDING

Figure 50. Two modifications of the cruciform array in Figure 49 by basal plane (0002) slip bending of the Ti and Y phases

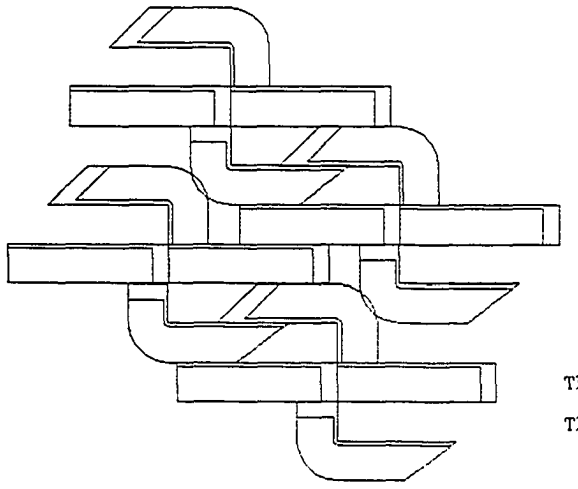

TRUE STRAIN = 1.39

TILING ARRANGEMENT OF 4
CRUCIFORM ARRAYS WITH
PARTIAL PINWHEEL BENDING

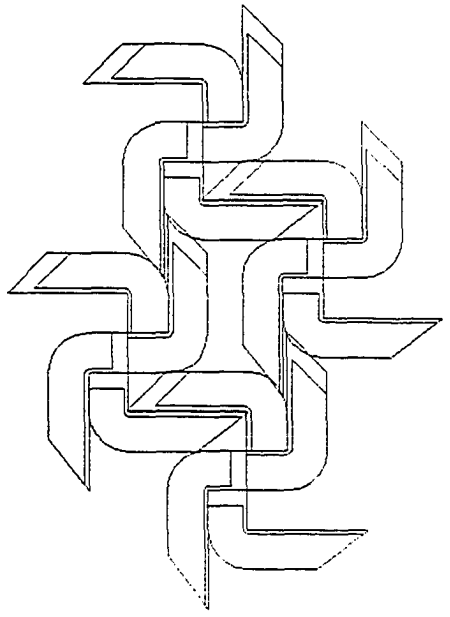

TRUE STRAIN = 1.39

TILING ARRANGEMENT OF 4
CRUCIFORM ARRAYS WITH
PINWHEEL BENDING

Figure 51. Two possible tiling arrangements of the modified cruciform arrays shown in Figure 50 that more nearly fill the available area in a contiguous, void-free tiling

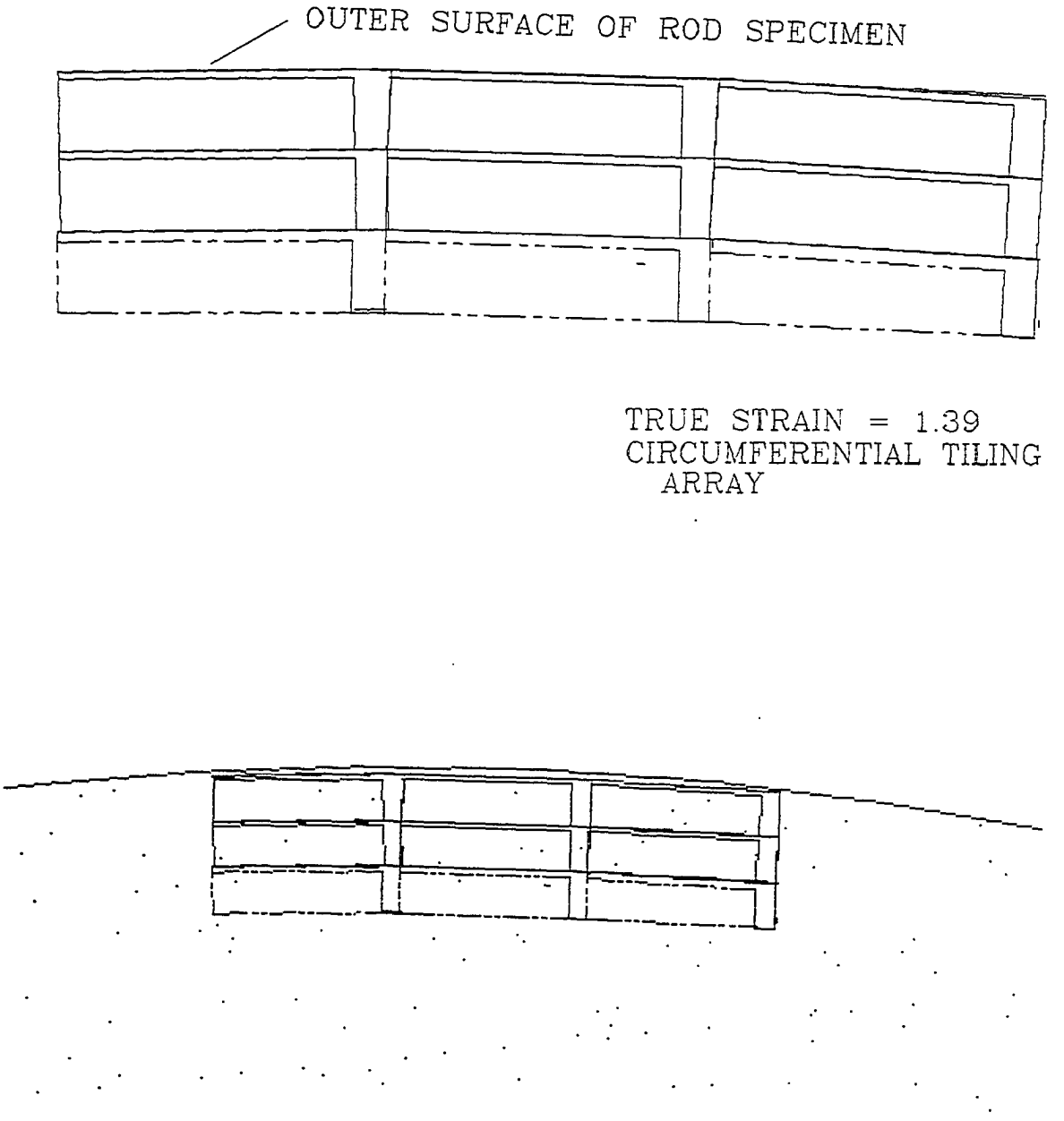

Figure 52. Two views of a possible circumferential ("tree ring") tiling arrangement of Ti-20Y deformed by plane strain to $\eta = 1.39$ where the phases bend slightly by basal slip (0002) to conform to the cylindrical contours of the specimen

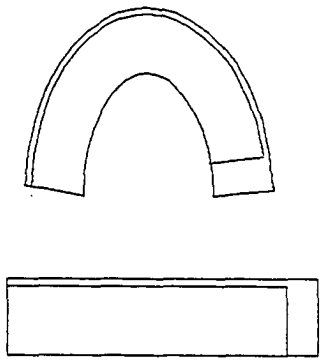

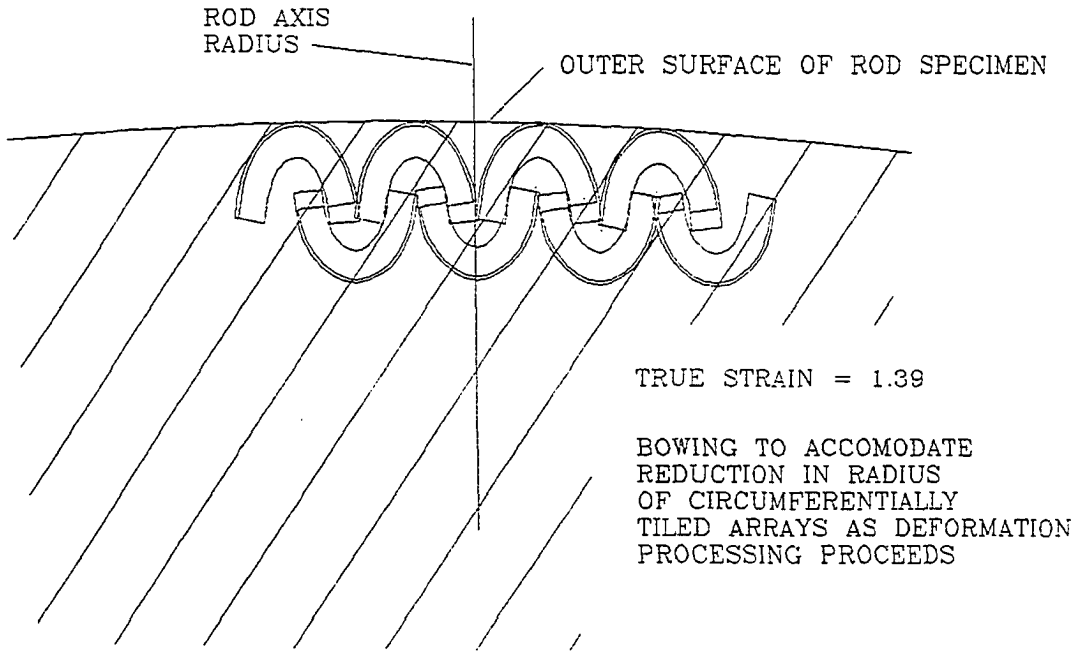

Figure 53. Depictions of possible "bowing" by basal plane slip (0002) of the Ti and Y phases to accomodate further deformation as the specimen radius (and circumference) diminish with continuing deformation processsing

in which the polygons are arranged parallel to the specimen's outer circumference in a pattern similar to the annual growth rings of a tree trunk. Such an arrangement provides a nearly perfect contiguous, void-free array with neighboring tiles; however, it allows for no reduction in the circumference of the array as the specimen size is further reduced by more deformation processing since it positions the dimension which is unchanging in plane strain parallel to the specimen's circumference. A possible accommodation to this problem is shown in Figure 53 where the polygons bend by slip on the Ti and Y basal (0002) planes to accomodate the diminishing circumference caused by further deformation processing. Such bowing of the polygons, however, will be only temporarily adequate to accommodate continuing deformation, since it repositions the polygons in an orientation that does not permit the radius to diminish with still further deformation processing.

The true strain of 1.39 depicted in Figures 49-53 corresponds to a 4:1 reduction ratio by plane strain. Although none of the suggested arrangements offers an ideal accomodation to the plane strain space-filling problem, one can assume that some combination of these various arrays could accommodate the need for both the Ti and the Y to flow by plane strain. The space-filling challenge becomes more severe, however, when one contemplates the 16:1 reduction ratio of $\eta = 2.77$ true strain depicted in Figure 54. Here the large aspect ratio of the polygons magnifies the difficulties in fitting these polygons into the confines of a cylindrical specimen shape. The cruciform array shown in Figure 54 is substantially more difficult to modify by pinwheel bending schemes into any possible arrangement that maintains a contiguous, void-free match with neighboring arrays without necessitating inordinate amounts of grain boundary sliding. The only apparent means to accommodate the diminishing radius and circumference of the specimen is to employ circumferential "tree ring" tiling schemes with more than one bend, rather like the convoluted bending patterns seen in Figure 35 of Ti-20Y cold worked an additional $\eta = 2.78$ after hot extrusion. Even at that, the Y filaments in Figure 35 can be seen to contain numerous fractures (visible as

narrow white cracks across the Y filaments) where the accommodation stresses exceeded the Y fracture strength.

It should be noted that all the hypothetical tiling arrays discussed here are indistinguishable from one another by x-ray texture analysis. Every arrangement considered is predicated on the assumption that a $<10\bar{1}0>$ fiber texture exists in the metal, and thus only phase shapes from the micrographs can be used to judge how nearly the various tiling schemes match the actual deformation pattern of the composite.

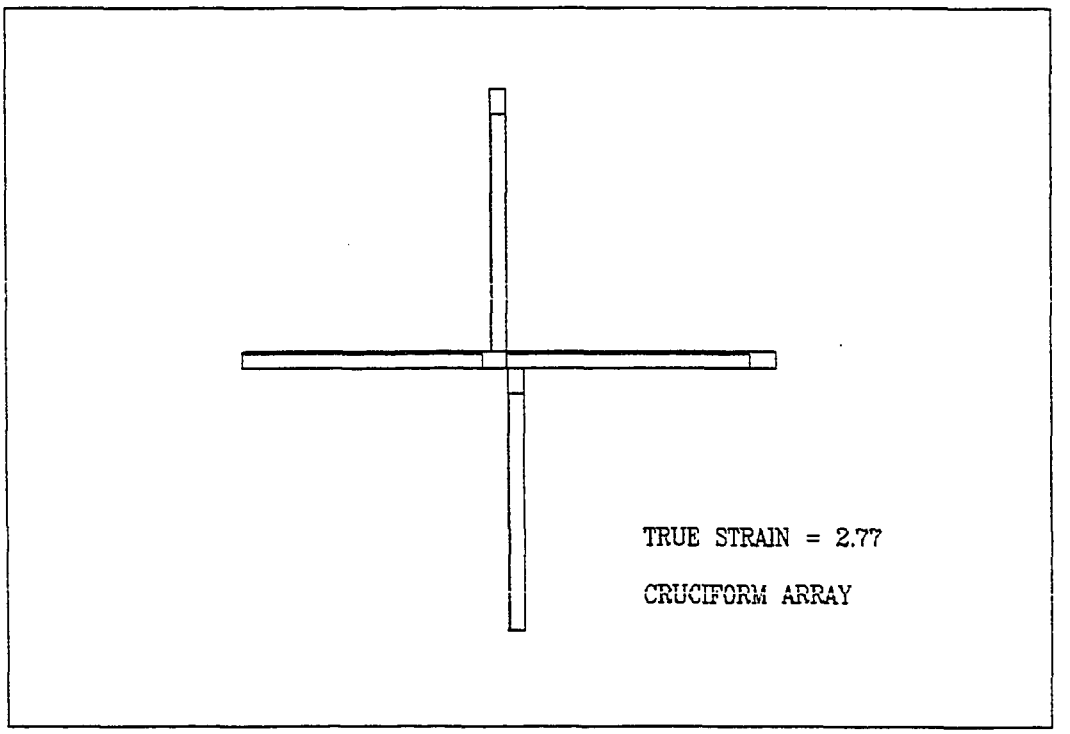

Figure 54. Pinwheel array of Ti-20Y polygons deformed to $\eta = 2.77$

The preceding discussion attempted to qualitatively characterize the difficulty in accomodating deformation in a composite where both phases deform only by plane strain. This suggests that it may be difficult to axisymmetrically deformation process any composite to very high η values in the absence of at least one "accommodating" phase like the fcc Cu in Cu-X that has a sufficient number of active slip systems to avoid these plane strain geometric fitting limitations. Thus, most of the possible deformation processed composites consisting of immiscible hcp/hcp, hcp/bcc, or bcc/bcc combinations may be rather stringently limited in their maximum attainable η values. Since most metallic elements are not fcc, such a conclusion suggests a major limitation to the prospective engineering applications of deformation processing to commercially useful alloy systems.

There are, however, still means available to produce deformation processed composites without fcc phases, including the following:

1. By starting the deformation processing with a specimen possessing exceptionally fine dendrites (by casting with melt spinning or similar techniques) or powder particle sizes (by mechanical alloying, CIP, and/or HIP processing), one might achieve a filamentary microstructure in the range of tens of nanometers after deformation processing to relatively modest true strains.

2. By deformation processing hcp or bcc matrix composites at carefully selected elevated temperatures, one might be able to avoid recrystallization and cylinderization/spheroidization while benefitting from the additional slip systems (to permit axisymmetric strain rather than plane strain) which become active at elevated temperatures. This strategy may be particularly effective in bcc metals, where several slip systems are available with only modestly higher resolved shear stresses.

3. Deformation processing by rolling the composite into sheet rather than swaging or drawing the composite into rod/wire forms would presumably avoid the geometric constraint of fitting plane straining phases into a cylindrical specimen shape. In rolled sheet, both the Ti and Y phases would be free to assume the natural lamellar shape that results from plane strain.

The commercial ramifications of the third item above are potentially large. Plate and sheet products are more useful in most engineering applications than rod or wire. If Ti and Y in a Ti-20Y composite acquire the rolling texture typically seen in pure Ti, they would form lamellae with the crystallographic alignment depicted in Figure 55. In this arrangement, the $<10\bar{1}0>$ axis of the crystal aligns with the rolling direction and the <0001> direction is tilted at a 20° to 40° angle to the sheet normal [29]. Such a texture would position the lamellae with their $<11\bar{2}0>$ slip directions tilted 20° to 40° with respect to the lamellae boundaries. Thus a dislocation on the only available slip direction for either basal or prism slip could move only a relatively limited distance before encountering the next lamella in the sheet. This is in contrast to the situation in Cu-X sheet where the large number of available slip systems in the fcc matrix permit some dislocations to run very large distances before encountering a lamellar barrier.

Overall, this study suggests that the prospect for producing rod or wire product of Ti-20Y by room temperature deformation processing of conventionally cast material appear to be limited at best. However, the potential exists to develop useful Ti-20Y (and possibly other hcp/hcp, hcp/bcc, or bcc/bcc) composites in plate/sheet form where the plane strain limitation of the deforming phases could be an asset to achieving high strength in a composite with excellent interphase bonding.

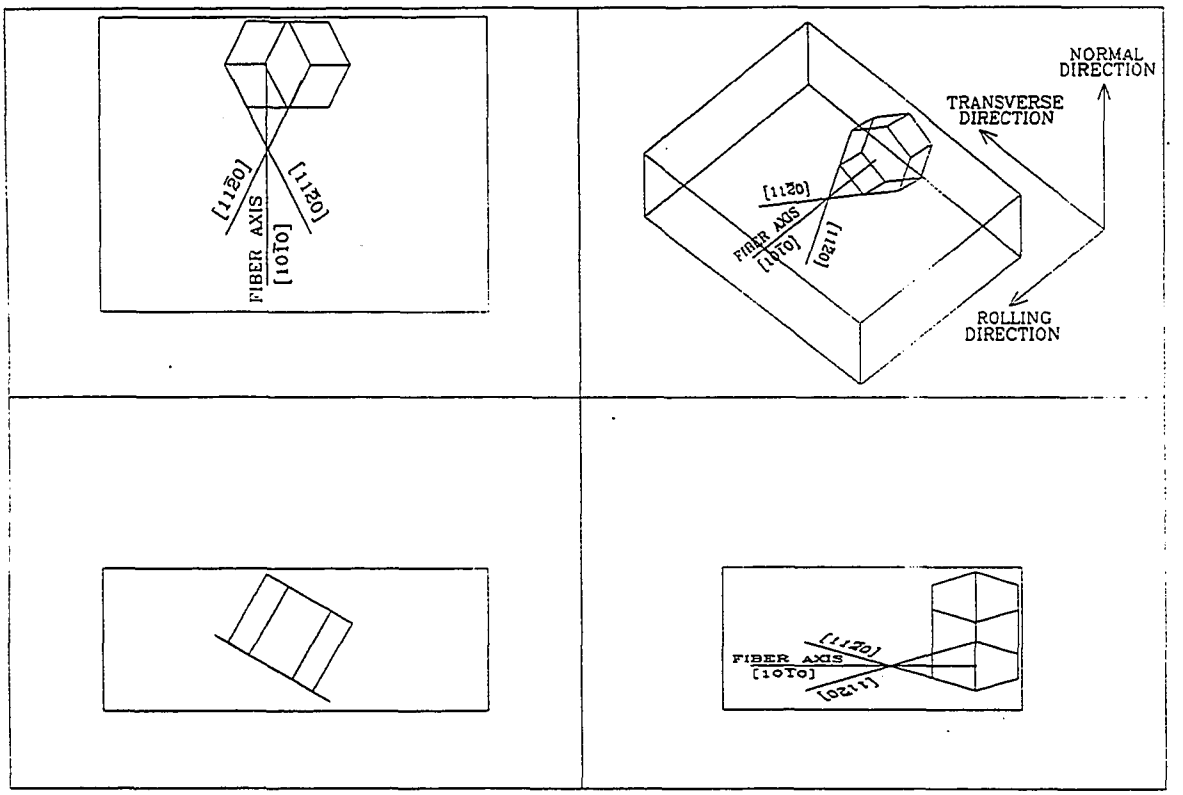

Figure 55. Top, front, right profile, and isometric views of the crystallographic texture of rolled Ti or Y lamella with the $<10\bar{1}0>$ direction parallel to the rolling direction and the <0001> direction tilted at 20° to 40° from the rolled sheet normal

SUMMARY AND CONCLUSIONS

1. Deformation processing can be used to produce a fine-scaled composite of Ti and 20 vol. % Y at deformation true strains as high as 12.8; however, the filamentary microstructure characteristic of the Cu-X composites was not produced at true strains higher than 7.27. A recrystallized, equi-axed grain structure was observed at higher η values.

2. For this Ti-20Y composite, deformation processing to true strains up to 7.27 showed a dependence of UTS on Ti phase spacing following a power function relationship:

$$\sigma_{c,uts} = 522\ (t_{Ti})^{-0.35}$$

where $\sigma_{c,uts}$ is the composite ultimate tensile strength expressed in MPa and t_{Ti} is the average Ti phase thickness expressed in μm. The slope of -0.35 in this relation is similar to the rate of strengthening with phase spacing reduction than is seen in the Cu-X composites for $\eta > 4$.

3. The deformation processing model of Embury and Fisher provides the best prediction of the Ti-20Y composite strengthening over the range $0 \leq \eta \leq 7.27$.

4. Both the Ti and Y phases in deformation processed Ti-20Y composite acquire a $<10\bar{1}0>$ fiber texture at deformation processing true strains between 2.25 and 5.03. The presence of the $<10\bar{1}0>$ fiber texture limits the strain of the Ti and Y filaments to plane strain, resulting in a convoluted ribbon phase shape for both Ti and Y. The Ti-20Y deformation processed composite is similar to the Cu-X deformation processed composites in that high-aspect ratio filaments form as the deformation progresses. The Ti-20Y composites differ from the Cu-X composites in that both phase types in Ti-20Y (Ti and Y) develop a crystallographic texture that limits their

strain to plane strain while in the Cu-X composites the bcc phase (X) is the only phase limited to plane strain.

5. For small filament thicknesses (less than about 100nm), a recovery anneal of 700° C. for 30 minutes appears to initiate spheroidization and recrystallization of both the Ti and the Y. This recrystallization process converts the high aspect ratio, convoluted ribbon phase shape to an approximately equiaxed grain structure and substantially weakens the specimen.

6. The deformation processing procedures followed in this experiment resulted in specimens with consistently good ductility as measured by tensile testing. All ductility values measured (except one specimen at $\eta = 12.8$ that had been severely cold worked prior to testing) lay within the range of 35% to 50% reduction in area at the fracture surface.

7. Development of a commercially useful deformation processed Ti-Y composite would require either hot work to impart the deformation processing or cold work, preferrably on a sample of very fine initial phase size, with an optimized recovery annealing time and temperature that must be high enough to permit further deformation without breakage but not so high as to permit spheroidization and loss of the textured, nanofilamentary microstructure necessary for high strength.

8. The observed texture of the Ti and Y phases suggest that rolling the Ti-20Y into sheet might produce a superior composite to that attainable by swaging or drawing the material into rod or wire.

REFERENCES

1. The Book of Exodus, Chapter 5, verses 6-7, *The Holy Bible: New International Version.* Zondervan Bible Publishers, Grand Rapids, Michigan (1984).

2. J.D. Embury and R.M. Fisher, *Acta Metall.*, **14**, 147-159 (1966).

3. G. Frommeyer and G. Wassermann, *Acta Metall.*, **23**, 1353-1360 (1975).

4. P.D. Funkenbusch and T.H. Courtney, *Acta Metall.*, **33**, 913 (1985).

5. H.P. Wahl and G. Wassermann, *Z. Metall.*, **61**, 326-339 (1970).

6. J. Bevk, J.P. Harbison, and J.L. Bell, *Journal of Applied Physics* **49**(12) (1978) 6031-6038.

7. J.D. Verhoeven, F.A. Schmidt, E.D. Gibson, and W.A. Spitzig, *Journal of Metals* **38**(9) (1986) 20-24.

8. J.D. Verhoeven, W.A. Spitzig, L.L. Jones, H.L. Downing, C.L. Trybus, E.D. Gibson, L.S. Chumbley, L.G. Fritzmeier, and G.D. Schnittgrund, *Journal of Materials Engineering* **12**(2) (1990) 127-139

9. W.A. Spitzig and P.D. Krotz, *Acta Metallurgica* **36**(7) (1988) 1709-1715.

10. J.D. Verhoeven, W.A. Spitzig, F.A. Schmidt, and C.L. Trybus, *Materials & Manufacturing Processes* **4**(2) (1989) 197-209.

11. J.D. Verhoeven, W.A. Spitzig, F.A. Schmidt, P.D. Krotz, and E.D. Gibson, *Journal of Materials Science* **24** (1989) 1015-1020.

12. P.D. Funkenbusch and T.H. Courtney, *Acta Metallurgica*, **33** (5) (1985) 913-922.

13. L.S. Chumbley, H.L. Downing, W.A. Spitzig, and J.D. Verhoeven, *Materials Science & Engineering,* **A117** (1989) 59-65.

14. C.L. Trybus, L.S. Chumbley, W.A. Spitzig, and J.D. Verhoeven, *Ultramicroscopy* **30** (1989) 315-320.

15. P.D. Funkenbusch and T.H. Courtney, *Scripta Metallurgica* , **23** (1989) 1719-1724.

16. W.A. Spitzig, J.D. Verhoeven, C.L. Trybus, L.S. Chumbley, & P.D. Funkenbusch, and T.H. Courtney, (a series of four communications) *Scripta Metallurgica et Materialia* **24** (1990) 1171-1184.

17. C.A. Trybus, Ph.D. Dissertation, Iowa State University, (1988).

18. D.R. Askeland, *The Science and Engineering of Materials*,, 3rd ed.; PWS Publishing, Boston, (1994).

19. M.A. Morris and D.G. Morris, *Materials Science and Engineering* **A111**, (1989) 115-127.

20. E. Orowan, *Symposium on Internal Stresses in Metals and Alloys, Discussion, Monograph and Report Series No. 5*, Inst. of Metals, London (1948) 451.

21. J.D. Verhoeven, L.S. Chumbley, F.C. Laabs, and W.A. Spitzig, *Acta Metall.* **39**, (1991) 2825.

22. J.G. Sevillano, *Strength of Metals and Alloys, Proc ICSMA 5* ed. P. Haasen, V. Gerold, G. Kowtorz, Pergamon Press, Oxford (1980) 819-824.

23. C. Biselli and D.G. Morris, *Acta Metall. Mater.* **42**, No. 1 (1994) 163-176.

24. P.D. Funkenbusch, J.K. Lee, and T.H. Courtney, *Metallurgical Transactions A* **18A**, (1987) 1249-1256.

25. J.D. Verhoeven, H.L. Downing, L.S. Chumbley, and E.D. Gibson, *J. Appl. Phys.*,**65** (3) (1989) 1293-1300.

26. A.R. Pelton, F.C. Laabs, W.A. Spitzig, and C.C. Cheng, *Ultramicroscopy*, **22**,(1987) 251-266.

27. J.S. Koehler, *Phys. Rev. B*, **2**, (1970) 547.

28. Morris and Morris, *Acta Metall. Mater.*, **39**, No. 8 (1991) 1763-1770.

29. G.Y. Chin, *ASM Metals Handbook*, **8**, (1985) 229-232.

30. A.T. English and G.Y. Chin, *Acta Metall.* **13**, (1965) 1013.

31. A.G. Silimperi and A.M. Russell, unpublished research (1993).

32. W.F. Hosford, Jr., *Trans. Met. Soc. AIME* **230**, (1964) 12-15.

33. D.W. Bare and O.N. Carlson, *Proceedings of the Forty-Second Annual Convention of the American Society for Metals*, Philadelphia, PA, October 17-21,1960.

34. B.G. Koepke, E.D. Gibson, and T.E. Scott, *Transactions Quarterly* **60**, No. 3 (1967) 409-417.

35. O.N. Carlson, D.W. Bare, E.D. Gibson, and F.A. Schmidt, *Symposium on Newer Metals: Special Technical Publication No. 272*, American Society for Testing Materials, 1959, 144-159.

36. M.J. Donachie, Jr., *Titanium: A Technical Guide*, ASM International, 1988, 40-41.

37. B.W. Christ, *ASM Metals Handbook*, **8**, (1985) 28-32.

38. E.E. Underwood, *Quantitative Stereology*, Addison-Wesley, 1970, Chap 3-4.

39. C.H.P. Lupis, *Chemical Thermodynamics of Materials*, Elsevier Science Publishing Co., New York (1983) 514.

40. E.A. Anderson, D.C. Jillson, and S.R. Dunbar, *Journal of Metals Trans AIME* **197** (1953) 1191-1197.

41. R.E. Reed-Hill and R. Abbaschian, *Physical Metallurgy Principles*, 3rd ed., PWS-Kent Publishing Co., Boston (1992) 142-144.

42. J.C. Malzahn, T.H. Courtney, and Y. Leng, *Acta Metall.* **37**, No. 7 (1989) 1735-1745.

43. T.H. Courtney and J.C. Malzahn Kampe, *Acta Metall.* **37**, No. 7 (1989) 1747-1758.

44. A.M. Russell, T.W. Ellis, and L.S. Chumbley, *Journal of Materials Science* (in press).

45. S. Willson, private communication.

ACKNOWLEDGMENTS

This work was performed at the Ames Laboratory of the U.S. Department of Energy under contract No. W-7405-Eng-82. Additional support was also provided by the Engineering Research Institute of the College of Engineering, Iowa State University, and by Rohr, Inc., Chula Vista, CA and G & S Titanium Co., Wooster, OH.

The author is grateful to the Program of Study Committee who helped plan and direct this project: Profs. Scott Chumbley (chair), Pat Kavanagh, Palaniappa Molian, Rohit Trivedi, and John Verhoeven and to Profs. David Boylan and Monroe Wechsler who planted seeds that lay dormant for several years before sprouting. The shared wisdom of Dr. Chumbley on topics ranging from metallurgy to the trajectories of plummeting sheep has been especially helpful and inspirational. The author is also grateful to Dr. Timothy Ellis for his original ideations on the topic of hcp metal-metal matrix composites and for his frequent consultations and words of encouragement. The assistance of Dr. Brian Norris and Messrs. Charlie Burg, Tom Donizetti, Brian Espeland, Jerry Hand, Larry Jones, Steve Lee, Lanny Lincoln, Brian Norris, Lester Reed, Hal Sailsbury, Rick Schmidt, Anthony Silimperi, Jon Weis, and John Wheelock is gratefully recognized in funding, producing, and deformation processing the materials studied.

The author also wishes to thank his fellow research group members at the Ames Laboratory for their support and guidance in the operation of sometimes refractory pieces of apparatus, particularly Mr. Fran Laabs for his patient mentoring on the use of the SEM, TEM, and the x-ray texture apparatus and for his masterful TEM sample preparation, photography, and general insights into matters ranging from the atomic scale to the global scale. The tutelage of Mr. Jeff Jensen on the mysteries of the Macintosh IIci, thermodynamics, and related subjects is also gratefully acknowledged, as is the technical and moral support and general good humor of Messrs Mohd Haji-Mahmood and Todd Voiles,

Madame Karen Pauwels, and Mademoiselle Lavonne Carson. Special assistance from Dr. Matt Kramer and Messrs. Kevin Dennis and Ed Hendrickson has also been of value.

In addition, the accomodations in workloads and the attitude of encouragement from Profs. Mike Berard, Roland Jenison, and David Kao were immensely helpful in completing this task in a finite time span. The author is also grateful to Prof. Gene Kellenberger for showing by his example that the "middle-aged Ph.D." is not impossible and to Prof. Martha Selby who graciously accomodated frequent last-minute instructor preparation emergencies in Marston Hall caused by the author's over-long attention to activities in Wilhelm Hall. The author especially appreciates the impeccable professional competence and good humor provided by Mesdames Patti Boone, Penni Bryant and Susan Lund throughout this project.

Finally, the author is grateful for the patient support of Messrs. Raymond Russell, Jeff Russell, and Mark Russell; Mesdames Helen Russell and Laurel Russell; and Mademoiselle Kristen Russell for their willingness to overlook late arrivals to scheduled events, failure to read bed-time stories, absences at school events, and intermittent grumpiness by the sometimes harried author throughout this 22-year journey.